THE IMPLEMENTATION OF OPTOFLUIDIC MICROSCOPY ON A CHIP SCALE AND ITS POTENTIAL APPLICATIONS IN BIOLOGY STUDIES

Thesis by

Lap Man Lee

In Partial Fulfillment of the Requirements for the

Degree of

Doctor of Philosophy

CALIFORNIA INSTITUTE OF TECHNOLOGY

Pasadena, California

2012

(Defended September 12th, 2011)

ii

Acknowledgement

The completion of my thesis is based on support and help from many individuals. First, I would like to express my gratitude to my PhD advisor Prof. Changhuei Yang for offering me a chance to work on an emerging research field of optofluidics and participate in the development of optofluidic microscopy (OFM), which leads to many successful results. His guidance has led the OFM project from an elegant engineering idea to reality. His enthusiasm and creativity in conducting academic research is forever young, motivating us to pursue excellence in our projects. I thank him for introducing me to biophotonics and allowing me to play a role in contributing to the field.

I want to thank Prof. Yu-Chong Tai for being my thesis committee chair. His pioneering work in MEMS has always been my motivation to pursue something 'big' in the world of 'small'. You will find yourself learning something new every time you interact with him, not only in science but also in life. I want to thank Prof. Chin-Lin Guo for the discussion after the committee meeting. I find his advice very useful. I am thankful for suggestions from Prof. Azita Emami, which made my PhD work more complete. I also acknowledge my candidacy committee members, Prof. Yu-Chong Tai, Prof. Mory Gharib and Prof. Chin-Lin Guo for passing me.

Dr. Xin Heng, Dr. Xiquan Cui, Sean Pang, Seung Ah Lee, and Chao Han are my teammates in OFM. We work closely together and exchange research experience, and this greatly accelerates the progress of our OFM projects. Dr. Jigang Wu was my mentor and labmate in the last two years of my PhD study. He is always determined to solve complicated research problems in a direct, prompt, and smart way. I also want to thank Dr. Meng Cui, Jian Ren, Guoan Zheng, Zheng Li, Dr. Zahid Yaqoob, and Dr. Benjamin Judkewitz for teaching me optics. I joined the group with practically zero knowledge in optics. Fortunately, they are never selfish and always patient, even when I ask very simple optics questions. I am so grateful to have Dr. Emily McDowell and Ying Min Wang as my bioengineering

buddies in the group. They give me a lot of support when I run into problems. Anne Sullivan, Agnes Tong, Christine Garske, and Ya-Yun Liu and are our group manager and secretaries. They are very helpful to supply and run the lab safely and smoothly.

I need to thank Ali Ghaffari, the lab manager of Watson Microfludic Foundary, and Bophan Chim, Guy DeRose, and Melissa Melendes from the Kavli NanoScience Institute at Caltech. They have helped me to solve many technical problems in fabrication. I am grateful to Justin Kim in Tai's group, who helped me to coat parylene for devices. I appreciate the help and care from Linda Scott, the secretary of the bioengineering option and Icy Ma from the grad student office. I also want to thank Dr. Felicia Hunt, the Associate Dean of Graduate Studies for the discussions.

Here I have to give credit to my masters and undergraduate advisors, Prof. Yitshak Zohar at the University of Arizona and Prof. Yi-Kuen Lee at Hong Kong University of Science and Technology, who brought me to the fascinating research field of microfluidics and BioMEMS, taught me fluid mechanics and helped me to define the right way to conduct experimental work. I am indebted to Prof. Sandra Troian, who allowed me to audit her beautiful fluid mechanics class at Caltech.

I am lucky to have a mom and dad who give me complete freedom, not pressure, to decide what I like and want to do in my life. I cherish the love and care from my girlfriend, May Lam. I owe them so much so much. I appreciate the friendship from the Hong Kong student community at Caltech, for their support and suggestions throughout my entire journey as a PhD student. I feel grateful to my bioengineering classmates in my year, Eugene Buchko, Fiona Chandra, Josh Michener, and Hesham Azizgolshani. Thanks for their help and encouragement in the long preparation of my qualifying exam. I want to thank Chi-kwan Chan from Arizona, Lilian Wong and Heywood Tam from Caltech. They have been my fountain of wisdom on many problems. It happens they are all physics or pure math PhDs.

Finally, I would like to acknowledge funding from the Croucher Foundation in Hong Kong, which arrived just at the right time and allowed me to continue my PhD study at Caltech.

Abstract

This thesis presents an effort to miniaturize conventional optical microscopy to a chip level using microfluidic technology. Modern compound microscopes use a set of bulk glass lenses to form magnified images from biological objects. This limits the possibility of shrinking the size of a microscope system. The invention of micro/nanofabrication technology gives hope to engineers who want to rethink the way we build optical microscopes. This advancement can fundamentally reform the way clinicians and biologists conduct microscopy. Optofluidic microscopy (OFM) is a miniaturized optical imaging method which utilizes a microfluidic flow to deliver biological samples across a 1-D or 2-D array of sampling points defined in a microfluidic channel for optical scanning. The optical information of these sampling points is collected by a CMOS imaging sensor on the bottom of the microfluidic channel. Although the size of the OFM device is as small as a US dime, it can render high resolution images of less than 1 μm with quality comparable to that of a bulky, standard optical microscope. OFM has a good potential in various biological applications. For example, the integration of an OFM system with high-speed hydrodynamic focusing technology will allow very large scale imaging-based analysis of cells or microorganisms; the compactness and low cost nature of OFM systems can enable portable or even disposable biomedical diagnostic tools for future telemedicine and personalized health care.

Table of Contents

List of Figures

List of Tables

Nomenclature

Au: Gold

CCD: Charge coupled device

CMOS: Complementary metal–oxide–semiconductor

DIC: Differential interference contrast

FIB: Focused ion beam

FWHM: Full width at half maximum

FZP: Fresnel zone plate

IC: Integrated circuit

NA: Numerical aperture

NSOM: Near-field scanning optical microscope/microscopy

OFM: Optofluidic microscope/microscopy

PDMS: Polydimethylsiloxane

PEG: Polyethylene glycol

PMMA: Poly(methyl methacrylate)

PSF: Point spread function

SEM: Scanning electron microscope

SNR: Signal-to-noise ratio

TEM: Transmission electron microscope

Chapter 1: Introduction

Optical microscopy was first invented in the 17th century. The father of microscopy, Anton van Leeuwenhoek of the Netherlands, invented new methods for manufacturing large curvature magnifying lenses to improve the optical performance of optical microscopes. He was the first to observe bacteria and yeast plants in a drop of water and the circulation of blood corpuscles in capillaries. Robert Hooke, following Leeuwenhoek's work, popularized microscopy by seeing fleas, mites and the compound eyes of flies under a light microscope [1, 2]. From that moment, the optical microscope became an essential tool in any analytical laboratory and lead to many groundbreaking discoveries in different levels in biology. Through several centuries, optical scientists and engineers continuously improved the design and enabled new functionalities in light microscopy, but the fundamental working principle remains the same: using a glass optical lens to create magnified images from biological objects. Recent advancement in scanning optical microscopy and microfluidics technology gives hope to engineers who want to re-think the way we conduct light microscopy. The first chapter of this thesis reviews and summarizes a new method to miniaturize and simplify optical microscopy through optofluidic integration technology. We named this novel miniaturized optical imaging approach optofluidic microscopy (OFM).

1.1 Optical Microscopy

The resolution of the naked human eye is about 0.1 mm which is about the width of a hair. Most biological entities are much smaller than that scale. For example, a human red blood cell has a standard size of about 6-8 μm. Therefore, humans make tools to magnify microscopic objects so that they can be discerned by our eyes. Light microscopes can be defined as any optical instrument that produces magnified images from an object in the visible light spectrum, from 400 nm to 700 nm. After the birth of the first optical microscope in the late 17th century, microscopes with a wide variety of functionalities emerged and have been commercialized, dark field, confocal, phase contrast, differential interference contrast (DIC), and fluorescence, to name a few. Different versions of microscopy use various approaches and strategies to enhance the contrast, signal-to-noise (SNR) ratio, and quality of the images. Nowadays, modern microscopes are very sophisticated and equipped with numerous optical elements, such as dichrotic filters, wave plates, beam splitters, pinholes, and polarizers. These are being arranged with precise optical alignment, as shown in Figure 1.1. No matter how complicated an optical microscope can be, the image resolution is diffraction limited and primarily determined by the objective lens.
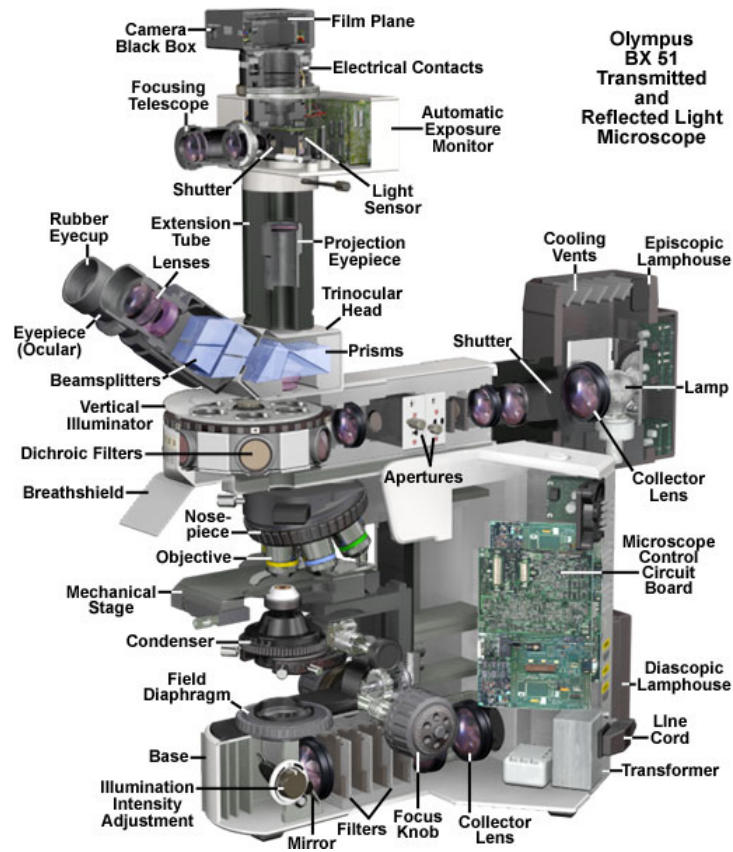
Figure 1.1 A schematic of a modern optical microscope

(Courtesy: http://micro.magnet.fsu.edu/primer/anatomy/bx51cutaway.html)

1.1.1 Resolution of Imaging Systems

Every engineering system has its limit and optical imaging systems are no exception. The important parameter that characterizes the performance of an imaging system is its resolution, which describes the ability of an imaging system to resolve details of an extended target object. Suppose we have an infinitesimal illuminating object; light emitted from this point source no longer exists as a point after passing an optical lens. Instead, it will spread with certain intensity distribution profile in the image plane. This is known as the point spread function (PSF) of the optical system. Using scalar diffraction theory [3], the far-field intensity distribution of a plane wave impinging on a circular aperture can be formulated by Fraunhofer diffraction. When a lens is placed right behind the pinhole, a pattern of concentric rings known as the Airy disk, which is formulated as a Bessel function of the first kind, is formed at the focal length of the lens. The distance, defined as R, from the highest intensity point located in the middle of the center spot to the first zero of the Bessel function in intensity profile is given by:

$$R = 1.22 \frac{f\lambda}{D} \qquad (1\text{-}1)$$

where f is the focal length of the lens, λ is the light wavelength, and D is the diameter of the aperture lens. The numerical aperture of lens is defined as

$$NA = \mu \sin\theta \qquad (1\text{-}2)$$

where μ is the refraction index of the medium and θ is the half-angle of the cone of light collected by the lens. Suppose there are two point sources in close proximity on the object plane: each point source will project an Airy pattern in the image plane. When we move these two point sources closer, these two Airy profiles start overlap each other until we cannot distinguish any separation between them. There are several different criteria to characterize optical resolution. The most

common way is the Rayleigh criterion (Figure 1.1.1(a)), which is defined as the place at which the peak of the Airy disk from one point source overlaps with the first zero of the other (Figure 1.1.1(b)). Following Equation (1-1), the resolution based on Rayleigh criterion, $R_{Rayleigh}$, is defined as:

$$R_{Rayleigh} = 0.61 \frac{\lambda}{NA} \quad . \tag{1-3}$$

In Rayleigh criterion, we are still able to discern the separation of two point sources quite well since there is a central minimum between the peaks of each Airy disk profile. A further decrease in the distance between the two point sources will cause the central dip to diminish and eventually disappear. This leads to the definition of a more stringent criterion, the Sparrow criterion, $R_{Sparrow}$, as shown in Figure 1.1.1(c),(d), where both the first and second derivatives of the combined intensity of Airy disks from two point sources are zero:

$$R_{Sparrow} = 0.47 \frac{\lambda}{NA} \quad . \tag{1-4}$$

In the other approach, the FWHM of the Airy disk is used as the resolution criterion, R_{FWHM}, which is defined as:

$$R_{FWHM} = 0.52 \frac{\lambda}{NA} \quad . \tag{1-5}$$

Notice that Equation (1-5) is based on the Airy disk profile, while Gaussian distribution is used to fit the intensity profile to determine the FWHM. We should pay attention to the confusion here.

One point we should notice is that the NA should always be smaller than 1.0 if the refractive index of the medium is air. In this case, the best optical resolution under visible light illumination (532 nm) would be around 300 nm. If we allow the use of water- or oil-immersion lenses, or employ a shorter wavelength illumination source, we can push this resolution limit

closed to 200 nm, although such high resolution, in practice, is not usually obtained. This range is about the resolution limit of diffraction-limited optical systems.
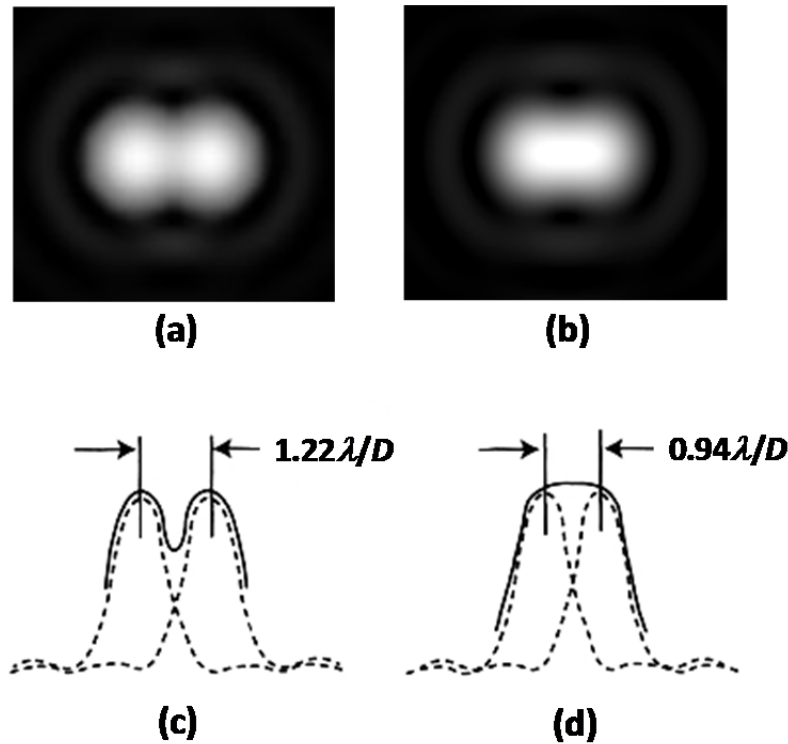
Figure 1.1.1 An illustration of optical resolution defined by (a) Rayleigh's criteria, (b) Sparrow's criteria

In the past decades, optical scientists and engineers have made tremendous efforts to break the diffraction limit of traditional optical microscopes. These techniques are known as super-resolution microscopy. One approach is by using near-field optical scanning technique, to create a near-field scanning optical microscope (NSOM). An illumination beam, which is diffraction limited is coupled into a probe tip with a nano-aperture, which is smaller than one

wavelength (for example, about 50 nm). During the scanning process, the probe is brought in a close proximity to the sample surface. The nano-aperture probe creates a tightly localized light field in the form of evanescent wave, interacting with scatters on sample surface. These near-field components are modified and converted into propagating far-field components so that they can be collected by collective optics and detected by a photodetector. The scanning feature of NSOM allows us to illuminate and detect one resolution area of the sample at a time. Therefore, the nano-aperture probe of a NSOM is able to differentiate miniscule structures that are extremely close to each other with optical resolution of less than 100 nm [4, 5].

The other approach for super-resolution microscopy is by using far-field techniques. One example is photoactivation localization microscopy (PALM) [6, 7], or stochastic optical reconstruction microscopy (STORM) [8]. In this imaging scheme, individual molecules tagged with fluorescent markers are activated and bleached selectively at different time durations. Although this imaging method still uses diffraction-limited optical microscopes to render images at different time steps, individual molecules can be discerned using Gaussian fitting to estimate their positions precisely. While these super-resolution microscopy techniques remain an active research topic for many optical scientists and biophysicists, to my knowledge, the implementation of super-resolution microscopy in miniaturized optical imaging systems remains largely unexplored. It definitely deserves better thinking and more attention from microfluidic engineers to adapt these techniques on a chip-scale level in order to enhance performance, achieve better optical resolution, and simplify the infrastructure of the system.

1.1.2 Miniaturization of Optical Microscopy

The function of an optical microscope is to magnify and project a microscopic object to the image plane as illustrated in a simplified ray diagram in Figure 1.1.2.1. The magnification is determined by the ratio between the image height, h_2, and object height, h_1, or the ratio between image distance, l_2 and object distance, l_1:

$$M = \frac{h_2}{h_1} = \frac{l_2}{l_1}$$

(1-6)
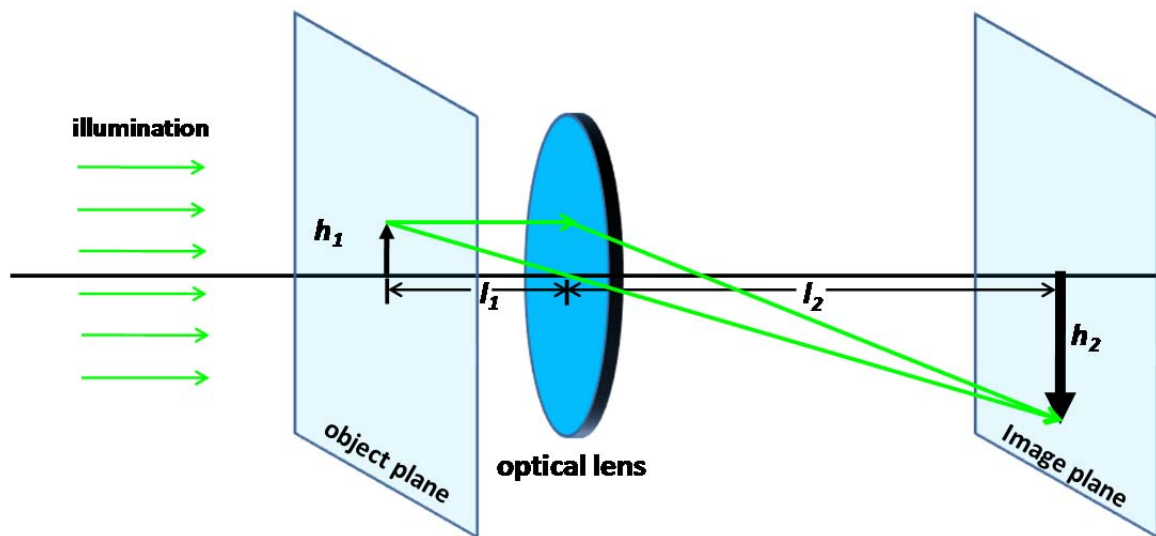
Figure 1.1.2.1 An illustration of a simplified ray diagram in conventional optical microscopy

The focal length of the optical lens is given by:

$$\frac{1}{f} = \frac{1}{l_1} + \frac{1}{l_2} \qquad .$$

(1-7)

Suppose a microscopic object is placed with an object distance of 10 μm in front of an optical lens; to magnify it 250 times, the image distance should be about 2.5 mm. To achieve such

magnification, the focal length is calculated to be about 10 μm (Equation (1-7)). To make such an optical lens from the simplified Lensmarker's equation (1-8), the radius of curvature, R_1, of the magnifying plano-convex lens ($R_2 \rightarrow \infty$) should be made on the order of 10 μm, given the lens material to be glass ($\mu = 1.5$):

$$\frac{1}{f} \approx (\mu - 1)\left(\frac{1}{R_1} - \frac{1}{R_2}\right) \qquad . \qquad (1\text{-}8)$$

One may argue that the miniaturization of optical microscopes is a trivial task. From the above formulation, the miniaturized microscope can be easily made with about size of a US dime. However, real life is not that straightforward. The above formulation is based on a thin lens assumption, which ignores a lot of aberration issues in image formation. Modern objective lenses, shown in Figure 1.1.2.2, are usually designed with computer-aided-design (CAD) software, like ZEMEX, to combine multiple lenses in order to correct optical aberrations and dispersion such as coma, astigmatism, geometrical distortion, field curvature, spherical and chromatic aberration. This is the reason why optical microscopes are very complicated, expensive, and bulky. We cannot rely on conventional optical principle to simply scale down the size of a microscope.

Figure 1.1.2.2 A schematic of a microscope objective

(Courtesy: http://www.olympusmicro.com/primer/anatomy/objectives.html)

Miniaturizing conventional optical microscopes with microfluidic technology has the following advantages:

1. High throughput — OFM systems can potentially achieve a very high throughput rate when integrated with advance hydrodynamic focusing units. OFM technology can lead to very large scale imaging-based cell analysis.

2. Operation in resource-poor environments — The OFM device has a very small size and can be made very compact and portable. It can be integrated into a cell phone or easily be carried from one place to another in resource-poor environments (for example, in developing countries or in space).

3. Low energy consumption — OFM devices consume less power than conventional optical microscopy due their smaller size.

4. Low production cost — miniaturized microscopes can be batch manufactured using standard photolithography technique, which greatly reduces production cost. The cost of a compact OFM device is about 10 USD.

Several research groups have designed and implemented different prototypes of miniaturized microscopes in the past decade [9-16]. These miniaturized microscopes are based on different working principles but with one common goal, which is to use light to reveal as much detailed information in biological specimens as possible while using a tool as simple as possible.

1.2 Full-Field Versus Scanning Optical Microscopy

Generally, there are two distinctive schemes in image formation of optical microscopy, namely full-field and scanning. In the full-field approach, the entire biological sample is flooded with illumination light for the full depth and field of view, as illustrated in Figure 1.2(a). This approach has an advantage of parallel processing; information from all the resolving points from the sample are transferred to the image plane simultaneously. The image acquisition time is much shorter since it involves only one time step. However, since intense light is used to illuminate the entire field of view throughout the whole depth of the specimen, rather than just at the focal plane or the focal point, much of the scattered or absorbed light coming from regions above and below the focal plane will be collected by the objective lens, contributing to out-of-focus blur in the final image and seriously degrading the image contrast and sharpness [17]. In the other approach, light is focused at one resolution of the specimen at a time; the scattered or absorbed light at that particular point is collected by the microscope objective and recorded by a photosensor as shown in Figure 1.2(b). Then either the illumination light spot or the biological sample is moved to reveal the light intensity at the next point. This process is repeated until the information from the whole field of view is acquired. In scanning optical microscopy, the problem of extracting information at the illuminated point becomes simpler and allows higher aberration tolerance in the collective optics. In addition, since light is focused only at one particular point of interest in the biological sample at each time step, there is no out-of-plane blur. This method also causes less damage to the biological sample since intense light is focused at only one point during the image acquisition. However, the image acquisition time is much longer and may pose a problem if we want to image or monitor real-time biological events (for example, in cell dynamics experiments). The image quality also depends highly on the stability and precision in light spot actuation and

biological sample translation. In addition, the experimental setup can be more complicated and expensive when compared with the full-field approach.

Illumination light

cover glass slide

biological sample

collection light

movement

(a)

(b)
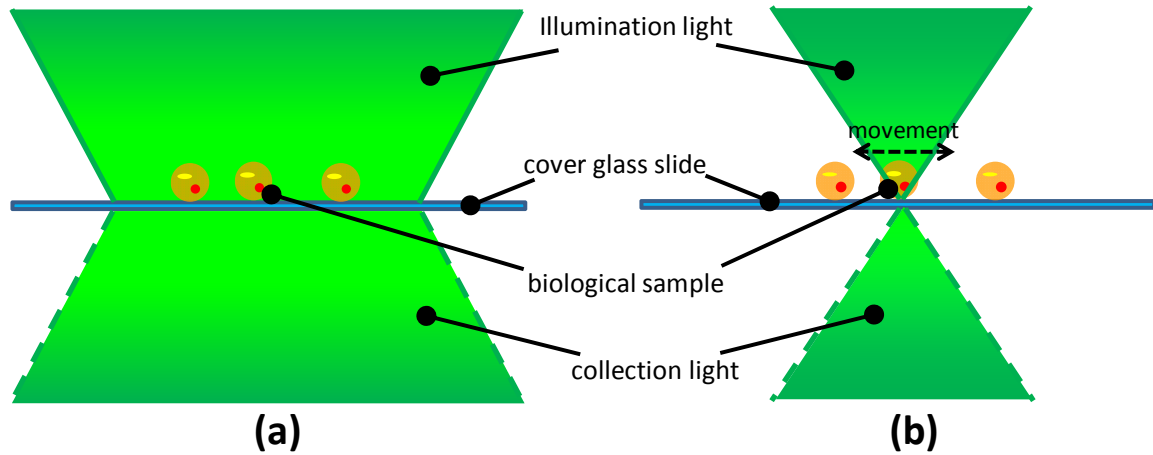
Figure 1.2 An illustration of two distinctive ways of illumination in optical microscopy: (a) full-field, (b) point scanning

1.2.1 Confocal Microscopy (by moving the light spot)

Modern confocal microscopes can be considered as a highly integrated system which combines an optical microscope, a photodetector (usually with a photomultiplier tube), a computing unit (for image data acquisition, processing, analysis and storage), and a laser system (for illumination) which can be with equipped with a wavelength selection device and a mechanical beam scanning device to actuate and direct the light spot to different positions of the sample. The basic concept of confocal microscopy was originally developed by Dr. Marvin Minsky in the 1950s. He produced a working microscope in 1955 and patented this invention in 1957 [18]. However, Minsky's idea has remained quiet for several decades, due to the lack of intense light sources and the lack of computational power to process the large amounts of data acquired from confocal microscopy. Several scientists have followed Minsky's idea to develop different mechanical scanning strategies to direct the point illumination from a laser to different parts of a biological specimen. With the advancement in computer technology and the development of more stable high-power lasers, confocal microscopy was finally commerialized in the 1990s. Laser scanning confocal microscopy (shown as in Figure 1.2.1.1), couples with fluorescent labeling techniques, lead to an explosion in numerous in-vitro and in-vivo applications in biomedical imaging. Now, confocal optical microscopy has become one of the most dominant imaging methods for daily laboratory analysis of biological molecules, cells, and living tissues.
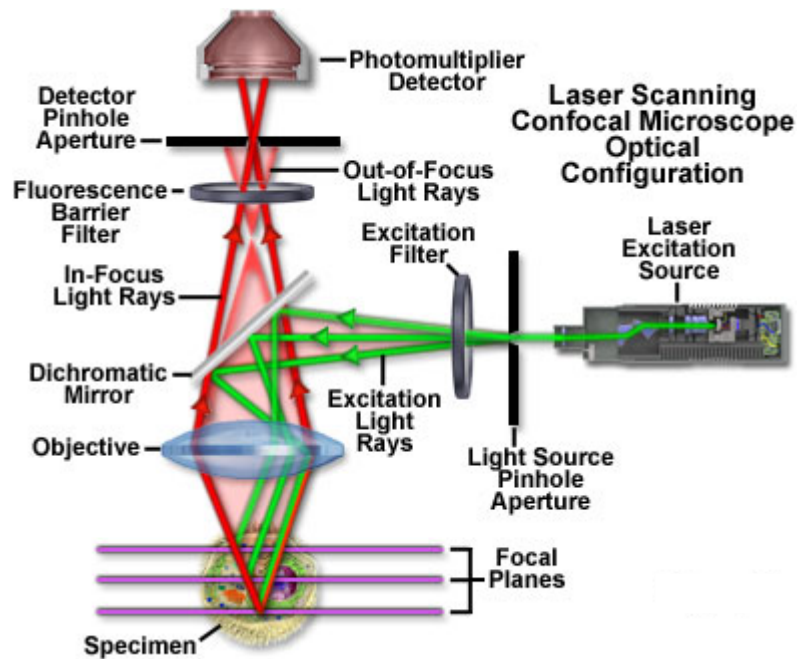
Figure 1.2.1.1 A schematic of laser scanning optical configuration in a modern confocal

microscope

(Courtesy: http://zeiss-campus.magnet.fsu.edu/articles/livecellimaging/techniques.html)

From an optical system point of view, confocal microscopy is fundamentally characterized by a pinhole aperture and point-by-point illumination on biological specimens. The incorporation of pinhole apertures in imaging is a distinctive feature of confocal microscopy. Usually the pinhole aperture is inserted in front of the photodetector of the confocal microscope system. The pinhole rejects any out-of-focus light from the biological sample; leads to a reduction in background illumination, an increase in signal-to-noise ratio (SNR), and an improvement in both the lateral and axial optical resolution. Thus, the pinhole aperture of confocal microscopy enables optical sectioning ability and allows 3-D image rendering for thick biological specimens which is difficult to achieve in other traditional full-field microscopy.
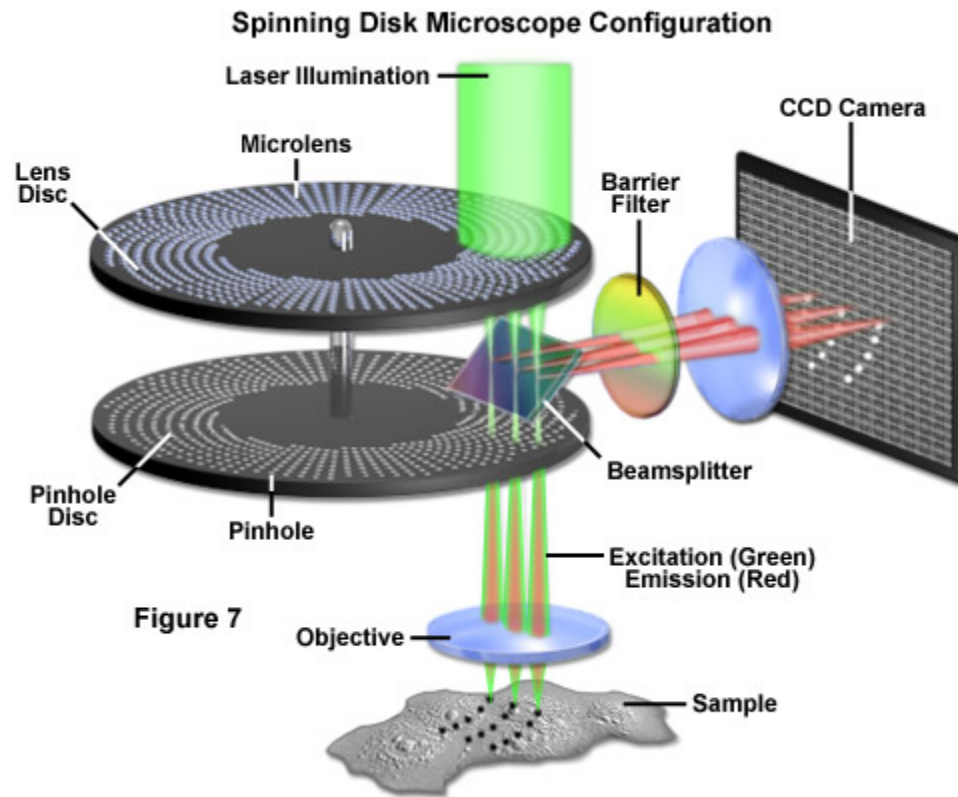
Figure 1.2.1.2 A schematic of Nipkow Disk optical configuration in modern confocal microscope

(Courtesy: http://zeiss-campus.magnet.fsu.edu/articles/livecellimaging/techniques.html)

In modern confocal microscopes, the light is tightly focused to a point by high-power objective lens and scanned across the entire field of interest on the biological sample. There are two different beam scanning techniques. The first one is single-beam scanning, which uses a pair of computer-controlled galvanometer mirrors or oscillating mirrors to scan the specimen in a raster pattern. In this case, usually a single-pixel imaging sensor device (for example, a photomultiplier tube) is used to measure the light intensity change during the scanning process. The other approach is by multiple-beam scanning. Some confocal microscopes are equipped with a spinning Nipkow disk which contains an array of pinholes aligned with microlenses for light focusing, as shown in Figure 1.2.1.2. Multiple-beam confocal microscopes are able to capture

microscopic images with an array detector, such as a charge-coupled device (CCD) or complementary metal oxide semiconductor (CMOS) camera, thus allowing quicker image acquisition. However, the scanning mechanism and date processing scheme used is more complicated.

Despite its relatively easy-to-understand working principle, confocal microscopy is considered the most important advancement in modern optical microscopy. However, the implementation of conventional confocal microscopy is in fact quite complicated. The complexity arises from the incorporation of a sophisticated control mechanism to precisely direct the tightly focused light to different parts of the biological specimen. In Chapter 5, I will present my recent progress in efforts to miniaturize and simplify confocal microscopy by using the OFM imaging approach.

1.2.2 Wide Field-of-View Microscopy (by moving the sample)

In traditional full-field microscopy, the field of view is usually inversely related to the resolution of microscope objective. That means it is not possible to render a large area microscopic image with good resolution (without serious aberration and image distortion). We can overcome this dilemma with optical scanning microscopy. Optical scanning microscopy can also be achieved by moving the biological specimen, rather than moving the focused light. In this imaging modality, an array of tightly focused spots is usually generated for illumination. Commercial scanning microscopes typically impose a 2-D raster scan on target samples under a high-resolution microscope objective using a 2-D motion controller. The full-view image can then be assembled from multiple, smaller-sized, high-resolution images. Recently our group developed a specially written hologram technique to generate a 2-D illumination grid of tightly focused light spots. The target sample is translated across the focal plane of the illumination grid using a 1-D motion controller; the intensity change of the illumination spots is recorded by a 2-D array of CMOS or CDD cameras underneath. The microscopic image can be reconstructed by a simple computer algorithm using the data of each line scan [19]. The 2-D illumination focus grid can be generated by Talbot effect. A metal mask with a 2-D aperture grid is illuminated with a collimated laser beam. The replicate of the aperture grid is reproduced at integer increments of the Talbot distance. The sample slide is then scanned at the one-and-a-half Talbot distance to render high-optical-resolution images [20]. This illumination-spot-array scanning imaging method abandons the use of expensive microscope objectives and highly simplifies the way we conduct wide field-of-view microscopy. Wide field-of-view microscopy has many practical applications in automated, high-resolution, and cost-effective biomedical imaging: such as high-throughput screening [21] and whole-slide digital pathology diagnosis [22].

1.3 Optofluidic Microscopy — a Brief Review

Optofluidic microscopy (OFM) can be defined as using miniaturized microscopes and microfluidics for sample scanning. Delivering biological samples through a microfluidic channel flow is the distinctive characteristic of OFM systems, differentiating them from other 'microscope-on-a-chip' systems.

Here I would like to provide a brief review on the development of OFM devices in our group. In 2006, the first proof-of-concept prototype OFM was developed [23]. A line of aperture array in a metal layer was fabricated on the floor of a PDMS microfluidic channel. The channel was tilted at a certain angle so that the biological sample, *C. elegans* could be translated on top of the aperture array under gravity. The light transmission through each aperture was relayed by a bulk microscope into an individual pixel of a CCD imaging sensor; the best optical resolution obtained was about 500 nm. In 2008, OFM was implemented completely 'on-chip'. The slanted line of apertures was fabricated directly on every alternate pixel of a CMOS imaging sensor using focused ion beam (FIB) machining [24]. With better microfluidic control on the biological samples using DC electrokinetics, spherical/ellipsoidal biological samples/entities, such as, pollen spores and *Chlamydomonas*, were imaged in high resolution at 800 nm. This greatly expanded the versatility of OFM on imaging samples with different shapes. About the same time, our group proceeded to another front in OFM development with the use of coherent light as the illumination source. A phase FZP fabricated on a glass plate replaced a conventional optical microscope as the relay to the OFM apertures [25]. (In this demonstration, the FZP was not integrated with the OFM device.)

Following that, a major effort was made to integrate an array of FZPs on top of a microfluidic channel in order to generate an array of tightly focused light spots with a resolution of 650 nm. This scheme led directly to the development of a fluorescence OFM system in which, when a fluorescent sample flowed through the channel and across the array of focused light spots, the fluorescence emissions were collected by a filter-coated CMOS sensor (which was coated on the floor of the microfluidic channel in order to render high resolution fluorescence images [26].

Another effort has been employed to incorporate collection optics in the floor of the microfluidic channel to enable the focusing capability in OFM systems using coherent illumination. An array of FZPs is defined on a spacing photoresist layer, in precise alignment with the apertures fabricated on the CMOS pixels underneath. Under a tilted plane wave illumination, the capability of dark field OFM imaging has been demonstrated. By combining both the illumination and collection FZP arrays fabricated on the top and bottom of the microfluidic channel, respectively, we next explore the potential to build a complete confocal OFM device.

1.4 Introduction to Microfluidics

Microfluidics is about the manipulation and detection of fluids (in liquid or gas phase or a combination of both, i.e. two-phase flow) or species suspended in fluid medium using structures on a micron scale such as channels, valves and pumps. Such operations can be conducted through mechanical, electrical, thermal, optical, magnetic, chemical, or even biological means. It is a highly interdisciplinary field intersecting engineering, physics, chemistry, and biology. Here I would like to restrict our scope of discussion to the domain of liquid flow (since most biological applications happen in liquid phase), in which we can assume that the fluid is incompressible. Fluid is composed of many finite-size molecules with finite distance between them under random motion and constant collisions. In some sense, fluids are not in continuum but composed of individual particles (when we scale down our observation sufficiently). However, if we allow our observation volume to be large enough to contain a sufficient number of fluid molecules to give an average value for the properties of the fluid (for example, the density or the velocity), these properties will be continuous in space and become independent of the number of molecules. Therefore, fluid can be treated as continuous and differentiable in space and time. This continuum assumption is very important and forms the base of the analysis of many fluid systems, since we can describe the entire domain of analysis by a set of partial differential equations instead of tracing the behavior of individual fluid molecules. In fluid mechanics, the behavior of fluid flow is primarily characterized by the Reynolds number, Re:

$$\mathrm{Re} = \frac{\rho U L}{\mu} \tag{1-9}$$

where ρ is the density, U and L denote the characteristic velocity and length, and μ is the dynamic viscosity. In microfluidics, characterized by small size and slow velocity, the Re number is usually small. In a low-Reynolds-number regime, convection becomes less important; although it

may not be fully negligible, fluid flow is dominated by viscous and surface forces. The flow field is predictable, stable, and even reversible. In pipe flows, if the Re number is lower than the transition (Re < 2300), the fluid flow remains laminar. One thing we should notice here is that laminar flow does not imply that we can completely neglect the inertial effect. In fact, the inertial effect can still play an important role in the fluid behavior or fluid and suspended particles interaction [27]. For example, for an average flow velocity of about 20 mm·s^{-1}, the inertial effect of the fluid can generate a significant amount of wall lift force and shear gradient force on the suspended particles, resulting in a continuous hydrodynamic focusing effect in the equilibrium position [28, 29]. In OFM applications, given the density and dynamic viscosity of water (1000 kg·m^{-3} and 1×10^{-3}N· s/m^2 respectively), the average velocity is usually less than 2 mm·s^{-1} and the channel width on the order of 100 μm. The Re number is then calculated as 0.1, which is lower than unity. Therefore, we can assume the flow to be within the Stokes flow limit, where the inertial effect is negligible.

While the fundamental science and physics remain a hot research topic for physicists, mechanical, and electrical engineers, the applications of microfluidics attract even more attention in the bioscience and biomedicine communities in both academic and clinical settings. From the start of the new millennium, the field of microfluidics has emerged and grown rapidly. Microfluidic devices can be built with hard materials such as, silicon, glass, and resin, or soft materials, like elastomer PDMS. Researchers began fabricating microfluidic devices on silicon and glass substrates back in the late 1980s when MEMS technology started to emerge and thrive [30]. Silicon micromachining techniques have been proven to be a versatile fabrication method based on standard photolithography techniques for microfluidic devices on the micron scale. The fabrication process has become more precise, reliable, and repeatable. Since silicon and glass have excellent mechanical and electrical properties, microfluidic devices made from MEMS

technology are very compatible for integration with electronic sensing, processing, and control components [31]. However, there are drawbacks and limitations in this approach. Since the fabrication process has to be conducted in cleanroom facilities, the production cost of silicon- or glass-based microfluidic devices is expensive and the device is thus not disposable, a quality which is desirable in certain biotechnological applications.

On another front, microfluidic researchers are looking for alternatives building devices. In the late 1990s, researchers at Harvard and Caltech started to incorporate the use of the soft material PDMS, a silicone-based elastomer, in the fabrication of microfluidic and optofluidic devices [32-36]. They called this technique soft-lithography. Note that soft-lithography can be generalized as a non-photolithographic strategy based on self-assembly and replica molding for carrying out micro- and nanofabrication, which includes microcontact printing (μCP), replica molding (REM), microtransfer molding (μTM), micromolding in capillaries (MIMIC), and solvent-assisted micromolding (SAMIM) [36]. Here I will only concentrate on replica molding, which is the most common approach to making single-layer PDMS microfluidics devices.
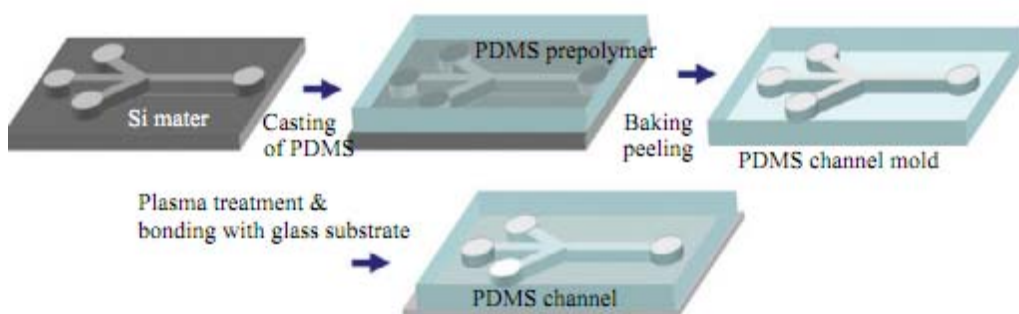
Figure 1.4 An illustration of soft-lithography fabrication for PDMS microfluidic devices

(courtesy: Soft Lithography for Microfluidics: a Review, BIOCHIP JOURNAL, Vol. 2, No. 1, 1-11, March 2008)

As illustrated in Figure 1.4, the soft-lithography process starts with a silicon wafer patterned with photoresist (for example, SU-8 or PMMA), which defines the feature of the microfluidic channel and is used as a master mold. The PDMS pre-polymer mixed with catalyst is poured onto the microfluidic master mold. Then, the PDMS is cured in a furnace at 80°C for 3 hours. The PDMS stack is peeled off from the master mold, forming a negative replica. After dicing and holes punching for the inlets and outlets, the PDMS replica is usually bonded with a piece of microscopic slide to form a microfluidic channel for off-chip applications. Surface cleaning by oxygen plasma or hydrochloric acid is sometimes employed to promote the bonding force.

The major advantage of using soft-lithography to fabricate microfluidic channel devices is the simplicity of its manufacturing process and a relatively low production cost. After the photolithography patterning of a silicon microfluidic mold, the PDMS casting can be conducted repeatedly without a cleanroom environment. The material property PDMS is also very suitable for many optofluidic applications [37]. The optical transparency and good optical quality of PDMS has been demonstrated in applications such as softlithographic fabrication of blazed gratings and solid immersion lenses [38, 39].

1.4.1 Optofluidic Integration

OFM devices gain their advantage by combining these two distinctive but complementary fabrication technologies. The optical sensing part of an OFM device consistes mainly of the CMOS imaging, which is manufactured from standard integrated circuit (IC) fabrication. It is robust and can be used for a long time. Cleanroom process, such as metal evaporation or FIB milling, can be conducted directly on top of the CMOS sensor. The microfluidic part, which is defined by soft-lithography, can be bonded temporarily or permanently onto the imaging sensor substrates, depending on application. A schematic of OFM systems is illustrated in Figure 1.4.1.
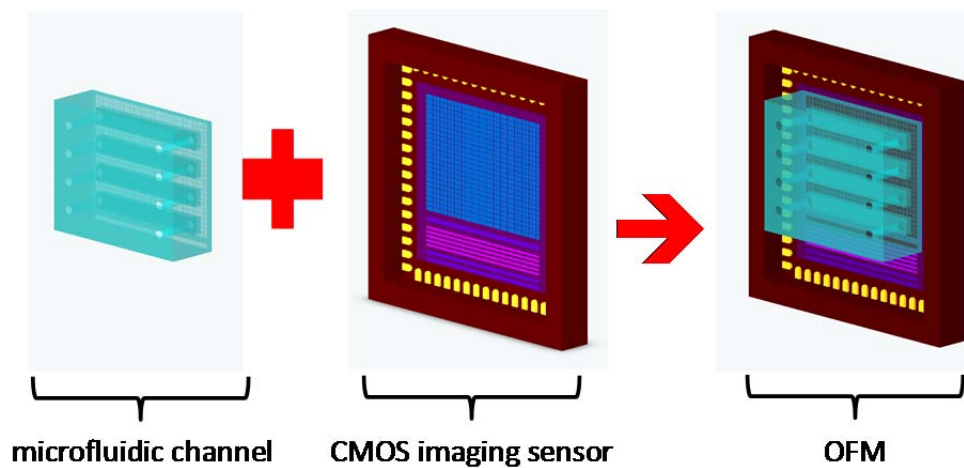
Figure 1.4.1 An illustration of integrated optofluidic imaging device

1.5 Structure of the Thesis

This thesis presents progress in the technological development of on-chip OFM systems. OFM delivers biological samples in a microfluidic flow integrated into a single CMOS imaging sensor in order to render high resolution images. In Chapter 2, I will explain the working principle, image resolution, and sampling characteristics of OFM. Microfluidic flow control of biological samples is crucial for good OFM imaging. Several flow strategies, such as pressure, electrokinetic and gravity-driven flows in PDMS microfluidic channels, are studied by experiment. Chapter 3 starts with the implementation of the first on-chip OFM system ever built in our group, which uses an array of collection apertures on a single metal layer fabricated immediately on top of the CMOS imaging sensor under incoherent light illumination. Following this route, an array of diffraction-based focusing elements, Fresnel zone plates (FZP), is built on top of the collection aperture array, separated by a spacing layer in precise alignment. This scheme enables the OFM device to collect light at a particular focal plane in the microfluidic channel with coherent plane wave illumination. In Chapter 4, an array of tightly focused spots is generated at the designed focal plane in the microfluidic channel through a specially recorded holographic plate or a set of FZP arrays integrated on top of the device under coherent illumination. This scheme has successfully led to the implementation of fluorescence OFM systems by coating an emission filter on top of the CMOS pixels. Chapter 5 presents the effort to combine integrated collection and illumination diffractive optical elements to achieve a complete confocal OFM system. Such an OFM system can enhance the image resolution and open up other opportunities in OFM imaging. I will also present several technology difficulties in this approach. Chapter 6 presents several potential applications of OFM systems in biomedicine and bioscience. Chapter 7 reviews and evaluates, incorporating other optofluidic integration techniques in OFM applications. One good example is incorporating the use of reconfigurable optofludic lenses in OFM systems.

References

[1] http://www.nature.com/news/2011/110304/full/news.2011.116.html

[2] http://inventors.about.com/od/mstartinventions/a/microscope.htm

[3] J. W. Goodman, Introduction to Fourier Optics, Roberts & Co, 3rd edition (2004)

[4] E. A. Ash and G. Nicholls, "Super-resolution aperture scanning microscope," *Nature* **237**, 510–512 (1972)

[5] U. Dürig, D. Pohl and F. Rohner, "Near field optical scanning microscopy," *Journal of Applied Physics* **59**, 3318–3327 (1986)

[6] E. Betzig, G. Patterson, R. Sougrat, O. Lindwasser, S. Olenych, J. Bonifacino, M. Davidson, J. Lippincott-Schwartz and H. Hess, "Imaging intracellular fluorescent proteins at nanometer resolution," *Science* **313**, 1642–1645 (2006)

[7] S. T. Hess, T. P. K. Girirajan and M. D. Mason, "Ultra-high resolution imaging by fluorescence photoactivation localization microscopy," *Biophysical Journal* **91**, 4258–4272 (2006)

[8] M. Rust, M. Bates and X. Zhuang, "Sub-diffraction-limit imaging by stochastic optical reconstruction microscopy (STORM)," *Nature Methods* **3**, 793–796 (2006)

[9] Y. Gambin, O. Legrand and S. R. Quake, "Microfabricated rubber microscope using soft solid immersion lenses," *Applied Physics Letters* **88**, 174102 (2006)

[10] D. Lange, C. W. Storment, C. A. Conley and G. T. A. Kovacs, "A microfluidic shadow imaging system for the study of the nematode *Caenorhabditis elegans* in space," *Sensors and Actuators B*, **107**, 904–914 (2005)

[11] S. Kwon and L. P. Lee, "Micromachined transmissive scanning confocal microscope," *Optics Letter*, **29**, 706–708 (2004)

[12] A. Chediak, Z. S. Luo, J. Seo, N. Cheung, L. P. Lee and T. D. Sands, "Heterogeneous integration of CdS filters with GaN LEDs for fluorescence detection microsystems," *Sensors and Actuators A*, **111**, 1–7 (2004)

[13] C. Oh, S. O. Isikman, B. Khademhosseini and A. Ozcan, "On-chip differential interference contrast microscopy using lensless digital holography," *Optics Express*, **18**, 4717–4726 (2010)

[14] O. Mudanyali, D. Tseng, C. Oh, S.O. Isikman, I. Sencan, W. Bishara, C. Oztoprak, S. Seo, B. Khademhosseini and A. Ozcan, "Compact, light-weight and cost-effective microscope based on lensless incoherent holography for telemedicine applications," *Lab on a Chip*, **10**, 1417–1428 (2010)

[15] D. Tseng, O. Mudanyali, C. Oztoprak, S.O. Isikman, I. Sencan, O. Yaglidere and A. Ozcan, "Lensfree microscopy on a cell-phone," *Lab on a Chip*, **10**, 1787–1792 (2010)

[16] D. N. Breslauer, R. N. Maamari, N. A. Switz, W. A. Lam and D. A. Fletcher, "Mobile phone based clinical microscopy for global health applications," *PLoS ONE* **4** (7), e6320 (2009)

[17] M. Shotton, "Confocal scanning optical microscopy and its applications for biological specimens," *Journal of Cell Science* **94**, 175–206 (1989)

[18] US Patent Number 3,013,467 (1961)

[19] J. Wu, X. Cui, G. Zheng, Y. M. Wang, L. M. Lee and C. Yang, "Wide field-of-view microscope based on holographic focus grid illumination," *Optics Letters* **35**, 2188-2190 (2010)

[20] J. Wu, G. Zheng, Z. Li and C. Yang, "Focal plane tuning in wide-field-of-view microscope with Talbot pattern illumination," *Optics Letters* **36**, 2179–2181 (2011)

[21] M. Oheim, "High-throughput microscopy must re-invent the microscope rather than speed up its functions," *British Journal of Pharmacology* **152**, 1–4 (2007)

[22] J. Ho, A. V. Parwani, D. M. Jukic, Y. Yagi, L. Anthony and J.R. Gilbertson, "Use of whole slide imaging in surgical pathology quality assurance: design and pilot validation studies," *Human Pathology* **37**, 322–331 (2006)

[23] X. Heng, D. Erickson, L. R. Baugh, Z. Yaqoob, P. W. Sternberg, D. Psaltis and C. Yang, "Optofluidic microscopy: A method for implementing high resolution optical microscope on a chip," *Lab on a Chip* **6**, 1274–1276 (2006)

[24] X. Cui, L. M. Lee, X. Heng, W. Zhong, P. W. Sternberg, D. Psaltis and C. Yang, "Lensless high-resolution on-chip optofluidic microscopes for Caenorhabditis elegans and cell imaging," *Proceedings of the National Academy of Science of the United States of America* **105**, 10670–10675 (2008)

[25] J. Wu, X. Cui, L. M. Lee and C. Yang, "The application of Fresnel zone plate based projection in optofluidic microscopy," *Optics Express* **16**, 15595–15602 (2008)

[26] S. Pang, H. Chao, L.M. Lee and C. Yang, "Fluorescence microscopy imaging with a Fresnel zone plate array based optofluidic microscope," submitted to *Lab on a Chip* (2011)

[27] D. Di Carlo, "Inertial microfluidics," *Lab on a Chip* **9**, 3038–3046 (2009)

[28] D. Di Carlo, D. Irimia, R. G. Tompkins and M. Toner, "Continuous inertial focusing, ordering, and separation of particles in microchannels," *Proceedings of the National Academy of Science of the United States of America* **104**, 18892–18897 (2007)

[29] D. Di Carlo, J. F. Edd, K. J. Humphry, H. A. Stone and M. Toner, "Particle segregation and dynamics in confined flows," *Physical Review Letters* **102**, 094503 (2009)

[30] C. M. Ho and Y. C. Tai, "Micro Electro Mechanical Systems (MEMS) and fluid flows," *Annual Review of Fluid Mechanics* **30**, 579–612 (1998)

[31] C. M. Ho and Y. C. Tai, "Review: MEMS and its applications for flow control," *Journal of Fluids Engineering* **118**, 437–447 (1996)

[32] S. R. Quake and A. Scherer, "From micro to nano fabrication with soft materials," *Science* **290**, 1536–1540 (2000)

[33] M. A. Unger, H. P. Chou, T. Thorsen, A. Scherer and S. R. Quake, "Monolithic microfabricated valves and pumps by multilayer soft lithography," *Science* **288**, 113–116 (2000)

[34] D. C. Duffy, J. C. McDonald, Olivier J. A. Schueller, and G. M. Whitesides, "Rapid prototyping of microfluidic systems in poly(dimethylsiloxane)," *Analytical Chemistry* **70**, 4974–4984 (1998)

[35] D. C. Duffy, O. J. A. Schueller, S. T. Brittain and G. M. Whitesides, "Rapid prototyping of microfluidic switches in poly(dimethyl siloxane) and their actuation by electroosmotic flow," *Journal of Micromechanics Microengineering* **9**, 211–217 (1999)

[36] Y. Xia and G. M. Whitesides, "Soft lithography," *Annual Review of Material Science* **28**, 153–184 (1998)

[37] D. Psaltis, S. R. Quake and C. Yang, "Developing optofluidic technology through the fusion of microfluidics and optics," *Nature* **442**, 381–386 (2006)

[38] Y. Xia, E. Kim, X.-M. Zhao, J. A. Rogers, M. Prentiss and G. M. Whitesides, "Complex optical surfaces formed by replica molding against elastomeric masters," *Science* **273**, 347–349 (1996)

[39] O. J. A. Schueller, D. C. Duffy, J. A. Rogers, S. T. Brittain and G. M. Whitesides, "Reconfigurable diffraction gratings based on elastomeric microfluidic devices," *Sensor and Actuator A*, **78**, 149–159 (1999)

Chapter 2: Implementation of Optofluidic Microscopy

In the previous chapter, I briefly reviewed the development and characteristics of optical microscopy. I have also summarized the importance of our effort to miniaturize conventional microscopy by strategic integration of optics and microfluidics technology. The OFM imaging method can be defined as a miniaturized optical scanning microscopy technique which utilizes a microfluidic flow for sample translation. The motion control on biological samples flowing in the microfluidic channel is critical for artifact- and distortion-free OFM image formation. In this chapter, I will first discuss the imaging formation mechanism of OFM systems. OFM imaging can employ either a 1-D array or a 2-D grid for image formation. I will further address the optical resolution and sampling issues in OFM imaging. In the second part, I will present several microfluidic flow strategies we used for sample translation in OFM imaging and discuss their applications in handling different biological samples.

2.1 Imaging Formation

OFM is based on scanning microscopy. The information from the sample object is revealed point by point through means of light, and this point-wise optical information is mapped to and recorded by the imaging detector in a systematic manner over time. The entire field of view of the image is then reconstructed from this set of point-wise optical information. As in any kind of scanning microscopy, there are two main parameters that fundamentally determine the final image quality: optical resolution and sampling.

The situation is like this: We hold a flashlight and point it into a dark forest. How fine the light beam from the flashlight is spotting on the trees will determine how good the resolution is. How fast we scan the flashlight in order to discern the whole picture of the forest will determine the sampling rate. If we allow ourselves to hold more flashlights to form a line array or even a 2-D grid of light spots on the trees, we will be able to discern the entire field of view of the forest more efficiently. In the first section of this chapter, we will discuss the image formation characteristics of the OFM imaging scheme.

2.1.1 Optical Resolution

OFM imaging can be constructed in different modes: collection, illumination, or a combination of both. These three modes lead to different OFM configurations and resolution characteristics. In collection mode, a plane wave is used directly as the illumination. Light transmitted through, and absorbed or scattered by the biological sample will be collected by a set of submicron sized apertures fabricated on CMOS imaging sensor pixels. In a more elaborated scheme, a set of focusing elements, FZP units, are fabricated and aligned with the collection apertures underneath to relay light from the sample focal plane to the collection apertures on the CMOS imaging sensor pixels. In both schemes, the size of the collection apertures fundamentally limits the best optical resolution of the OFM image we can achieve. The collection mode OFM systems will be studied in Chapter 3. In illumination mode, light is modulated by optical elements before it impinges on the biological samples flowing in the microfluidic channel. Undressed CMOS pixels are used to collect light from the biological sample directly. In this case, the optical resolution will be primarily limited by the optical elements, such as the holographic plate or the FZP units, used in illumination modulation. We will discuss this scheme in detail in Chapter 4. We notice that it is possible to combine the use of both illumination and collection optics in OFM device construction, and this potentially leads to a substantial improvement in both lateral and axial optical resolution and SNR. Such scheme forms the basis for building a confocal OFM system which enables optical sectioning capability in OFM imaging. Preliminary results from this effort will be discussed in Chapter 5.

2.1.2 Sampling Problem

OFM imaging is a miniaturized optical scanning microscopy technique. The sampling point or points are set to be static and we move the biological samples for scanning. The light intensity through the sampling point is collected and measured by a CMOS imaging sensor for image formation. If there is only one sampling point, the specimen has to be raster scanned to discern the entire field of view of the object. This approach requires the sample to move back and forth in the microfluidic channel. At the same time, the sample has to maintain a constant orientation at each translation. This requires a rather complicated microfluidic control mechanism, (which is not trivial) to be integrated in on-chip imaging. Alternatively, we can impose a 1-D line of sampling points which spans the entire width of the target sample for OFM imaging. In this case, a single unidirectional sample translation at a slanted angle to that sampling line array is sufficient for the whole field of view in OFM image acquisition. This scheme actually forms the basis of the first OFM implementation. It is possible to add another dimension in OFM imaging spatially by utilizing a 2-D grid sampling point array. We can imagine this implementation by folding several 1-D lines of sampling points into a 2-D grid array. In this case, several sampling points can scan and acquire information on different parts of the target object at the same time during the sample translation, thus reducing the total acquisition time and the length of the sampling array. The advantage of this design only exists when the size of the target object is larger than the actual CMOS imaging sensor pixel size; otherwise, the 2-D grid is effectively only using one line array at each sample translation. This approach also involves a more complicated algorithm for image reconstruction and is more vulnerable to artifacts due to the crosstalk between adjacent sampling lines if they are not sufficiently separated. In many OFM applications, the size of biological samples is about 10 μm and we usually have to separate them by about 10 μm to prevent

crosstalk. This is the reason why the 2-D grid sampling is not an attractive option. However, the 2-D grid approach has proved to be very successful and efficient for wide field-of-view applications [1].

Here I will explain the formulation of the 1-D line array sampling scheme in an OFM system. Figure 2.1.2 is an illustration of the sampling scheme in OFM imaging. The sampling along x-direction is determined by both the flow speed of the biological sample along the flow direction, U, and the readout frame rate, f. The sampling along y-direction is determined by the lateral distance between the apertures across the flow direction (x-direction). This lateral distance can be found by $L\sin\theta$, where the L is distance between neighboring apertures and θ is the tilted angle between the line aperture array and the microfluidic channel. Thus, the virtual grid density of OFM image formation can be found as follows, where δx is the grid density along x-direction and δy is the grid density along y-direction:

$$\delta x = \frac{U}{f} \qquad\qquad (2\text{-}1)$$

$$\delta y = L\sin\theta \qquad . \qquad (2\text{-}2)$$

To prevent aliasing artifacts in sampling, the grid density (δx and δy) is chosen to be half of the optical resolution limit of the sampling point, in order to satisfy Nyquist criteria. For a collection-aperture-based OFM system, this optical resolution limit is primarily determined by the diameter of the aperture and the aperture/biological sample separation. For an illumination-mode OFM system, the optical resolution is determined by the size of the focused spot. The distance between the apertures L is usually set to the minimum possible value before cross-talk between successive sampling points starts to occur. This can ensure that the distance for OFM image acquisition is as short as possible before significant cell rotation or tumbling starts to occur.
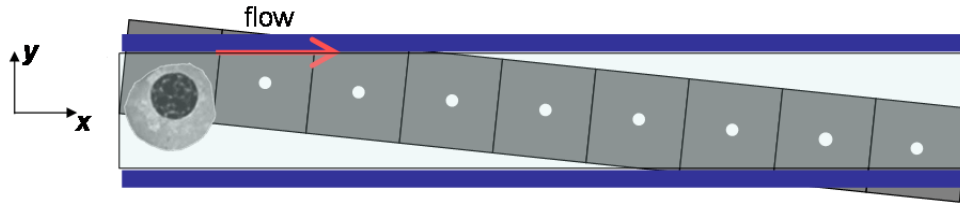
Figure 2.1.2 An illustration of 1-D slanted-line array sampling scheme in OFM imaging

One interesting point deserving of mention is that although the OFM device samples the biological specimen temporally by each OFM aperture in the *x*-direction and spatially by different OFM apertures in the *y*-direction, the image sampling schemes in these two directions are essentially equivalent to each other. Last, I would like to point out that the above formulation is good if we treat our samples as 2-D objects. It is possible to extend this sampling scheme to 3-D, by superposing this sampling line array successively along the flow direction at different depths. This implementation can be achieved in FZP-collection-, illumination- and confocal-mode OFM systems, where in principle we can position our optical sampling points at any desired position in the microfluidic channel by correct parameter design. To render good OFM imaging sampling, the vertical grid density δz in 3-D OFM imaging should be chosen to be half of the depth of focus of the focusing optical element.

2.2 Microfluidics for Sample Transport

In OFM imaging, biological samples are delivered by a microfluidic flow for optical scanning in image formation. The motion of biological samples flowing in the microfluidic channel directly determines the image quality. A constant, rotation- and tumbling-free, rigid translation is highly sought in different OFM imaging schemes. In fact, the size and shape of the biological entity, the fluid medium, and the geometry of the microfluidic channel all play an important role in affecting the motion of target objects flowing in the microfluidic channel. Microfluidics is a highly diversified field ranging from fundamental physics to biotechnology applications; the scope of the material in this section will be limited to considerations in adapting microfluidic techniques which most suit for flow-control applications in OFM imaging. Several microfluidic flow mechanisms have been studied and investigated in experiments to improve the versatility of OFM systems to image different biological samples without serious discrepancy in image formation.

Before we discuss different flow-driven mechanisms commonly used in microfluidics, we notice there is a fundamental limit on the microscopic motions of suspended particles when there is no external force acting on the particles. This thermally induced random fluctuation on any rigid object suspended in fluid medium is termed Brownian motion. The suspended particles in a liquid medium are being bombarded by surrounding liquid molecules, causing them to vary in direction many millions of times per second. The path of this fluctuation is a random walk process and very numerically expensive to investigate microscopically. Einstein suggested a macroscopic concept, diffusive flux, to model Brownian motion by assuming a Gaussian distribution on the random displacement of an individual suspended particle at each time step.

The mean square displacement in three dimensions is given by:

$$\left\langle r^2 \right\rangle = 6Dt \tag{2-3}$$

where t is the time duration of observation and D is the translational diffusion coefficient of the suspended particles.

$$D = \frac{kT}{6\pi\mu a} \tag{2-4}$$

where k is the Boltzmann constant (1.38×10^{-23} m^2·kg·s^{-2}·K^{-1}), T is the temperature (in absolute scale), μ is the dynamic viscosity of the medium, and a is the radius of the suspended particle. This equation is commonly referred to as the Stokes-Einstein equation, which represents the balance between the thermal-induced displacement of the suspended particles and the viscous drag from the surrounding fluid medium. Combining equation between Equations (2-3) and (2-4), the root-mean-square displacement for suspended particles is given as follows:

$$\left\langle r^2 \right\rangle^{1/2} = \sqrt{\frac{kTt}{\pi\mu a}} \tag{2-5}$$

For a 10 μm polystyrene microsphere with radius a = 5μm, suspended in water (μ = 1.002×10^{-3} kg·m^{-1}·s^{-1}), at room temperature (T = 293K), with the OFM device operating at an imaging sensor pixel exposure time of t = 0.5 ms, the root mean square displacement of the suspended microsphere is calculated to be 10 nm. This value is substantially smaller than the optical resolution of OFM images. During the 0.4 seconds of OFM image acquisition, the three-dimensional root-mean-square displacement due to the Brownian motion is 0.3 μm, which may

potentially lead to distortion and blur in OFM image formation. However, this value is still substantially small compared to the overall size of the target object. Besides the translational motion of suspended particles, the Brownian motion will also introduce rotational fluctuation on the suspended particles, causing them to change in orientation from time to time. Based on a similar calculation, this rotational fluctuation does not effectively alter the OFM image formation. Interested readers are referred to [2], which provides an excellent explanation of this problem.

I have evaluated the effect of Brownian motion on a microsphere with diameter of 10 μm, which is quite typical for many biological cell imaging applications in OFM prototypes. What about objects of different size? Referring to Equation (2-5), the root-mean-square fluctuation caused by Brownian motion is linearly related to the root of the observation time, while the image acquisition time scales linearly with the object size. Therefore, it is logical to expect that the smaller samples are more subjected to both image blur and distortion than large objects, assuming the OFM device is operating with the same frame rate.

Despite its simplicity, the above analysis provides a theoretical background on the feasibility of using fluid medium to transport biological samples for OFM applications even with the existence of Brownian motion. In fact, we have made one important assumption in the Brownian motion derivation and analysis: that there is no external forcing acting on the suspended objects. It is possible to apply external force, for example, electric or optical force [3], to suppress the Brownian motion and stabilize the translational motion of biological samples in OFM imaging. It is also possible to use a working fluid with higher viscosity to suppress the effect of Brownian motion (for example, dissolving sucrose or adding glycerol to the sample solution). This will lead to several orders of increase in viscosity. However, this approach may

cause osmotic shock to the biological cells, possibly causing damage in the morphology of the biological samples. Furthermore, the change in the refractive index of the sample solution will affect the image contrast in OFM imaging.

2.2.1 Pressure-Driven Flow

In the previous section, I have evaluated the effects of Brownian motion, which causes both translational and rotational fluctuations in biological sample translation in OFM imaging. In the following sections, I will focus more on the fluid and flowing object interactions, based on our knowledge of continuum fluid mechanics, in conjuction with experimental findings.

Microfluidic flow is characterized by low Reynolds numbers, typically smaller than unity. In this regime, the incompressible Navier-Stokes equation for Newtonian fluid can be simplified to a Stokes flow equation by neglecting the convection term:

$$\nabla p = \mu \nabla^2 \boldsymbol{u} \tag{2-6}$$

where ∇p is the gradient of the pressure, μ is the dynamic viscosity of the fluid, and $\boldsymbol{u}$ is the velocity field of the fluid. Together with the continuity equation,

$$\nabla \cdot \boldsymbol{u} = 0 \tag{2-7}$$

defines the fluid flow. Fluid flows in this limit are attached and the streamlines are parallel with the channel geometry. This system of governing equations is linear, so the flow-field solutions are superposable and reversible. In viscous liquid flows, a no-slip boundary condition is usually imposed parallel to the flow direction at the channel wall interface, and a no-penetration boundary condition through the walls is imposed normal to the flow direction. In micro-scale fluid mechanics, usually microfluidic channels are manufactured with a constant rectangular or square cross section, primarily due to convenience in microfluidic fabrication. The liquid flow is unidirectional, so that only the velocity component in the streamwise (x-direction) direction is

non-zero when a constant pressure gradient is applied along that direction. This assumes that the microfluidic channel flow is fully developed and free from the entrance effect, in which case the velocity is constant in the streamwise direction. Under this condition, Equation (2-6) can be further reduced to a two-dimensional Poisson equation:

$$0 = -\frac{\partial p}{\partial x} + \mu\left(\frac{\partial^2 u}{\partial y^2} + \frac{\partial^2 u}{\partial z^2}\right) \tag{2-8}$$

where u is the streamwise velocity distribution and is a function of y and z for a rectangular cross section microfluidic channel:

$$u(y,z) = \frac{16b^2}{\mu\pi^3}\left(-\frac{dp}{dx}\right)\sum_{i=1,3,5...}^{\infty}(-1)^{(i-1)/2}\left[1 - \frac{\cosh(i\pi y/2b)}{\cosh(i\pi h/2b)}\right]\frac{\cos(i\pi z/2b)}{i^3} \tag{2-9}$$

where b is half the channel width and h is half the channel height and ($-b \leq y \leq b$ and $-h \leq z \leq h$). The above equation is rather complicated and no longer intuitive for visualizing the velocity profile. It actually represents a two-dimensional parabolic profile with peak velocity along the channel middle axis and zero velocity at the side walls [4]. Low Reynolds-number flow, with velocity **U**, exerts a drag force, **F**, on suspended particles, resulting in a translational motion. The drag force exerted on the body depends on the shape and orientation on the object [5, 6]:

$$F_i = 6\pi\mu R_{ij}U_j \tag{2-10}$$

where R_{ij} is termed the translational tensor which is solely determined by the size, shape, and orientation for a rigid body.

For a rigid perfect sphere, in which we can assume that the internal viscosity approaches infinity, the viscous drag is parallel to the translational direction, leading to the famous classical Stokes drag law:

$$F = -6\pi\mu a U \ .$$
(2-11)

Notice there is a negative sign in the expression. This indicates that drag force is frictional in nature. This resistance force always acts against the flow direction at the fluid/suspended particle interface. In pressure-driven flow, given the parabolic velocity profile, particles dispersed at different positions in the microfluidic channel will experience different magnitudes of drag force and move at different translational speeds. In addition, particles with different sizes and shapes will also affect the translational velocity. In fact, this forms the basic working principle of hydrodynamic chromatography. Another important parameter of interest, which is even more related to OFM applications, is the couple or torque experienced on the particles by the flow field interaction, resulting in the rotational motion on the suspended objects. In fluid mechanics, the vorticity or the local angular rate of rotation of the flow can be found by taking the curl of the velocity field:

$$\boldsymbol{\omega} = \nabla \times \boldsymbol{u} \ .$$
(2-12)

The torque $\mathbf{T}$ about the center of rotation of a body with angular velocity of $\boldsymbol{\omega}$ can be expressed in tensor form as:

$$T_i = -6\mu\Omega_{ij}\omega_j$$
(2-13)

where Ω_{ij} is the rotation tensor, which again depends on the shape and size of the object. We now return to the discussion of two-dimensional pressure-driven flow, where the velocity field distribution has a parabolic profile. When we take the curl of the velocity field of pressure-driven flow as shown in Equation (2-9), there is only one point where the vorticity is exactly zero, which

is along the channel mid-axis. The net torque exerted on the object is identically zero and the object rotational motion is minimized along the channel mid-axis regardless of the shape of the object. When the suspended object is flowing off-axis, it experiences a certain degree of torque, resulting in rotational motion on the flowing objects. Take a perfect sphere as the simplest example which is isotropic with respect to rotational motion about its center; the magnitude of the rotation is not constant at different cross-section positions of the microfluidic channel. Given the parabolic velocity profile, the magnitude of vorticity is highest near the channel wall and decreases linearly to zero at the channel mid-axis. The rate of rotation also depends on the shape and orientation of the flowing object. The three-dimensional rotational motion can be studied analytically or numerically based on the rotation tensor formulation in Equation (2-13). This formulation is not trivial for complicated geometry and usually requires detailed experimental study. Here I try to provide a lay person's explanation on this. Let us take two geometries at extremes for benchmark comparison. The first object is a sphere (for example, a pollen spore), and the second object is a slender ellipsoid with the longest axis orientated along the flow direction (for example, a *C. elegans* worm). Assuming they are flowing at the same off-axis position in the microfluidic channel, the difference in the velocity on the upper and lower apex of the perfect sphere is much larger than that of the slender ellipsoid. Thus, a much larger torque or rotational motion is imposed on that sphere compared to that of the slender ellipsoid. The above discussion focuses only on the Stokes drag interaction between the fluid and suspended objects. When the biological samples are translating in close proximity to the channel wall, the samples will experience friction or other interaction force, such as electrostatic force, from the solid channel wall. This is probably the situation for the implementation of the first prototype of the OFM device, where the biological samples have to be confined by the height of the microfluidic channel so that the samples are flowing close enough to the collection apertures fabricated on the channel bottom to ensure good image resolution. The channel surface is thus modified with a lubrication layer, polyethylene glycol (PEG), to minimize the frictional interaction between the

translating biological samples and the channel surface in order to ensure a smooth microfluidic flow. The details of PEG surface modification are explained in Appendix A1.

I have conducted a set of experiments to study the flow motion of biological samples for OFM applications. I have fabricated a PDMS-on-glass microfluidic channel for the purpose of easy flow visualization. The microfluidic channel is mounted on an inverted optical microscope (Olympus IX71) under a 10× objective. The dimensions of the microfluidic channel are 40 μm in width, 9.7 μm in height, and 2.5 mm in length. The region of interest is selected as the middle of the microfluidic channel, so that the flow field is free from entrance effect. The pressure difference is generated in the PDMS microfluidic channel through the use of surface tension. To accomplish this, I add an additional drop of the sample solution onto the input port. Since native PDMS is highly hydrophobic, this drop beads up to form a hemispherical shape with a radius of about 0.5 mm. The associated surface tension then creates a Young–LaPlace pressure up to several hundred Pa at the inlet [7]. This pressure difference between the inlet and outlet then generates a mean fluid flow velocity with a magnitude of a few hundred microns per second in our microfluidic channel configuration. This fluid velocity will drag the targets to flow inside the microfluidic channel, and the translation speed of the samples is proportional to this flow speed. I find that the flow velocity as generated by this means for an individual biological entity is sufficiently constant for OFM application, as the OFM image acquisition time for each target is fairly short (typically less than 1.0 second). The flow speed may vary over time as fluid drains out of the beading drop and alters the surface tension. However, this change occurs over a much longer timescale. As long as I am able to measure the flow speed of each individual target independently, this variation is unimportant.

I used biological samples of *G. lamblia* cyst, which has an oval shape, about 7–10 μm in width and 8–13μm in length [8] as a benchmark for OFM imaging applications. The sample preparation is described in Appendix A1. The channel height is made smaller than the average length of the *G. lamblia* cysts in order to restrict the out-of-plane rotational motion of the cysts. We adopt this design for two purposes. First, three-dimensional rotational motion study of suspended particles is very difficult to accomplish. To achieve that, a high-power confocal microscope with high-speed image capturing capability and short depth of field is required. Sub-cellular image resolution is required in order to avoid ambiguity in image analysis. Second, this configuration is closer to the real situation in the implementation of the first prototype of aperture-based OFM system, in which a shallow microfluidic channel is required to confine the samples close enough to the channel floor to ensure good image resolution. In experiment, we found that the flow motion of the *G. lamblia* cysts is quite consistent with the prediction of the analysis. The vorticity generated by the parabolic flow profile creates a significant torque on the samples and, thereby causes the cysts to rotate as shown in Figure 2.2.1(a). The cysts rotate with opposite orientations (clockwise versus counter-clockwise) when flowing along the upper or lower half of the microfluidic channel while driven by pressure since the direction of vorticity vector changes sign when it crosses the channel mid-axis ($y = 0$). We also observed that the *G. lamblia* cyst tends to rotate more and translate slower when it is flowing near the side wall. For the cysts flowing close to the channel mid-axis ($y = 0$), minimum or zero rotational motion is observed, since the local vorticity vanishes in that location.

Figure 2.2.1 An experimental illustration of the microfluidic motion of a *Giardia* cyst driven by

pressure difference

2.2.2 Electrokinetic-Driven Flow

The applications of electrokinetic technology in microfluidic systems have been studied and implemented extensively since the 1990s in theory, numerical simulations and experiments. These findings resulted in thousands of publications and the field of electrokinetic microfluidics remains vibrant and continues to emerge. With the limits of the context, I will not be able to discuss the details of electrokinetic phenomena in liquid medium. The material covered in this section will remain simple and focus on the application to the flow-motion control of biological samples in OFM applications.

To understand electrokinetic phenomena, the first topic for discussion is the electrical interaction between the solid and liquid interface. Generally speaking, solid surfaces are likely to carry electrostatic charge, such as an electric surface potential, due to broken bonds and surface charge traps [9]. When an electrolyte solution is brought into contact with such a solid boundary, the surface charge attracts the counter-ions in the liquid, establishing an electric field. The arrangement of the electrostatic charges on the solid surface and the balancing charges in the liquid is called the electric double layer, EDL [10]. Counter-ions are strongly attracted to the surface, forming an immobile compact layer at the solid/liquid interface. Outside this layer, the distribution of the counter-ions away from the interface decays within the diffuse layer with a characteristic thickness known as the Debye length-scale, which is inversely proportional to the square root of the liquid ionic concentration. The electric potential at the boundary between the compact and diffuse layers is called zeta potential. Typically, Debye length in dilute electrolyte is thinner than 10 nm [11] and in distilled water is about 100 nm. Compared with the dimension of

most microfluidic systems (including OFM systems), in which the characteristic length scale is on the order of tens of microns, we can simply adopt the thin EDL assumption.

A microfluidic channel with fixed charges at the walls generates a mobile 'sheath' of ions in the fluid. Under an externally applied electric field parallel to a surface with net charge density, the mobile ions move in a direction parallel to the wall. The movement of this sheath induces the motion of the bulk liquid, due to shear stress, as if the walls of the channel were sliding at a velocity directly proportional to both the magnitude of the applied field and the mobility of the ions. The ion mobility is a function of the surface charge density, liquid ionic strength, liquid viscosity, and permittivity. This is known as electro-osmotic flow.

Most biological samples carry a net charge. When a charged particle is suspended in an external electric field, it experiences a Coulumb force. In addition to the electrical force, once the charged particle starts to move in the fluid medium, it experiences Stokes drag, acting opposite to the direction of the electrical force. These two forces acting on the suspended particle will eventually balance each other and the particle will translate to a constant velocity. The electrophoretic mobility is determined by the electric charge and the frictional properties of the suspended particle. This phenomenon is known as free-solution electrophoresis [12].

Electrokinetic-based flow is a better flow control mechanism than the pressure-driven flow for a number of reasons: 1) The electro-osmotic flow in thin EDL limit has a plug-like profile [2] and the vorticity outside the EDL is zero, thus there is no generation of a significant torque on a target in the flow stream. 2) The net electric charge on a biological target interacts

with the imposed electric field to pull the target towards the oppositely charged pole (electrophoretic force). This interaction acts as a net body force exerted on the cell and should not cause any rotation. 3) The non-uniform electric charge distribution (dipole moments) on a target interacts with the imposed electric field to reorient the target in order to achieve the most stable state; this electro-orientation effect effectively holds the target into a single orientation during the entire flow duration [13].

To study the impact of electrokinetic-based microfluidic flow on *G. lamblia* cysts, we set up an experiment by generating a constant electric field in the microfluidic channel. I implemented this set of experiments by inserting a pair of external platinum electrodes into the input and output ports. Next, we connected the electrodes to a low-voltage power supply (E3617A, HP). A multi-meter was also connected to the setup to measure the current level. A constant voltage of 30 V (electric field strength is $E \approx 10$ V/mm) was applied to the electrodes. No destruction or disruption of the poly(methyl methacrylate) (PMMA) protection layer was observed if the applied voltage was kept below this level, since both the *G. lamblia* cysts [14] and the microfluidic channel walls carried net negative charges at near-neutral pH values. This implied that the resulting electrophoretic force and electro-osmostic flow would act in opposite directions. We observed that the net electrokinetic flow of the cysts was opposite to the direction of applied electric field; this indicated that the electrophoretic force was stronger than the electro-osmotic flow in our experiment setting. We found that the net electrokinetic flow speed was linearly proportional to the applied electric field. In addition, most *Giardia* cysts settled into their final flow orientation by electro-orientation effect before flowing more than 200 μm in the microfluidic channel, and maintained a constant orientation during its translation in the microfluidic channel, as shown in Figure 2.2.1.1. A relatively small electric field ($E = 10$ V/mm) was sufficiently strong to create an electro-orientation force that held most cells at a constant

orientation during the translation. This electric strength was much lower than the critical value that would cause cell lysis [15]. Occasionally, we observed that a residual pressure can build up due to due to inbalance of the liquid in the inlet and outlet ports after a prolonged experiment. However this residual pressure difference did not cause significant rotation of the biological samples. We believe that the reason for this was that the DC electro-orientation effect is strong enough to suppress the rotational motion causing the pressure difference.
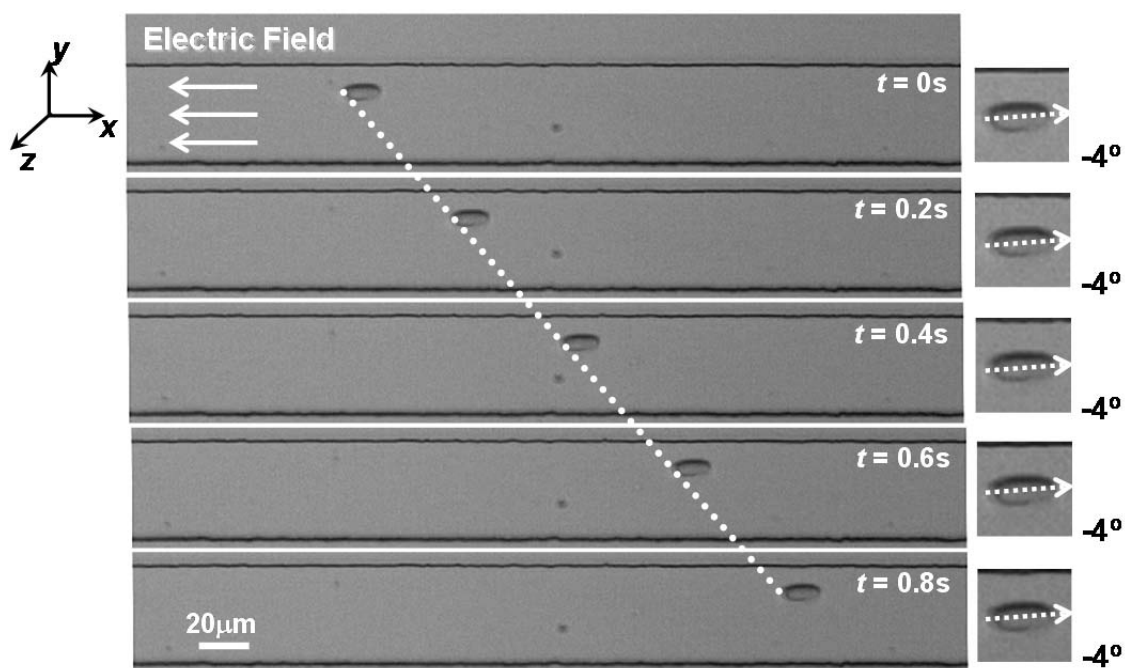
Figure 2.2.2.1 An experimental illustration of the microfluidic motion of a *Giardia* cyst driven by DC electrokinetics

The statistical distribution of cell-rotation events was also studied by driving 100 *Giardia* cysts singly in a microfluidic channel under pressure-based and electrokinetic-based flow. Figure 2.2.1.1 plots the number of cysts versus the extent of the rotation (over a flow distance of 300

μm). We can see from the plot that, under pressure-based flow, the cyst rotation was significant and broadly distributed. In comparison, the extent of cyst rotation under electrokinetic-based flow was small. In the context of this current OFM design, a rotation of 5° during the passage of the cyst across the aperture array does not create significant image distortions. Experimentally, we find that 70% of the cysts experienced rotations under pressure-driven flow while only 5% of the cysts experienced significant rotations under effect of electrokinetics. This indicates that the use of DC electrokinetics is an effective way to suppress rotational motion of cells in OFM systems.
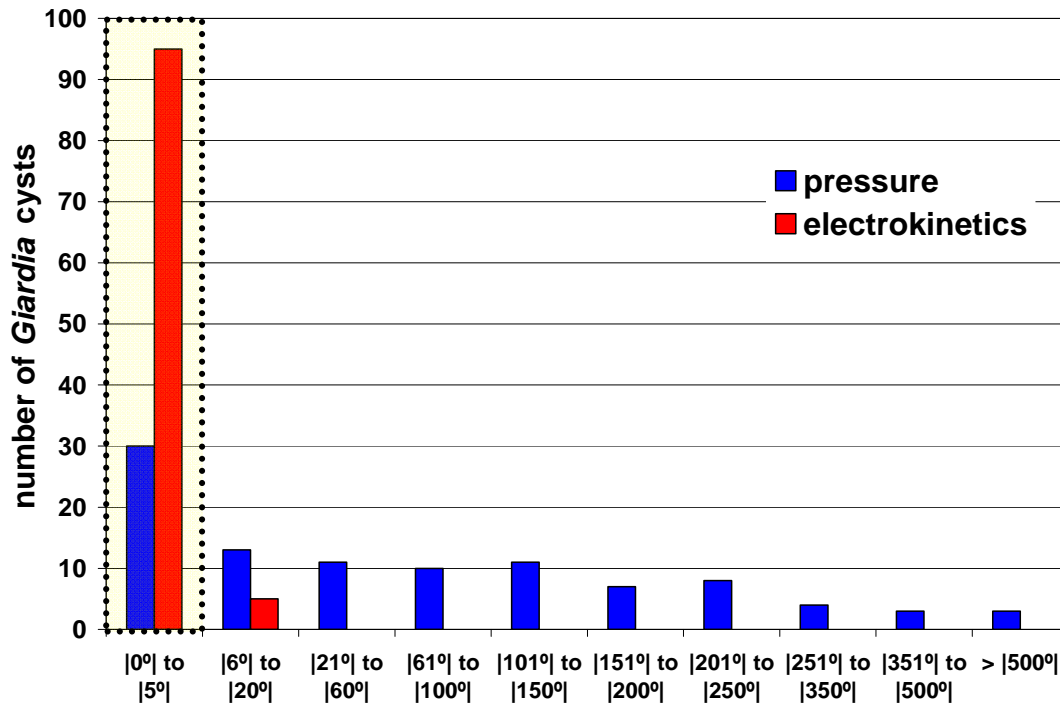
Figure 2.2.2.2 A plotting of the statistical distribution of sample rotation under pressure-based and electrokinetic-based microfluidic flow. The horizontal axis quantifies the magnitude of rotation after 300 μm of travel in the microfluidic channel.

In another set of experiments, mulberry pollen spores were suspended to form the sample solution. Upon switching the direction of the applied electric field along the microfluidic channel, a pollen spore moved in the opposite direction and its orientation reached a steady state in less than 100 μm. In summary, the use of DC electrokinetics provides an alternate, simple, and direct way to actuate microfluidic flow. This method involves imposing an electric field along the microfluidic flow channel axis to generate an electro-osmotic flow, an electrophoretic force, and an electro-orientation force on the biological sample over a constant, uniform electric field. The main purpose of the use of electrokinetics in OFM systems is to ensure a rotation-free translation during the image acquisition process.

2.2.3 Gravity-Driven Flow

Gravity has been utilized by the microfluidic community in particle sorting of different sizes [16]. Instead of placing the microfluidic channel horizontally, the device is operated upright, orientating vertically so that when the specimen solution is injected into the inlet, the solution wets the microfluidic channel and the suspended objects are continuously pulled into the channel by gravity. This approach has the advantage of eliminating the need for bulky external pumps. For many biological specimens or suspended particles, their density is higher than that of the fluid medium, thus the suspended object will experience a sedimentation force and fall freely along the direction of gravity to the bottom; the net force, F_{net}, acting on the suspended object is a force balance between gravity and the buoyancy force on the suspended object, and is given by:

$$F_{net} = (\rho_{object} - \rho_{fluid})V_{object}g \tag{2-14}$$

where ρ_{object} represents the density of the suspended object, ρ_{fluid} is the fluid density, V_{object} is the volume of the suspended particle, and g is the gravitational acceleration constant (9.8 m·s^{-2}). In the case of low-Re-number flow, as the suspended particle velocity continues to increase in free fall, the viscous drag opposing the motion will also increase and eventually match with the sedimentation force, resulting in an equilibrium so that the suspended object is no longer in acceleration. Note that in Equation (2-14), the sedimentation force depends on the suspended object density and volume. This flow actuation approach is more appropriate for OFM imaging on biological specimens with higher density and relatively large size (for example *C, elegans*). The OFM device is usually operated with the microfluidic channel tilting at a certain angle. By doing this, a certain portion of the gravitational force component will pull the biological samples to the floor of the microfluidic channel during its downward direction translation to ensure a close

proximity to the OFM apertures on the channel, which is desirable for good image resolution in the implementation of the single-layer aperture-based OFM prototype. We demonstrated the successful OFM imaging on elongated objects using this flow method. However, gravity-driven flow is not suitable for spherical/ellipsoidal species, since the gravitational force acting on the body of the sample and the frictional force between the sample and channel wall will form a torque causing the object to rotate.

REFERENCES

[1] J. Wu, X. Cui, G. Zheng, Y. M. Wang, L. M. Lee and C. Yang, "Wide field-of-view microscope based on holographic focus grid illumination," *Optics Letters* **35**, 2188–2190 (2010)

[2] R. F. Probstein, Physicochemical Hydrodynamics: An Introduction, Wiley-Interscience, 2nd edition (2003)

[3] X. Heng, E. Hsiao, D. Psaltis and C. Yang, "An optical tweezer actuated, nanoaperture-grid based Optofluidic Microscope implementation," *Optics Express* **15**, 16367–16375 (2007)

[4] N.-T. Nguyen and S. T. Wereley, Fundamentals and Applications of Microfluidics, Artech Print on Demand, 2nd edition (2002)

[5] J. Happel and H. Brenner, Low Reynolds Number Hydrodynamics: With Special Applications to Particulate Media, Springer, 1st edition (1983)

[6] G. K. Batchelor, An Introduction to Fluid Dynamics, Cambridge University Press (2000)

[7] G. M. Walker and D. J. Beebe, "A passive pumping method for microfluidic devices," *Lab on a Chip* **2**, 131–134 (2002)

[8] L. Zhu, Q. Zhang, H. Feng, S. Ang, F. S. Chau and W. T. Liu, "Filter-based microfluidic device as a platform for immunofluorescent assay of microbial cells," *Lab on a Chip* **4**, 337–341 (2004)

[9] P. Bertrand, A. Jonas, A. Laschewsky and R. Legras, "Ultrathin polymer coatings by complexation of polyelectrolytes at interfaces: suitable materials, structure and properties," *Macromolecular Rapid Communications* **21**, 319–348 (2000)

[10] R. J. Hunter, Zeta Potential in Colloid Science: Principles and Applications, Academic Press (1981)

[11] A. De Leebeeck and D. Sinton, "Ionic dispersion in nanofluidics," *Electrophoresis* **27**, 4999–5008 (2006)

[12] P. D. Grossman and J. C. Colburn, Capillary Electrophoresis: Theory and Practice, CRC Press, 2nd edition (1997)

[13] M. P. Hughes, Nanoelectromechanics in Engineering and Biology, CRC Press, 1st edition (2003)

[14] S. L. Erlandsen and E. A. Meyer, Giardia and Giardiasis: Biology, Pathogenesis, and Epidemiology, Springer, 1st edition (1984)

[15] P. C. H. Li and D. J. Harrison, "Transport, manipulation, and reaction of biological cells on-chip using electrokinetic effects," *Analytical Chemistry*, **69**, 1564–1568 (1997)

[16] D. Huh, J. H. Bahng, Y. Ling, H.-H. Wei, O. D. Kripfgans, J. B. Fowlkes, J. B. Grotberg and S. Takayama, "Gravity-driven microfluidic particle sorting device with hydrodynamic separation amplification," *Analytical Chemistry* **79**, 1369–1376 (2007)

Chapter 3: Collection-mode Optofluidic Microscope

Optofluidic microscopes can be constructed at different levels of complexity which enable various functionalities in OFM imaging. We can briefly categorize OFM imaging into two modes: collection and illumination. In this chapter, I will present my effort on the integration of collection optics in OFM imaging, in which optical elements are fabricated directly on top of the imaging sensor. In collection-mode OFM imaging, the illumination light field is not modulated, i.e., a plane wave is used directly as the illumination source from the top. Light not occluded by the translating biological sample in the microfluidic channel is collected by the optical elements fabricated on the channel bottom and detected by the imaging sensor pixels underneath. In the first part of this chapter, I will mainly focus on the incorporation of single layer structure collection optics in OFM imaging. The bulk of this section will be attributed to the development of a collection aperture-based OFM prototype. In this implementation, an array of circular apertures, 500 nm in diameter, is fabricated at the center of every alternate pixel of a metal-coated CMOS imaging sensor using FIB milling. Under an incoherent white light illumination, biological specimens translating in a microfluidic channel aligned at a slanted angle with the aperture array occlude the light field, and the light intensity change is collected by the apertures fabricated on the CMOS imaging sensor pixels. This OFM prototype marks the first successful implementation of OFM system on a chip-level and it leads to the successful bright field OFM imaging of several biological samples — including *Chlamydomonas reinhardtii*, mulberry pollen spores, polystyrene microspheres, *Giardia lamblia*, and *C. elegans* — with optical resolution less than 1 μm, which is comparable to conventional optical microscopy, under a 20× objective. In the second part of this chapter, I will focus on two-layer structure construction which provides focusing ability in OFM imaging with coherent light illumination. To accomplish this, a linear array of diffractive optical lenses, the Fresnel zone plate (FZP), is fabricated on top of the OFM collection aperture array with good alignment. These two layers are

separated at a precise distance to provide space for light propagation. By careful design of zone plate parameters, an array of conjugate focus can be formed at our desired vertical position in the microfluidic channel, where only light enclosed at this location will be relayed to and collected by the CMOS imaging sensor pixel. This scheme not only enables direct focusing capability in OFM imaging, but also provides a huge advantage in the microfluidic control since biological samples do not need to translate in close proximity to the channel floor in order to ensure good image resolution. In experiment, under normal and tilted plane wave illumination, bright field and dark field OFM imaging of mulberry pollen spores, *Cyanophora paradoxa* and polystyrene microsphere are demonstrated. The image quality and contrast mechanism of the acquired OFM image will be discussed in the following sections.

3.1 Single-Layer Structure

We start the development of a compact OFM system by imposing different single-layer features on the CMOS imaging sensor pixel for light collection and modulation. We showed that bright field differential interference contrast (DIC) and dark field microscopy can be implemented under the context of OFM imaging. With a single through-hole, a bright field OFM imaging scheme can be achieved. If we impose four closely packed through-holes, this hole set forms an on-chip phase imager based on 2-D Young's interference [1]. This enables a phase-sensitive OFM device. We also showed in experiment that, given a set of concentric ring trenches around a subwavelength through-hole on a gold film with proper design parameters, the surface wave generated by the rings interferes destructively with the incident light wave and allows significant pre-detection background suppression [2]. By repeating these surface-wave-enabled dark field apertures to a 1-D array, a compact dark field OFM imaging device can be built for sensitive near-surface detection. However, since there is only one degree of freedom in the above optical designs, it is difficult to incorporate focusing capability in above prototypes. In addition, these innovations are demonstrated in off-chip manner and still rely on a bulk 4-f optical system for light relaying. Nonetheless, I believe these preliminary results have paved the road to incorporate this novel imaging scheme in OFM.

3.1.1 Using Apertures in OFM Imaging

In traditional optics, an aperture is an optical stop which allows certain part of a light beam to pass through but physically blocks other part. It is usually made of an adjustable-leaf diaphragm which controls the amount of light reaching the image plane. The use of apertures in optical imaging can be found as far back in the invention of the pinhole camera. A pinhole camera is made of a black box with a tiny hole at one side and an opening at the other side covered by a translucent screen. Light reflected or emitted from an object passes through this tiny opening and forms a real and inverted image on the screen. A similar construction is found in the operation of our human eye. The iris limits the amount of light entering our eyes and forms a real and inverted image in the retina. In an optical system for image formation, usually the aperture is placed behind an optical lens and the role of the aperture is to control the acceptance angle of a bundle of rays that come to focus in the image plane. If the aperture opening is set to be small, it only accepts collimated light. A sharp, aberration-free image will be formed along the optical axis at an extended distance of the lens focal length. If a large aperture is used, a wide angle of light ray bundles will be accepted, including the oblique light rays. In this case, a sharp image will be formed only within a short distance from a certain focal length and the image will appear blurry at other places. The above illustration is just one example of the use of aperture in optical imaging. In fact, the combination and appropriate arrangement of optical lenses and apertures can improve image sharpness and contrast, and reduce aberration. Such applications can be studied and simulated through geometry optics, which is very useful in the modern design of cameras and microscopes. The analysis is based on the assumption that the size of the pinhole and the optical path is much larger than the propagating light wavelength and neglects a large degree of the electromagnetic wave nature of light, for example, interference, diffraction, and near-field optics.

In the implementation of collection apertures in OFM systems, the role and working principle of aperture is not the same as in traditional optics, such as, the pinhole camera. The collection aperture is fabricated directly on top of the CMOS imaging sensor pixel and it effectively diminishes the photosensitive area of the imaging sensor pixels. The size of the collection apertures is usually less than 1 μm, approaching to the diffraction limit of light. In fact, the role of the collection aperture in OFM imaging is closer to that of NSOM, which is able to break the diffraction limit of light because the resolution of such devices is fundamentally limited by the aperture size, but independent of the illumination wavelength, or the numerical aperture of any lens involved [3, 4]. To understand and characterize the optical properties of OFM apertures, two sets of fundamental studies have been conducted to characterize the resolution, the depth of field, and the acceptance angle in experiments and numerical simulations for a range of size of OFM apertures [5, 6]. A summary of these findings and studies will be presented in more detail in the following sections.

3.1.2 Design and Fabrication

In this section, I will present the design and fabrication of the first on-chip collection-aperture-based OFM prototype. The planar design of the OFM device is shown in Figure 3.1.2(a). The OFM aperture array consists of a total of 120 apertures, and the dimensions of the microfluidic channel are 40 μm in width and about 2.5 mm in length. The aperture array spans the entire width of the microfluidic channel so that all biological samples passing through the device will be imaged. The channel height can be chosen to be 10 or 13 μm depending on the size of the biological samples to be imaged. This guarantees that the targets flow across the aperture array in close proximity to the channel bottom to ensure good image resolution. The channel also confines and limits the out-of-plane rotational motion of ellipsoidal objects. The microfluidic substrate is made of a transparent elastomer to facilitate optical imaging. The apertures are circular in shape, 500 nm in diameter, and are fabricated at the center of every alternate square pixel (5.2 μm in length) underneath, with a separation of 10.4 μm. The tilted angle of the array with respect to the channel's flow axis is about 2º. The separation of the apertures in the direction perpendicular to the flow axis of the microfluidic channel is 330 nm (smaller than half of the aperture focal plane resolution) in order to satisfy the Nyquist criteria to prevent the sampling problem of aliasing. The OFM aperture array is located in the middle segment of the main microfluidic channel so that the sample can flow across this rotation-free region steadily and free from entrance effect, under the regime of low Reynolds number flow. The side microfluidic channel is designed three times wider than the main microfluidic channel in order to create an accelerating flow before biological samples enter the main channel for imaging. This microfluidic design reduces the chance of cell stiction in the main microfluidic channel during prolonged usage of the OFM device. The cross-sectional view of the OFM device is shown in Figure 3.1.2(b).
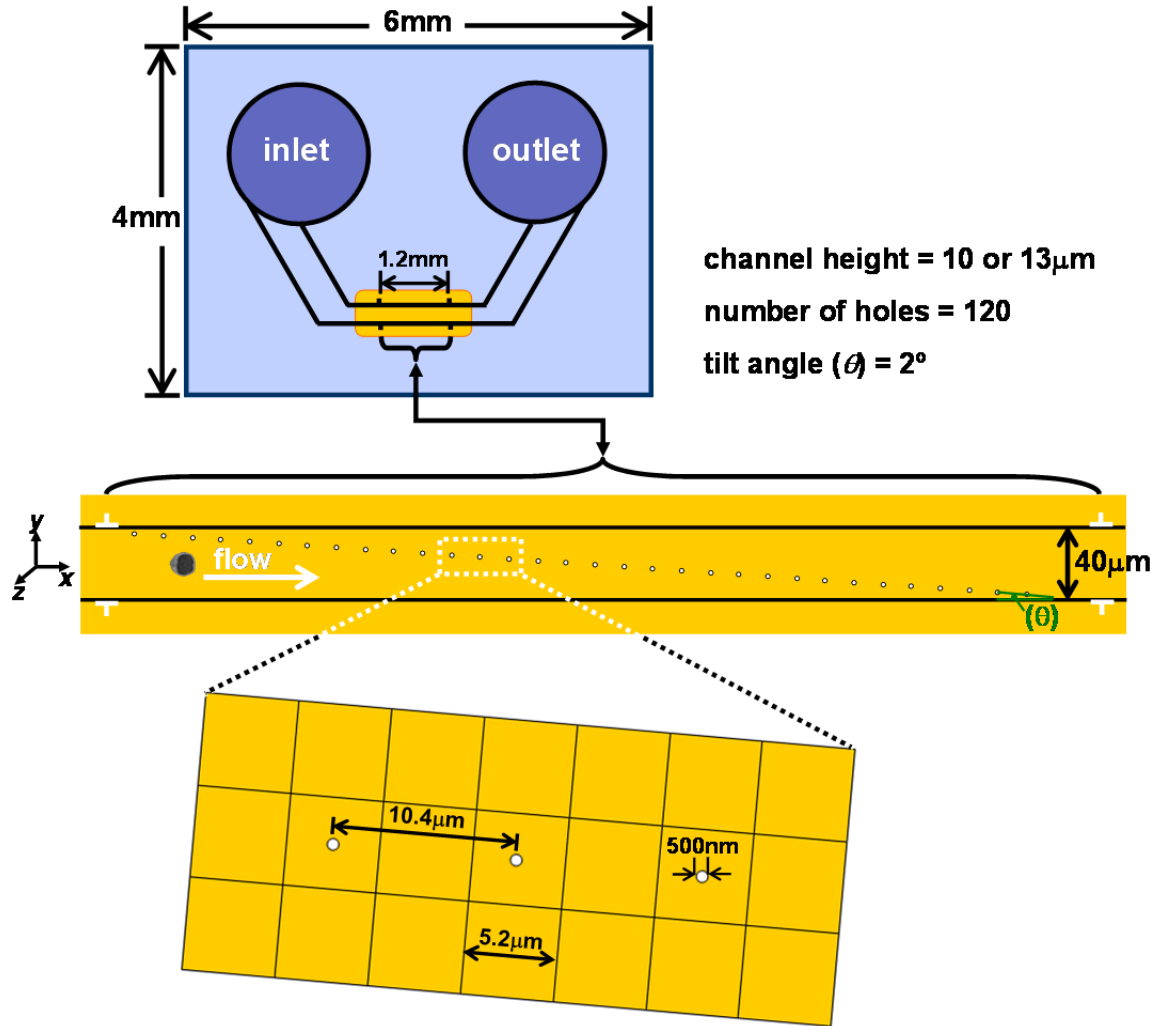
(a)
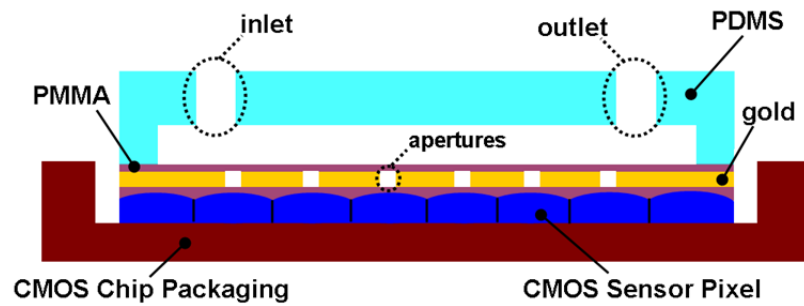
(b)
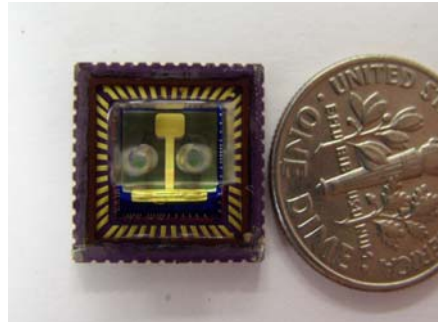
(c)

Figure 3.1.2 An illustration of design and fabrication of the on-chip collection-aperture device: (a) The

planar geometry and the aperture array arrangement of the on-chip OFM, (b) The cross-sectional scheme

of the OFM device, (c) A photo of the fabricated on-chip OFM device.

A combination of nanofabrication technology and standard softlithography technique is used to

fabricate the on-chip collection-aperture-based OFM devices. I used a monochrome CMOS imaging

sensor (Aptina, MT9M001C12STM) as the starting substrate. This sensor chip contains a 2D array of

1280×1024 square pixels. Please note that the fabricated OFM device will only use a couple of lines of

pixels on this sensor chip for sensing and, as such, I could have used a linear array sensor chip in place of

this particular chip model. First, the cover glass of the CMOS sensor chip is removed and the surface of

the imaging sensor pixel is washed with IPA. The sensor chip is spin coated with a 400 nm layer of

PMMA for planarization using a standard spin coater (WS-400A-6NPP/LITE, Laurell Technologies).

Notice that the micro-lens array on top of each pixel is not removed for the purpose of precise positioning

in aperture fabrication in the FIB process afterwards. In fact, the thickness of the first PMMA layer has

been optimized to partially planarize the sensor pixel, so that it can effectively protect the imaging sensor

pixel underneath but at the same time it does not completely planarize the pixel. Next, I coated a 15 nm

chromium seed layer followed by a 300-nm-thick gold layer onto the PMMA surface by thermal evaporation (AVC 1000, Veeco). After the metal coating, the CMOS sensor pixels maintain a certain degree of topology for pattern recognition in FIB imaging. Using FIB (Nova200, dual beam FEI Company), a line array of circular apertures is milled into the metal layer. The Ga^+ ion beam has a 5 nm nominal diameter with the voltage set to be 30 kV and ion current to be 0.30 mA. I then passivated the gold surface with another 400-nm-thick PMMA layer. This PMMA layer both protects the collection-apertures and prevents electrolysis of the metal layer when the electric field is applied. The choice of layer thickness represents a compromise between passivation robustness and the need to optimize object and collection aperture array proximity for good image resolution. After coating of the second PMMA layer, the CMOS pixels are almost completely planarized, and this layer forms the floor of the microfluidic channel. Next a transparent PDMS block containing a microfluidic channel is placed onto the modified sensor chip. The PDMS microfluidic channel is formed by standard softlithography, which defines its planar geometry, and the microfluidic channel height, which is designed by a SU-8 patterning process. The placement is performed with the aid of a contact aligner (Karl Suss, MJB3) to ensure a precise alignment of the angle between the microfluidic channel and the direction of the aperture array. A photo of the fabricated on-chip OFM device is shown in Figure 3.1.2(c). Finally, I mounted the OFM device onto a customized socket, which is connected to an evaluation board (Silicon Video® 9M001 from Epix, Inc.), which allows interface between the OFM device and a desktop computer.

3.1.3 Demonstration in Bright Field OFM Imaging without Focusing Ability

For testing and evaluations, the on-chip collection-aperture OFM device is mounted on a conventional optical microscope (BX41, Olympus Microscopy) and illuminated under a white light source (100 W halogen lamp through a 5× objective with NA = 0.10, focal plane resolution = 2.5 μm) from the top. The light reaching the biological sample is approximately uniform. The incident light intensity is 20 mW·cm^{-2}, which is comparable to the intensity of sunlight. The conventional microscope used in the experiment simply serves as a platform for cross-verifications and is not an integral part of the OFM device. I reprogramed the associated data-readout software so that we can readout the relevant lines of the sensor pixels rather than the entire sensor grid. This way we are able to achieve a line readout rate of 2000 lines per second. An exposure time of 0.5 ms is selected in each readout. During the image acquisition process, the control of flow speed is critical to prevent undersampling artifacts in the OFM images. The flow speed of each target is calculated by dividing the channel length spanned by the aperture array by the transit time of the object across the entire array. The percentage error of the computed flow speed is found to be less than 4% for most of the biological samples I examined. Since the OFM device collects signal from each relevant sensor pixel at a rate of 2000 per second (the maximum line rate for this sensor), this frame rate corresponds to a threshold object flow of 1 mm/s before undersampling problem to occur. During my experiments, I typically operate with flow speeds that are substantially lower than this speed to preserve good resolution in the flow direction. The sample solution is introduced into the OFM device by injecting the solution into the input port using a syringe. The solution automatically fills the entire microfluidic channel by capillary force. There are two ways by which we can actuate microfluidic flow and perform sample scanning, depending on the biological samples — pressure-based flow and electrokinetic-based translation. I have described the implementation of both approaches in Chapter 2. The biological sample preparations and microfluidic channel surface modification are explained in Appendix A. An

experimental schematic is shown in Figure 3.1.3.1. The biological sample flow in the microfluidic channel is monitored under computer 1 and the OFM device is connected to computer 2 for imaging acquisition. When the biological sample is about to enter the OFM imaging area, the capture card will be triggered to start recording the image frames. In experiments with DC electrokinetics, the microfluidic channel is usually connected to a multi-meter for current monitoring.

The maximum throughput of the sample in test is about 20 cells per minute. We observed that the OFM device can typically operate for about 30 minutes before debris accumulation begins to have an impact on the uniformity of the flow velocity. This relatively long operational lifetime is attributable to the PEG coating treatment of the microfluidic channel, which reduces debris deposition. The microfluidic channel can be flushed and rinsed with DI water via a vacuum pump. The on-chip OFM can then be stored under DI water, ready for repeated use.
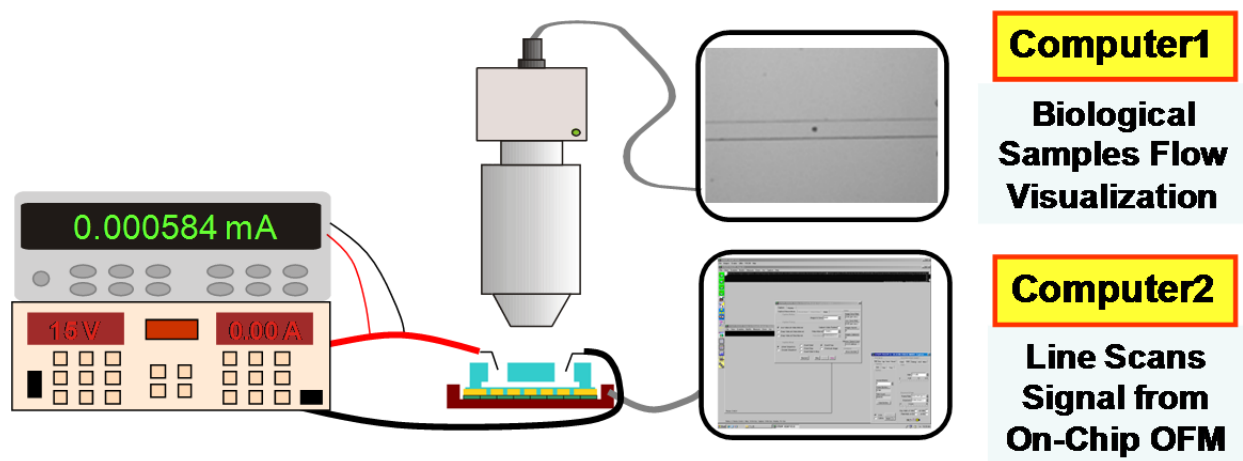
Figure 3.1.3.1 An illustration of the experiment setup to evaluate the performance of on-chip OFM device using DC electrokinetics to drive the flow of biological samples

Several OFM images of three different samples (namely, *Chlamydomonas*, mulberry pollen, and 10 μm polystyrene microspheres), are shown respectively in Figure 3.1.3.2(a)–(e) in comparison with images acquired with an inverted microscope (Olympus IX-71) under a 20× microscope objective in Figure 3.1.3.2(f)–(j). We also imaged a number of *G. lamblia* cysts and trophozoites with our compact collection-aperture OFM device. Figure 3.1.3.3(a)–(d) and (g)–(j) are OFM images (NA = 0.4, focal plane resolution = 800 nm) of several *G. lamblia* cysts and trophozoites respectively. Figure 3.1.3.3(e) and Figure 3.1.3.3(k) are conventional optical microscopy images of similar *G. lamblia* cysts and trophozoites acquired with an inverted light transmission microscope (Olympus IX-71) under a 40× objective (NA = 0.65, focal plane resolution = 420 nm). We can see that the OFM images compare well with standard microscopy images. The subcellular content and the trophozoites's flagella are clearly discernable in the OFM images.

I further compare the performance of our OFM device to the simple direct projection imaging scheme. In this experiment, we placed some *G. lamblia* cysts and trophozoites directly onto a high density CMOS sensor chip (Micron Tech, MT9P001) and allowed the specimens to settle on the pixel surface. With a sensor pixel size of 2.2 μm, this is the highest pixel density sensor chip that is currently commercially available at that time. Representative images of the targets are shown in Figure 3.1.3.3(f) and (l). The relatively low quality of the images when compared with OFM images can be attributed to a number of reasons. First, due to the planar design of the CMOS sensor chip and the fact that each sensor pixel fill factor is normally less than unity, we expect these images to be sparsely sampled. In comparison, the OFM method actually allows us to oversample our targets by simply choosing a slower flow speed than the sensor frame rate and by ensuring that the line scans associated with the apertures overlap spatially. The latter can be accomplished by choosing a shallow tilt angle for the aperture array versus the microfluidic channel. Second, the transparent protective coating on the sensor deteriorates the achievable resolution. We estimated that this layer is about 400 nm thick based on typical manufacturing practices.

As the highest resolution is achieved in direct projection imaging by placing the targets as close to the sensor pixels as possible, this relatively thick coating deteriorates the achievable resolution quite significantly [5]. The purpose of this passivation layer is to prevent dielectric breakdown when DC electric field is applied. This passivation layer can be omitted when we are using pressure difference or AC electrokinetics to drive and control the biological sample flow. Some efforts have been made to use other materials for passivation, for example, the incorporation of spin-on-glass coating. However, the application protocol of this passivation coating is found to be incompatible with OFM fabrication due to the high-temperature curing process.
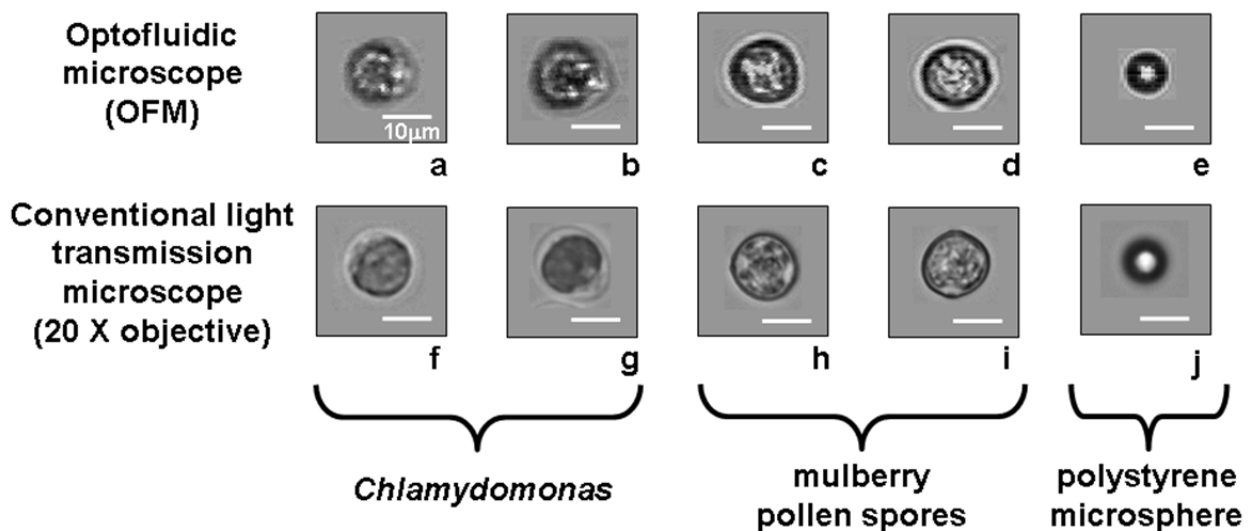
Figure 3.1.3.2 An experimental demonstration of several cell and microsphere images. (a)–(e) Images acquired from the on-chip OFM driven by DC electrokinetics of *Chlamydomonas* (a) and (b), mulberry pollen spores (c) and (d), and a 10 µm polystyrene microsphere (e). (f)–(j) Images acquired from a conventional light transmission microscope under a 20 × objective of *Chlamydomonas* (f) and (g), mulberry pollen spores (h) and (i), and a 10 µm polystyrene microsphere (j)

(Scale bars: 10 µm.)
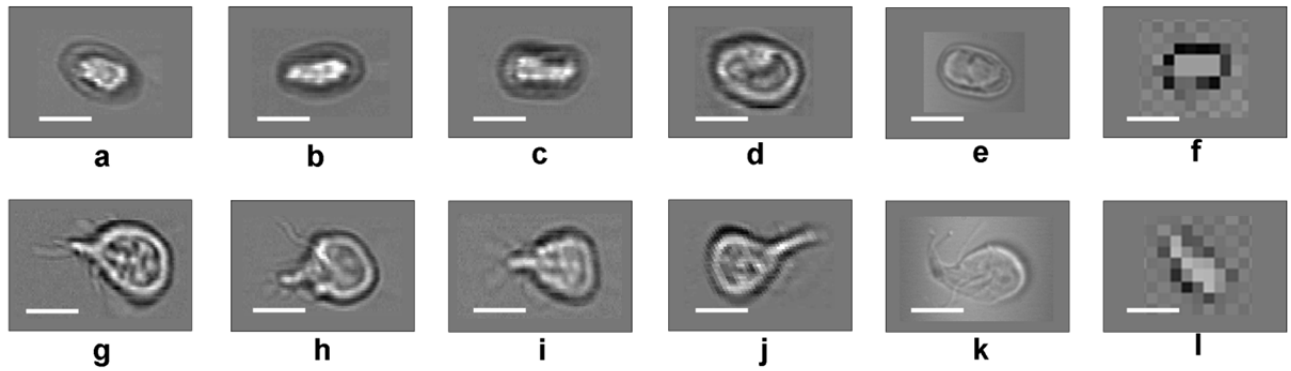
Figure 3.1.3.3 An experimental demonstration of several *G. lamblia* cysts and trophozoites images. (a)–(f) Images acquired from the on-chip OFM device of cysts (a)–(d) and trophozoites (g)–(j). Images taken from a conventional light transmission inverted microscope with a 40× objective of cysts (e) and trophozoites (k). Direct projection images on a 2.2 µm CMOS imaging sensor chip of cyst (f) and trophozoite (l) for comparison

(Scale bars: 10 µm)

3.1.3.1 Optical Resolution, Acceptance Angle and Image Contrast

The optical resolution characterization of a single-layer aperture-based OFM system is studied extensively in references [5, 6]. A NSOM tip less than 100 nm, which can be approximated as a point source, is scanned across the apertures at different heights from the surface of the aperture. The signal response is detected by the underlying sensor pixel. By this, we can extract the point spread function (PSF) of the OFM collection-aperture at different heights. The PSF is broadened as a function of increasing height from the sensor pixel and the diameter of the aperture. Note that the best resolution of my collection-aperture OFM system was 800 nm (with the 400-nm-thick PMMA coating above the metal layer accounted for) and the resolution degraded to 2 µm at a height separation of 2.5 µm. The result of the NSOM study reveals that the collection-aperture OFM device achieves its highest resolution in the plane that is just above the aperture array. Thus, the single-layer OFM system is similar to a conventional microscope, in which the focal plane is locked at the plane that is just below the sample object. Another study is conducted to characterize the acceptance angles of small circular apertures [7]. By examining the full width at half maximum (FWHM) of the acceptance angle as a function of the aperture size, we show that the acceptance angle of a circular aperture reaches a minimum of 67° before rebounding around the transition between single-mode and multimode transmission (approximately 400 nm). This study is important because it characterizes the depth of focus of OFM collection apertures.

The OFM image contrast mechanism shares some similarities with the contrast in conventional microscopy images. In bright field imaging, the light field at the detection plane is a superposition of both the unscattered illumination light and light from scatterers in the biological sample. This effect is best illustrated with the pollen spore OFM images shown in Figure 3.1.3.2(c),(d). The dark boundary at the border of the pollen spores is due to the decrease in light intensity resulting from the presence of the

pollen cell wall, which scatters light away. The bright ring next to that dark boundary is due to the increased intensity of light diffracted from the cell wall of the pollen spore. The above observation is based on the assumption that the near-field light component is not significant. We find this assumption is valid, since the smallest collection aperture we used in OFM imaging is 500 nm and the closest sample distance from the aperture is 400 nm. Assuming an average illumination wavelength of 500 nm, the Fresnel number is closed to unity. In this regime, the near-field effect is not important. We also note that it is possible to achieve better resolution in OFM imaging by using smaller apertures with sub-wavelength size. However, there are two intrinsic difficulties to achieving sub-wavelength resolution imaging in collection-mode OFM systems. First, when the aperture size becomes smaller than the wavelength of the illumination light, the light transmission is very weak. In this regime, the light transmission scales to the power of fourth with the aperture diameter; this implies we may need to use a very strong illumination light. Using high power illumination can cause evaporation and bubble generation in the microfluidic channel, which is not desirable for biological sample translation. Second and more importantly, since we are using microfluidic flow for biological sample transition in the OFM imaging method, the sample motion is unavoidably affected by Brownian motion. The motion fluctuation will introduce image blur or distortion in the final OFM image formation.

It is worth noting that, similar to a conventional transmission microscope, in principle there is no upper limit to the sample thickness that the OFM device can process. However, in practice the OFM will fail to acquire an image if the biological sample is too optically scattering or absorptive to permit sufficient light to transmit through the collection OFM apertures. We believe this problem can be solved if we are allowed to incorporate a tightly focused light spot for illumination.

3.2   Two-Layers Structure

In the first part of this chapter, we studied and discussed the characteristics of single-layer structure collection-based OFM systems and we successfully demonstrated high-quality bright field imaging with submicron sized circular apertures fabricated at the bottom of the microfluidic channel to collect light from the target samples for image formation. From an optics point of view, although this imaging scheme can overcome optical resolution by physically limiting the size of a CMOS imaging sensor pixel, it is still based on shadow imaging, in which illumination light from the top along the propagation direction passes through every part of the biological sample before being collected by the OFM aperture for detection. In essence, we are still imaging the light projection of the biological sample, regardless of the fact that the slanted OFM aperture array improved both the optical resolution and the sampling density of the shadow images. This imaging scheme actually implies several limitations. First, the spatial resolution of the image decays approximately linearly if the biological samples are translating further away from the channel bottom, due to the broadening PSF [6]. To ensure distortion-free and good-resolution imaging, we have to make sure that the biological samples are flowing constantly without tumbling and rotation in close proximity to the channel bottom. One way to achieve this is to build a microfluidic channel with height comparable to the size of the flowing objects, in order to geometrically confine the biological samples into flowing in close proximity to the channel bottom. However, the throughput rate can be significantly hindered due to the frictional interaction between the biological samples and the channel surface. Channel blockage can easily occur due to the same reason. In addition, most biological species have a distribution in size and shape, for example, normal human red blood cells (RBCs) have standard size of about 6–8 μm. It is very difficult to accommodate all cells of different shapes and sizes in a single microfluidic channel and make sure all of them are rendered with good optical resolution in a single-layer collection-aperture-based OFM system. This problem becomes more severe if we want to image different biological species in a mixture of cell suspension. It is possible to use advanced microfluidic technology or the

incorporation of other external forces—for example, optical or electric force [8, 9]—to manipulate the biological samples to orientate and translate in close proximity to the collection apertures at the channel bottom. Unavoidably, however, this will cause our OFM prototypes to become more complicated and nullify the advantage of an OFM system being a simple and compact device. Second, in collection-aperture-based OFM systems, since the highest resolution plane is locked just above the aperture array at the channel bottom, we are not allowed to set the focal plane location to different planes of the biological samples. If we are imaging thick or optically highly scattering or absorptive biological samples, there is not enough light to be collected by OFM apertures, causing deterioration of image contrast. These limitations on the first prototype of OFM systems motivated me to rethink and improve the imaging scheme. I started to think about expanding the design from single-layer to two-layer structures. This way we will be able to optically relay the focal plane at the collection apertures sitting immediately on top of the imaging sensor pixel to a different depth in the microfluidic channel by the proper design of optical elements at the second layer. The two-layer structure actually enables another degree of freedom for optical arrangement. We showed that, by tilting the angle of illumination light, it is possible to achieve dark field imaging in an OFM context. The incorporation of relay optics in OFM imaging allows us to collect light locally at a desired position, for example, at the mid-plane of the microfluidic channel. In this case, we no longer require the biological samples to flow in proximity to the channel bottom to ensure good image resolution. Thus, we can employ a much simpler microfluidic control configuration—for example, a well-developed three-dimensional hydrodynamic focusing unit—to force the flow of biological samples along the channel mid-axis, where the velocity profile has zero or minimal vorticity. The rotational motion of biological samples is reduced to minimum, regardless of the shape and orientation. We can also build a taller microfluidic channel to accommodate biological samples with different sizes and shapes. This allows us to image a mixture of different biological species in a single microfluidic channel with good image resolution and quality. The chance of channel clogging is reduced, due to the absence of flowing-object and channel-surface interaction. In fact, the implementation of relay optics shares a certain similarity with the role of a pinhole aperture in confocal microscopy. The pinhole

aperture in confocal microscopes is usually placed in front of a photodetector to reject out-of-focus light and collect only in-focus light by relay optics. This enables sectioning capability in confocal microscopy. Modern laser scanning confocal microscopes use very sophisticated mechanical actuation mechanisms (for example, a Galvo mirror or even an MEMS scanning mirror/lens [10]) to direct a tightly focused light spot at different locations on the specimen and then relay the light spots by collection optics to the photodetector pixel. The OFM imaging method instead uses a simple microfluidic flow to deliver biological samples across an array of collection focal spots for optical scanning. This highly simplifies the optical scanning mechanism. One remark here is that a complete confocal OFM system requires an effort to integrate both illumination and collection optical units with the microfluidic channel. In this chapter, we limit our discussion and experimental findings to collection-mode OFM systems only. The details and challenges of implementing a miniaturized version of a confocal OFM prototype will be discussed in Chapter 5.

3.2.1 Using a Fresnel Zone Plate as a Light Collection Unit in OFM Imaging

The optical collection unit of an on-chip OFM device is composed of two parts: a pinhole aperture fabricated directly on top of the CMOS imaging sensor and a focusing unit to relay the point of interest to the aperture. Usually light focusing is through an optical convex lens which transmits and refracts light, converging the light beam to a focal point. However, micromachining of the lenslet or micro-mirror array [11, 12] usually requires a well-controlled thermal annealing or micro-molding process to prevent aberration and ensure good focusing property. The fabrication process of a lenslet or micro-mirror array is not very compatible with the building of OFM devices. I started to look for alternatives. Unlike other optical lenses, FZP focuses light by diffraction instead of refraction. Amplitude-modulated FZP is composed of a set of concentric rings with increasing line densities, known as Fresnel zones, which alternate between opaque and transparent. When a monochromatic light hits the zone plate, it will diffract around the opaque zones. The zones are designed and spaced such that the diffracted light constructively interferes at the focus, creating a light spot. In the other words, we can regard the FZP as a circular grating. Similar to any other kind of grating, the FZP has multiple diffraction orders, resulting in multiple foci. The fabrication process of amplitude-modulated FZP is more compatible with standard micro/nanofabrication technique, due to its planar nature.

The working principle of the FZP-aperture-collection unit in the compact OFM system is very straight forward. It consists of a pinhole, fabricated directly on top of the middle of a CMOS imaging sensor pixel as illustrated in Figure 3.2.1.1(a), (b). An FZP is then fabricated on top of a spacing layer and acts as an optical lens to relay light from the point of interest on the target object to the collection aperture. The purpose of a transparent spacing layer is to provide room for light propagation. The thickness of this spacing layer determines the magnification of the object and plays an important role in

the design parameter of the FZP. Note that FZP is a diffraction-based optical element. To avoid significant chromatic aberration, the illumination light should be monochromatic, for example, a laser source. Figure 3.2.1.1(c) is a schematic illustrating the working principle of a collection-FZP-aperture unit. The pinhole aperture accepts only light in focus (solid line) collected by the FZP, and rejects light out of focus (dotted line). This configuration results in the increase of spatial resolution both in the lateral direction (x,y) and axial direction (z). The combination of the aperture and FZP effectively forms a pair of conjugate focal spots between the point of interest in the object plane and the collection aperture.
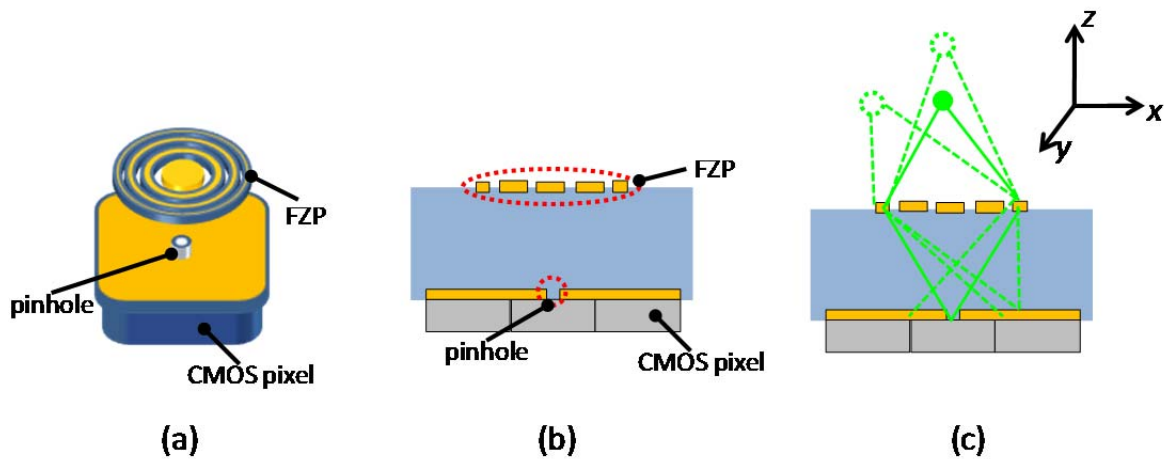
Figure 3.2.1.1 An illustration of collection-FZP-aperture unit: (a) from a perspective view, (b) from a side view, (c) for the working principle

Here I am going to briefly explain the construction and certain characteristics of FZP. We start with the simplest configuration, where we want to focus a monochromatic plane wave to a focal spot. As shown in Figure 3.2.1.2, to design and construct an amplitude-modulated FZP, the basic idea is to introduce a path difference of one λ between successive zones (open areas) so that the light transmission through the zones will have a constructive interference at the desired focus spot. If one draws a right triangle with the focal length f as one side and the radius of any zone r_m as a second side, the hypotenuse should have the length of $f + m\lambda/2$. The zonal radius can be found by the following relation:

$$r_m = \sqrt{m\lambda f + \left(\frac{m\lambda}{2}\right)^2}$$. $$(3\text{-}1)$$

The numerical aperture (NA) of a conventional microscope objective lens, assuming the propagation medium is air, in which the refractive index is equal to 1.0, is defined as:

$$NA = \sin\theta \qquad (3\text{-}2)$$

where θ is the half angle of the largest cone of light that can be collected by the microscope objective lens.
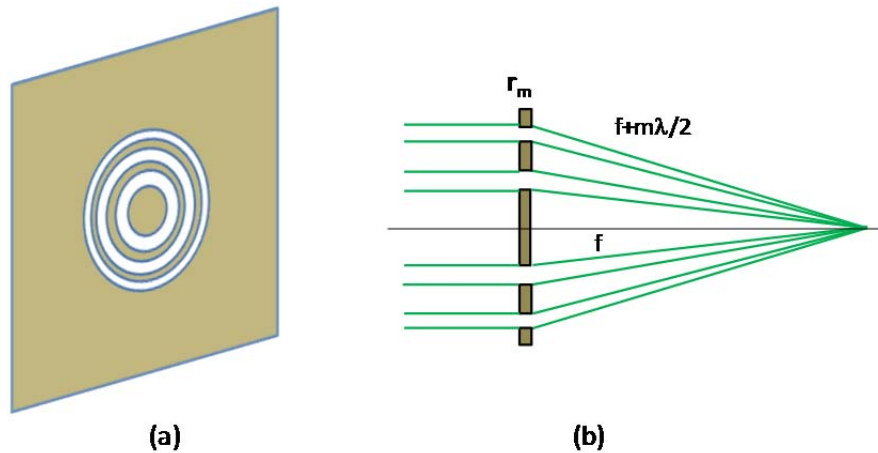
Figure 3.2.1.2 An illustration of the FZP under a collimated laser illumination: (a) from perspective view, (b) for the working principle

Under Rayleigh's criterion, $R_{Rayleigh}$ denotes the resolution limit of such lens-based imaging systems.

$$R_{Rayleigh} = 0.61\frac{\lambda}{NA} \qquad (3\text{-}3)$$

By paraxial assumption, and if the total number of zones is sufficiently large, the optical resolution of FZP can be roughly approximated by:

$$R_{Rayleigh} = 1.22\Delta r \quad .$$
(3-4)

Thus, the optical resolution of the FZP is principally determined by the width of the outermost ring, Δr. Another important parameter that characterizes the degree of convergence of an optical lens or an imaging system is the depth of focus. One way to characterize depth of focus is by Gaussian beam approximation, which has been largely adopted by the optics and laser community [13]. The depth of focus, z_R, in Gaussian beam is defined as the distance travelled by a light beam along the propagation direction from the beam waist to the location where the area of the cross section is doubled (or the beam radius is increased by a factor of $\sqrt{2}$):

$$z_R = \frac{\pi\omega_0^2}{\lambda}$$
(3-5)

where λ is the wavelength and ω_0 is the beam waist, the radius at its narrowest point. We find that the application of FZP is mainly within the soft X-rays and extreme ultraviolet radiation domain and not extensively used in optical microscopes or other imaging devices in the visible spectrum [14]. Only recently have researchers started to realize the potential of using FZPs [15-17] in optofluidic imaging or sensing devices.

One major reason why FZP is not widely used in full-field imaging in optical microscopy is that FZP suffers from serious aberrations beyond the paraxial region [18, 19]. FZP also has multiple higher-order diffraction focusing along the propagating axial direction, although the intensity of these higher-order diffractions is sufficiently less than the first-order diffraction (at least ten times weaker [14]).

Nevertheless, in our collection-FZP-aperture unit, the arrangement of the pinhole aperture can effectively block higher diffractions and off-axis aberration and collects light from the focal point under normal or tilted illumination.

In amplitude FZP, 50% of the incident light is blocked by the opaque zones and 25% of the light transmits to the forward direction and only 10% goes to the first order focus. The efficiency can be improved to 40% by replacing the opaque rings with transparent rings of a thickness to introduce a phase change of π. This is the so-called phase-reversal zone plate [20]. However, the fabrication of phase-modulated FZP involves a much more sophisticated fabrication process. One possible approach is by nano-imprinting [21]. The precise tolerance control of the thickness is critical for the diffraction efficiency. Nonetheless, the incorporation of phase FZP is very appealing to fluorescence OFM application in which photon budget is critical for light collection.

3.2.2 Design and Fabrication Process

Here we have a basic understanding of the working principle and diffraction properties of FZP. Next, we are going to work on the details in the design parameters of the FZP and aperture. The collection aperture size is selected to be 1 μm. In principle, we can possibly obtain a better contrast and spatial resolution (both vertical and horizontal) if we choose a smaller size aperture. However, the amount of light we collect will be significantly reduced. More importantly, it also requires a higher degree of precise alignment between the FZP and collection aperture, which is difficult to achieve in our current fabrication approach. Thus, an aperture size of 1 μm is a result of the compromise of these two factors.

In the preceding sections we have considered the focusing conditions for a FZP from a uniform plane wave illumination. However, in designing the collection-FZP-aperture unit, we used the FZP to relay a point source from the object plane to the aperture. We should consider a point object at a finite distance q from the zone plate, to an image plane at a distance p, as illustrated in Figure 3.2.2.1. Since we are building the FZP-aperture on the chip-level, we need to take into account the difference in the refractive index for the materials we used in the device construction. The object distance is given by:

$$q = q_{water} + q_{PMMA} \tag{3-6}$$

and image distance is given by:

$$p = p_{SU-8} \quad . \tag{3-7}$$

The zonal radius $r_{m,[collection]}$ is expressed as the follows:

$$r_{m,[collection]} = r_{m,water} + r_{m,PMMA} \tag{3-8}$$

$$\frac{r_{m,water}}{q_{water}} = \tan\theta_{water} \approx \sin\theta_{water} \quad \text{and} \quad \frac{r_{m,PMMA}}{q_{PMMA}} = \tan\theta_{PMMA} \approx \sin\theta_{PMMA}. \tag{3-9}$$

Here we made an assumption for small angle refraction or para-axial approximation, i.e., $\tan\theta \cong \sin\theta$. By Snell's law, the refraction angle and refractive index are related as:

$$\mu_{water}\sin\theta_{water} = \mu_{PMMA}\sin\theta_{PMMA} \tag{3-10}$$

$$r_{m,[collection]} = r_{m,water}\left[1+\left(\frac{\mu_{water}}{\mu_{PMMA}}\right)\left(\frac{q_{m,PMMA}}{q_{m,water}}\right)\right] \quad \text{where} \quad q_{m,water} = \sqrt{q_{water}^2 + r_{m,water}^2} \tag{3-11}$$

$$r_{m,[collection]} = r_{m,PMMA}\left[1+\left(\frac{\mu_{PMMA}}{\mu_{water}}\right)\left(\frac{q_{m,water}}{q_{m,PMMA}}\right)\right] \quad \text{where} \quad q_{m,PMMA} = \sqrt{q_{PMMA}^2 + r_{m,PMMA}^2} \tag{3-12}$$

Rearranging the algebraic terms gives:

$$p_{m,SU-8} = \sqrt{p_{SU-8}^2 + r_{m,[collection]}^2} \tag{3-13}$$

$$q_{m,PMMA} = \sqrt{q_{PMMA}^2 + \left[\frac{r_{m,[collection]}}{1+(\frac{q_{water}}{q_{PMMA}})(\frac{\mu_{PMMA}}{\mu_{water}})}\right]^2} \quad q_{m,water} = \sqrt{q_{water}^2 + \left[\frac{r_{m,[collection]}}{1+(\frac{q_{PMMA}}{q_{water}})(\frac{\mu_{water}}{\mu_{PMMA}})}\right]^2}.$$

$$\tag{3-14}$$

The same design rule as in collimated laser illumination is applied to construct the successive zones of the collection-FZP unit: alternately transparent and opaque, so as to add half of the wavelength, $\lambda/2\mu_{mean}$, to successive path lengths. It gives:

$$q_{m,water} + q_{m,PMMA} + p_{m,SU-8} = q_{water} + q_{PMMA} + p_{SU-8} + \frac{m\lambda}{2\mu_{mean}} \qquad (3\text{-}15)$$

where the mean refractive index, μ_{mean} is given by:

$$\mu_{mean} = \frac{q_{water}\,\mu_{water} + q_{PMMA}\,\mu_{PMMA} + p_{SU-8}\mu_{SU-8}}{q_{water} + q_{PMMA} + p_{SU-8}} \qquad . \qquad (3\text{-}16)$$

The terms from Equations (3-6), (3-7), (3-13), (3-14), and (3-16) are substituted into Equation (3-15). Equation (3-15) cannot be solved analytically to obtain a closed-form solution. The zonal radius of the collection-FZP unit is determined numerically by a trial-and-error approach. We chose the following parameters for the construction of the collection-FZP unit:

The object and image distances are $q_{water} = 5$ μm, $q_{PMMA} = 5$ μm, $p_{SU-8} = 25$ μm.

The magnification is $M = q/p = 2.5$.

The refractive index of water, PMMA, and SU-8 are 1.33, 1.49, and 1.65, respectively.

The zonal radius of the collection-FZP unit is listed in Table 3.2.2.
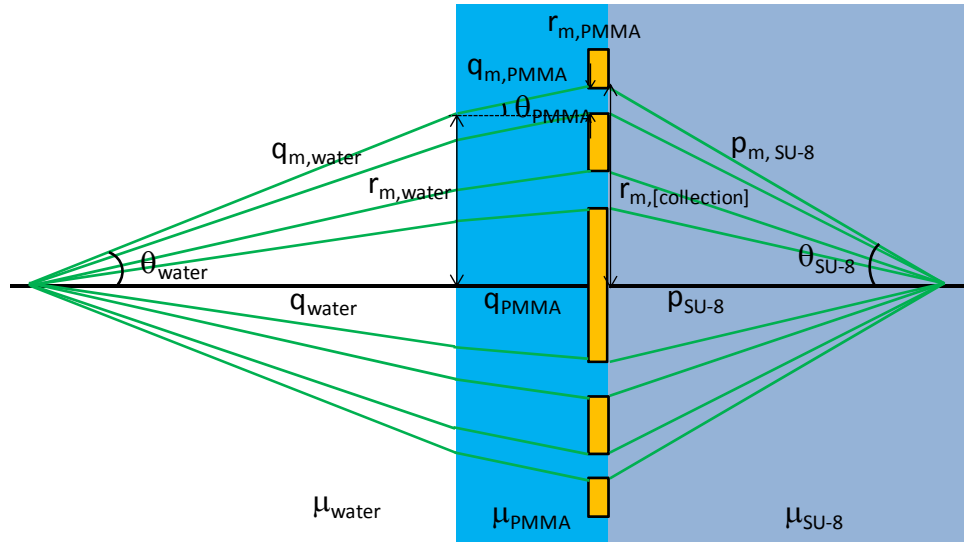
Figure 3.2.2.1 An illustration in design of the zonal radius of the collection FZP

q_water=5	m	r	width
q_PMMA=5	1	1.66	0.69
p_SU-8=25	2	2.35	0.54
	3	2.89	0.45
mu=1.51	4	3.34	0.4
lambda=0.532	5	3.74	0.37
h=20	6	4.11	0.34
	7	4.45	0.32
	8	4.77	0.3
	9	5.07	0.28
	10	5.35	0.27
	11	5.62	0.26
	12	5.88	
	13		

q_water=10	m	r	width
q_PMMA=5	1	1.87	0.79
p_SU-8=25	2	2.66	0.6
	3	3.26	0.51
mu=1.51	4	3.77	0.45
lambda=0.532	5	4.22	0.41
h=20	6	4.63	0.38
	7	5.01	0.35
	8	5.36	0.33
	9	5.69	0.32
	10	6.01	0.3
	11	6.31	0.29
	12	6.6	0.27
	13	6.87	0.27
	14	7.14	0.26
	15	7.4	

Table 3.2.2 A summary of two sets of the zonal radius design in collection FZP

I have described the detailed formulation of the design parameters of FZP. The next step is determining how to implement such design in on-chip OFM systems. FZP can be cost-effectively fabricated with micro- or nanofabrication techniques such as standard optical or electron-beam lithography. However, in our implementation, we cannot use standard optical lithography since the size of the zone is on a submicron level and the typical resolution of standard optical lithography is about 2 μm. Electron-beam lithography is another option. However, the secondary electrons generated in the electron-beam process can deteriorate the performance of the CMOS imaging sensor since we are conducting the fabrication on-chip. Thus, we chose to use FIB for the fabrication of the pinhole and FZP layers.

The cross section of the collection-FZP-aperture OFM device is shown in Figure 3.2.2.2. The starting substrate is a 2-D CMOS imaging sensor array (Aptina, MT9M001C12STM). The first half of the fabrication process is very similar to that of the single layer collection aperture OFM device as described in Section 3.1.2. After partial planarization of a thin layer of PMMA, the sensor chip is then coated with a thin gold layer. The CMOS sensor chip is sent to the FIB to mill two lines of 160 circular aperture arrays—1 μm in diameter with a separation of 15.6 μm, which is equivalent to 3 pixels—at the center of the imaging sensor pixel. This separation is chosen to prevent the overlapping of successive FZP units in the metal layer afterwards. These two-line arrays of collection apertures have a lateral shift of 5.2 μm, equivalent to the pitch size of one CMOS sensor pixel. A set of alignment marks is patterned on the first gold layer to allow sequential alignment for the FZP layer. Then, a layer of SU-8 with a thickness 25 μm is spin coated on the aperture gold layer, forming the relay spacing layer. This SU-8 layer is then patterned with a window opening to expose the alignment patterns on the first gold layer. A second gold layer of thickness of 200 nm is then deposited on the SU-8 layer using thermal evaporation. The substrate is placed in the FIB machine again to fabricate two-line arrays of FZP units on the second gold layer. In the FIB imaging mode, we can still discern the alignment mark on the first collection aperture metal layer clearly in the open window, allowing us to align the FZP units precisely with the collection aperture

underneath. The tolerance of misalignment is estimated to be around 1 μm for every 20 FZP units. An illustration of the collection-FZP units by SEM and FIB imaging is shown in Figure 3.2.2.3. Two lines of FZP arrays are fabricated, with the first line of FZP designed with object distance, q_{water}, of 10 μm and the second line with distance 5 μm, measured from the FZP plane. These two lines have a lateral shift of 5.2 μm, equivalent to one sensor pixel. The voltage of FIB is set to be 30 kV, but the ion current is increased to 3.0mA. Although we sacrifice the control of roughness on the Au layer, the processing time to mill FZPs is 10 times faster. After the fabrication of the FZP arrays, a layer of 5 μm PMMA is spin coated on the substrate for the protection of the FZP metal layer. A PDMS microfluidic channel with height of 15 μm is aligned under the contact aligner and bonded with the PMMA coating temporarily so that the PDMS microfluidic channel can be separated and bonded again for cleaning if channel blockage occurs to enable repeated use. The inclination angle of the microfluidic channel with respect to the direction of the FZP-aperture array is chosen to be 2°. This alignment and bonding process is identical with the single-layer collection-aperture device.
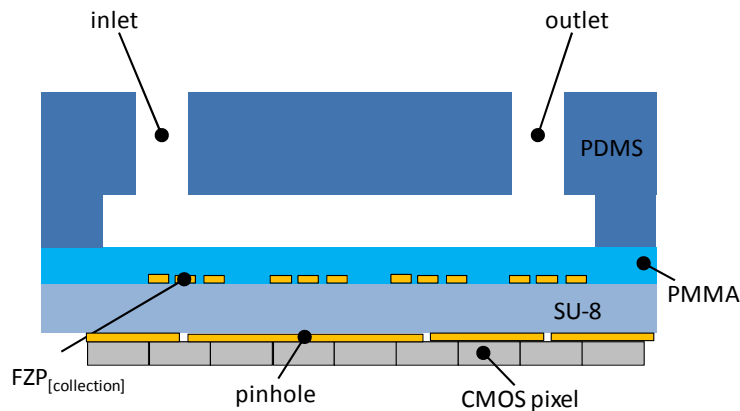
Figure 3.2.2.2 A schematic of the cross section of the collection-mode FZP-aperture OFM device
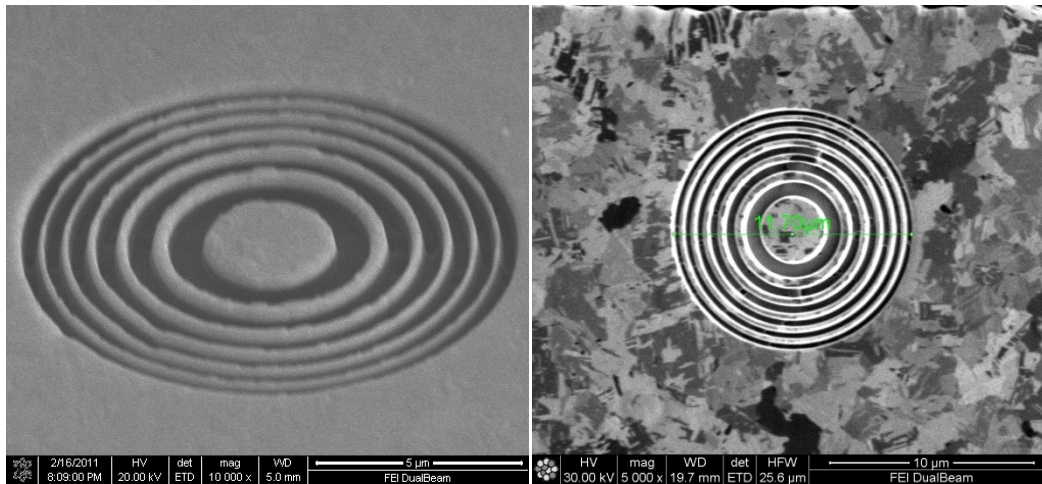
(a)   (b)
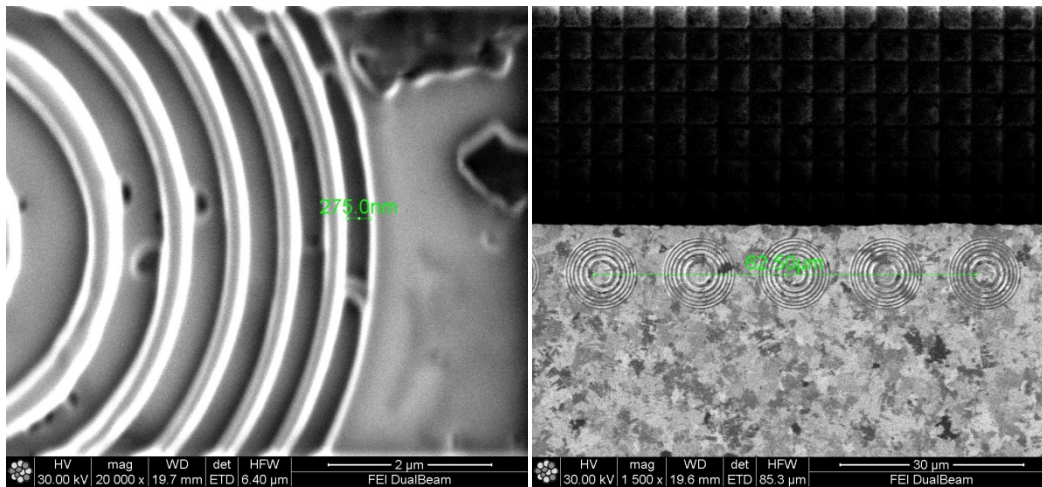
(c)   (d)

Figure 3.2.2.3 An experimental illustration of collection FZP fabrication by FIB nano-machining (a) in high magnification SEM imaging mode, (b) in FIB imaging mode, (c) in high magnification FIB imaging mode, and (d) in low magnification FIB imaging mode to show the alignment of the collection FZP units array

3.2.3 Demonstration in Bright Field FZP-aperture OFM Imaging

I first evaluated the collection-FZP-aperture bright field OFM imaging by using a coherent normal illumination. The on-chip collection-FZP-aperture OFM device was mounted on a platform on the optical table. A laser (Excelsior-532-200-CDRH, Spectra Physics, with wavelength of 532 nm and power of 200 mW) was used as the light source. The laser was attenuated, and expanded to a collimated Gaussian beam with $1/e^2$ beam diameter of 21.3 mm. I used only the center portion of the beam (diameter is 12 mm and has a power of about 1 mW). The illumination light can be regarded as a plane wave. Before the experiment, I adjusted the alignment of the light path so that the pixel response reached its maximum to ensure the illumination was normal to the FZP-aperture pixel array.

I generated the cell flow by pressure and DC electrokinetics in a similar way as with the single-layer collection-aperture OFM system. During the image acquisition process, the average flow speed of the biological samples in the experiment was about 350 μm·s^{-1}. The imaging sensor was operated at a frame rate of 2000 frames per second. The pixel exposure time was set to be 0.4 ms. The pixel spacing (or size) of the OFM images is $\delta x = 0.33$ μm and $\delta y = 0.33$ μm. The acquisition time for the OFM images was typically less than 1 second. We observed that occasionally, upon the application DC electrokinetics, gas bubble generation occurred at the edge of the microfluidic channel. This problem became more severe when gas bubbles were trapped in the microfluidic channel in the 'fill-up' process due to the channel roughness after several photoresist patterning processes. Since I still relied on the previous microfluidic control mechanism, which used the channel height to confine the sample flow at a fixed vertical position in the microfluidic channel, it was expected that some biological samples, especially those with smaller size compared to the channel height, would be randomly dispersed at different heights in the microfluidic channel during the translation. Thus, some of the acquired OFM images are defocused for this reason.

Figure 3.2.3 shows an image collection of pollen spores, 10 μm microspheres, and *Cyanophora paradoxa*, a fresh-water alga with two cyanelles or chloroplasts, acquired from the collection-FZP-aperture OFM device and a conventional light transmission optical microscope using both normal coherent and incoherent illumination. Figure 3.2.3(a), (b) shows images of the pollen spores that are acquired with a microscope (Olympus BX-41) through a 20× objective with focal plane resolution of 650 nm under coherent and incoherent illumination, respectively. Figure 3.2.3(c) is the FZP-aperture OFM image of pollen spores. We also display the images in a similar manner for 10 μm microspheres and *Cyanophora paradoxa* in Figure 3.2.3(d)–(f) and Figure 3.2.3(g)–(i), respectively. All the OFM images are acquired based on the second-line FZP array with $q_{water} = 5$ µm.

We notice that the background of the collection-FZP-aperture OFM images appears to be more similar to the incoherent illumination conventional-microscope image than the coherent illumination conventional-microscope image, despite the fact the FZP-aperture OFM device is actually using a coherent source for illumination. The speckle background in Figure 3.2.3(a), (d), (g) is a result of the interference of stray light components scattered and reflected from various interfaces in the compound microscope objective lenses in the conventional microscope and from the biological sample. We notice the speckle pattern varies spatially but not temporally since the biological samples are static in conventional microscope images. We do not observe such speckle patterns on the background in incoherent illumination in Figure 3.2.3(b), (e), (h). In incoherent illumination, light is composed of a spectrum of visible wavelengths. The interference causes speckle patterns produced by each individual wavelength that has path-length differences. The speckle patterns from each wavelength will average each another out in incoherent illumination. The absence of the speckle background in the FZP-aperture OFM images can be explained by noting that each horizontal line in the acquired images represents a time trace of transmitted light in the array of focused spots. If there is no object appearing in the focused spots, the light transmission collected by the FZP through the collection aperture will remain unchanged in time,

assuming the laser fluctuation is negligible. Thus, the intensity variation observed in the FZP-aperture OFM images along the flow direction is insignificant. Across the flow direction, while the intensity collected by each sensor pixel is normalized with respect to each other in the OFM image, which is originally intended to correct for small variations in the collection pinhole size, FZP-aperture unit collection efficiency and CMOS imaging sensor pixel sensitivity. The impact of speckle background in collection-FZP-aperture OFM imaging is effectively eliminated as well. However, the effect of mutual light interference from multiple scatters within the target sample should still remain in the collection-FZP-aperture OFM images since the entire biological sample is flooded everywhere with the plane wave illumination light. The speckle effect within the target samples will be greatly minimized when we use focused light spots for illumination. This is the major motivation to pursue the implementation of a complete confocal OFM device.

We also observe there is jittering in the bright field FZP-aperture OFM images. This artifact is more apparent for relatively large samples, for example, the pollen spores in Figure 3.2.3(c). We believe the jittering artifact in collection-FZP-aperture OFM images is likely attributed to the optical performance variation in individual collection-FZP-aperture units in the OFM device. The fabrication tolerance of the FZP and collection aperture and the alignment between the FZP and aperture arrays affects the optical property of individual collection FZP-aperture unit. The variation of the optical performance of individual FZP-aperture in a dissembled collection FZP-aperture OFM device is studied experimentally and in numerical simulations in Appendix A.4. We also observed a certain degree of image distortion in the FZP-aperture OFM for small biological samples, like *Cyanophora paradoxa* in Figure 3.2.3(i). The image distortion artifact can be attributed to the sample translational fluctuations due to Brownian motion or the non-uniformity of flow speed due to microfluidic channel roughness. Notice that small objects are more subject to flow fluctuation in a microfluidic channel, as explained in Section 2.2.

normal illumination

Conventional microscope
(20 x objective)

pollen spores
Laser, 532 nm   white (halogen)

microsphere, 10 µm
Laser, 532 nm   white (halogen)

Cyanophora paradoxa
Laser, 532 nm   white (halogen)

(a)   (b)

(d)   (e)

(g)   (h)

FZP-aperture OFM

→ flow

pollen spores
Laser, 532 nm

microsphere, 10 µm
Laser, 532 nm

Cyanophora paradoxa
Laser, 532 nm

(c)

(f)

(i)
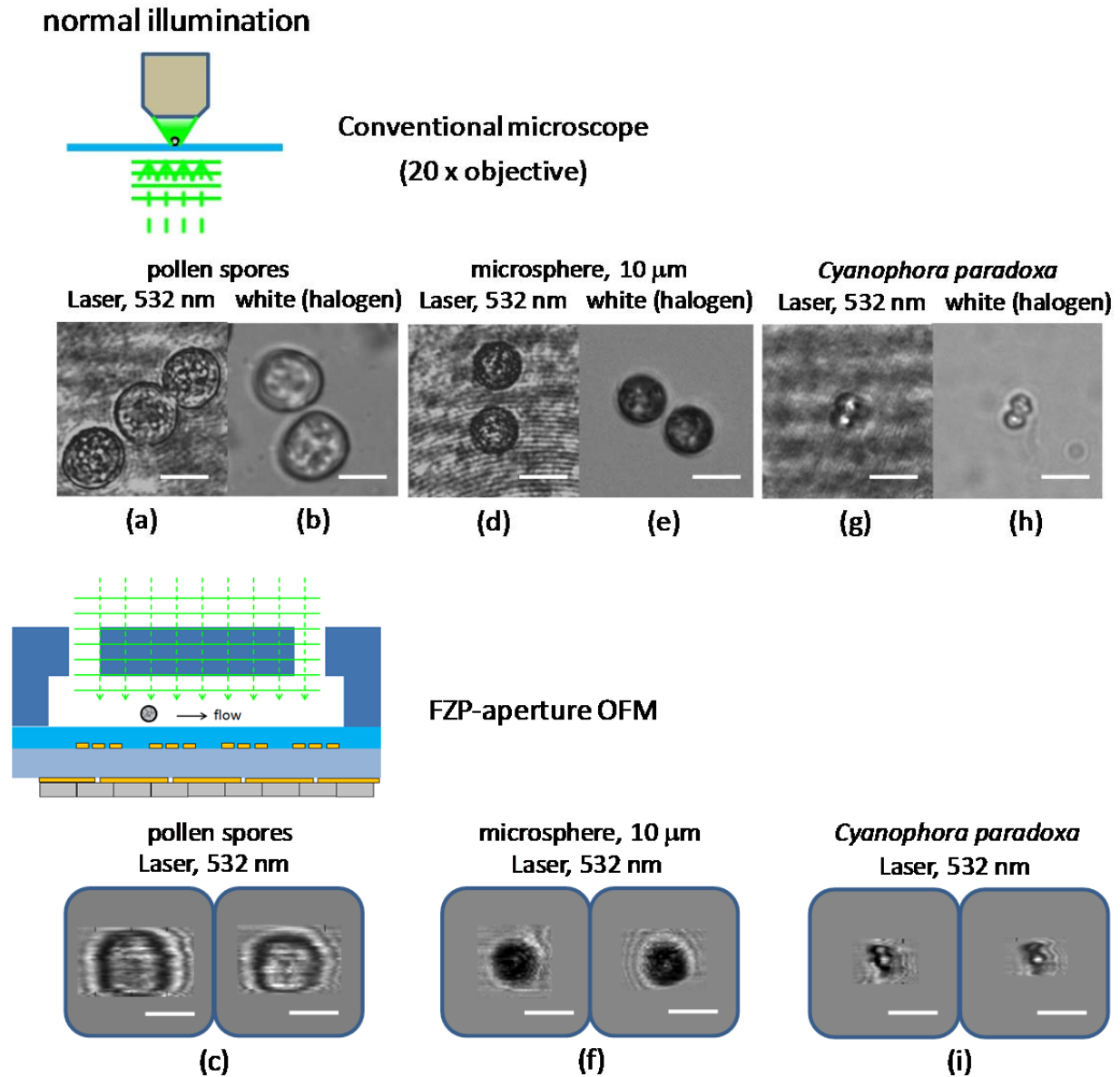
Figure 3.2.3 An experimental demonstration of several bright field images. Images acquired from a conventional light transmission microscope under a 20× objective with normal laser and halogen illumination, respectively, of mulberry pollen spores (a),(b), 10 µm polystyrene microsphere (d),(e), and *Cyanophora paradoxa* (g),(h). Images acquired from the FZP-aperture OFM by normal laser illumination mulberry pollen spores (c), a 10 µm polystyrene microsphere (f), and *Cyanophora paradoxa* (i)

(Scale bars: 10 µm)

3.2.3.1 Optical Resolution and Depth of Focus

A set of experiments have been conducted to characterize and investigate the optical property of the collection-FZP-aperture unit in comparison with other configurations. Four different cases are studied as illustrated in Figure 3.2.3.1.1. A laser (Excelsior-532-200-CDRH, Spectra Physics, with wavelength of 532 nm and power of 200 mW) is used as the light source. The laser is attenuated and expanded to a collimated Gaussian beam. The beam is then focused by a 60× microscope objective (NA = 0.95) to create a tightly focus spot with focal plane FWHM of 340 nm. I scanned the tightly focused light spot in the x-direction at different heights in z-direction, measuring from the sample substrate surface. Then, I plotted the intensity profile from the CMOS imaging sensor and fitted the curve with a Gaussian profile, in order to determine the PSF of the optical system. Using that profile, we calculated the FWHM in x-direction as shown in Fig 3.2.3.1.2. In order to determine the PSF of an optical system, we should use an infinitesimal point source, which is difficult to implement in our current experimental setup. Thus, a numerical study with a point source is used to simulate and compare with experimental findings. The details of the numerical scheme formulation are described in Appendix A.3. I also incorporated a Gaussian beam with the beam waist and focus of depth similar to the 60× microscope objective for cross validation. Four sets of devices are fabricated for this study. The first device has no structure, which is a plain CMOS sensor pixel. The second device has a zone plate designed with object distance $p = 10$ μm and image distance of $q = 25$ μm on a spacing layer with a thickness of 10 μm but without the pinhole aperture. The third device has a pinhole, with 1 μm diameter at the center pixel, which is similar to the single-layer collection aperture device studied in the first half of this chapter. The fourth design is the FZP-aperture, which consists of both the pinhole and FZP. Since we are conducting this characterization experiment in air ($\mu_{air} = 1.0$), the protective PMMA layer is omitted and the zonal radius of the FZP has been modified to accommodate this change. The FZP is designed to have object distance $p = 10$ μm and

image distance of $q = 25$ µm. The magnification is $M = q/p = 2.5$. The pinhole diameter is 1 µm. For the first configuration, where there is no structure. As expected, the best resolution is about the pitch of one pixel of the CMOS imaging sensor and the focal plane is on the CMOS pixel surface. For the second configuration where we incorporate the use of FZP, the best spatial resolution is similar to the first case, where there is no structure. However, in this case, we can move the focal plane to a height of about 10 µm above of the FZP plane, which is as consistent with our design. In the third case, where we have a pinhole aperture for collection, the FWHM is about the size of the aperture and the focal plane is closed to the surface. This result is complementary to the NSOM study [7]. In the last case, for the collection-FZP-aperture configuration, the FWHM at the focal plane ($z = 11$ µm) is 650 nm in experiments and 475 nm in simulations. I believe the slight shift of the focal plane (originally designed to be on $z = 10$ µm) is due to the lumped refractive index assumption in the zone plate design. In general, the experimental and numerical results match reasonably well. In Figure 3.2.3.1.2(a), which should act as the benchmark scheme of this study, it is a bit surprising that the experimental FWHM values match better to the simulation results with a point source than with the Gaussian beam propagation. I proposed two reasons to explain this. First, in numerical simulations, I use the entire pixel area for collection (fill factor = 1), which may not reflect the real situation in experiment. Second, I did not remove the microlens on top of the sensor pixel and it may have focusing effect on the diverging Gaussian beam and lead to a smaller FWHM value. In Figure 3.2.3.1.2(c), when we limit the active collection area to a 1 µm aperture, the FWHM experimental data matches well with the numerical result of Gaussian beam. This agrees with our expectation. We also observe a noticeable deviation of normalized intensity reading between experimental and numerical results shown in Figure 3.2.3.1.2(a),(b). This deviation can be attributed to the presence of micro-lens on top of the sensor pixel, which facilities the light collection at different heights near the focal plane. The Rayleigh range of the optical systems of FZP-aperture is estimated to be 2.6 µm in experiments and 3.4 µm in numerical simulations. A normalized peak intensity pixel reading from is plotted complementary to each data point with the FWHM value. Note that the above

experimental results are based on a collection-FZP-aperture unit with the purpose to characterize and study the PSF of the optical system. The collection FZP-aperture unit is not bonded with the microfluidic channel to form an OFM device. The characterization of the variations in optical performance of individual collection FZP-aperture unit in the bonded OFM device will be presented in Appendix A.4.
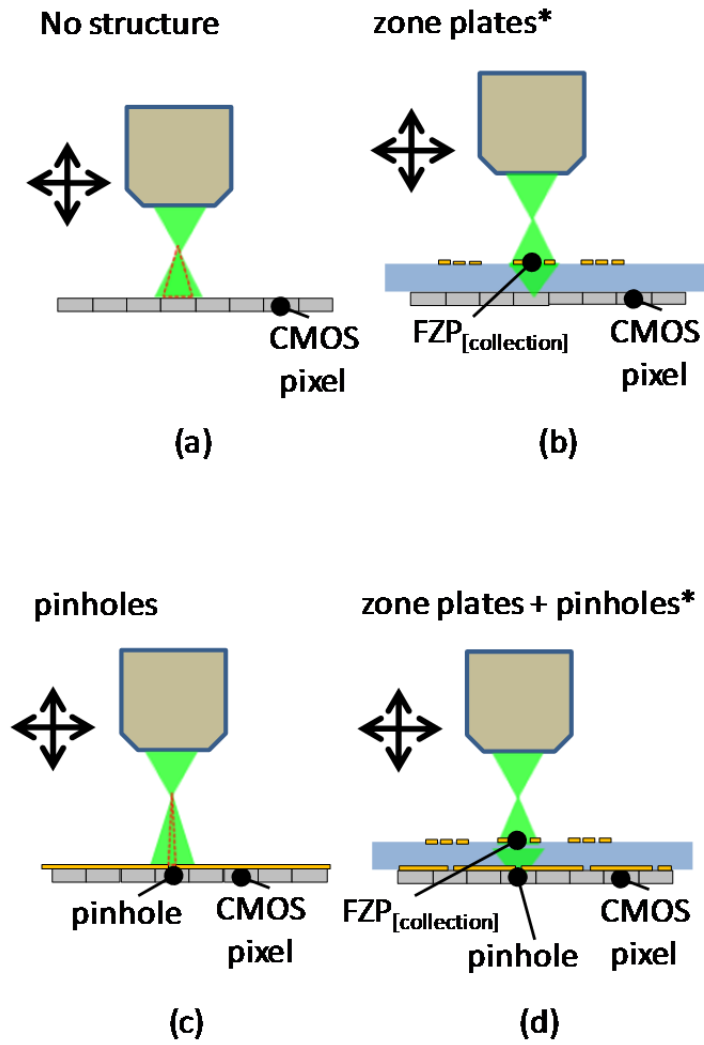
Figure 3.2.3.1.1 An illustration of the experimental setup to determine the FWHM of the PSF at different heights by a light spot (340nm) tightly focused by a $60 \times$ objective for several collection optics configurations on the CMOS pixel (a) no structure (b) FZP (c) aperture and (d) FZP-aperture
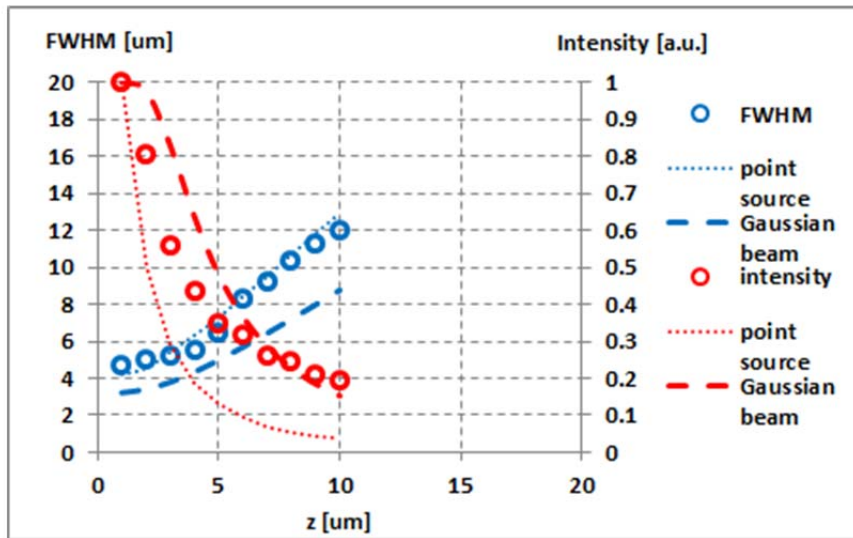
(a)
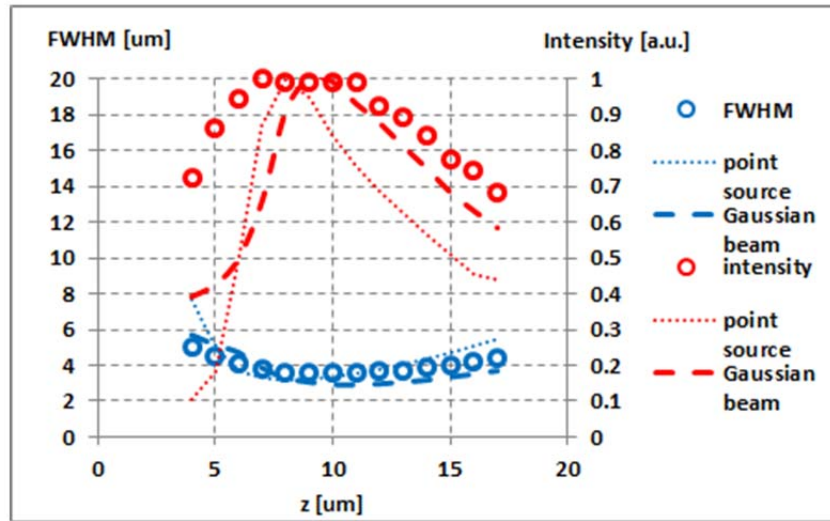
(b)
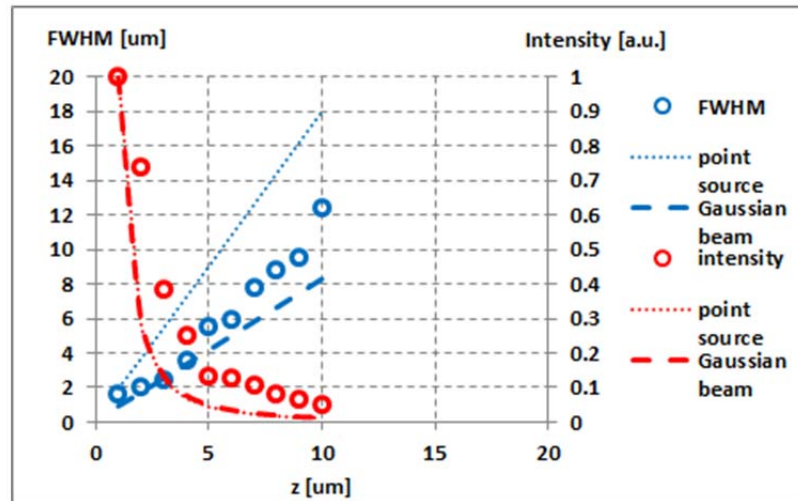
(c)
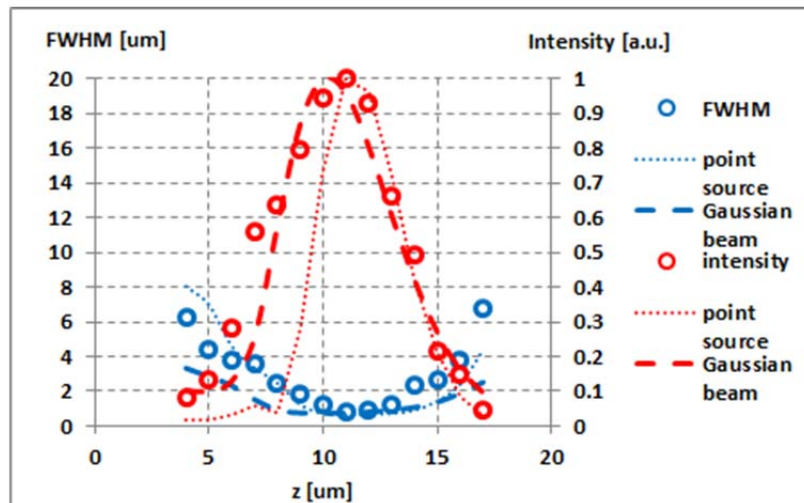
(d)

Figure 3.2.3.1.2 A set of plotting illustrating the FWHM of the PSF and the intensity response at different heights for several collection optics configurations on the CMOS pixel (a) no structure (b) FZP (c) aperture and (d) FZP-aperture in comparison with numerical simulation results [circles represent experiment data points and broken lines represent numerical results; z is measuring from the sample substrate surface]

3.2.4 Demonstration in Dark Field FZP-Aperture OFM Imaging

Although optical resolution is one of the most important parameters in determining the image quality of an optical system, there are other factors affecting the ultimate image quality. One of those factors is image contrast. In standard bright field optical microscopy, light that impinges on the biological sample has to be scattered or absorbed by features in the sample in order to provide image contrast. In other words, the image always has a bright background and the features always appear to be darker. This can impose a limitation in image contrast and mask weak scattering or absorbing features even their size is already larger the optical resolution limit. This limitation can be attributed to the following reasons. First, the bright background from the illumination light source can introduce a proportionate noise term and intensity decrement by scattering or absorption that the features must exceed to be observable. Second, our eyes or the recording camera in an optical microscope have a limited dynamic range that can be adjusted to the bright background. As the bit depths of most measurement systems are finite, if the decrement brightness of the optical scatterers or absorbers versus the background is smaller than this scale, the sample feature will simply be indistinguishable from its bright background. For this reason, in bright field microscopy, biological samples sometimes need to be artificially stained to enhance the image contrast. However, dye staining often causes death in biological samples, preventing us from visualizing transparent living materials.

Dark field microscopy can enhance the image contrast in unstained samples by blocking the illumination light and collecting only the scattering light from biological samples. In conventional dark field optical microscopy, as shown in Figure 3.2.4.1(a), rather than illuminating the biological sample with a filled cone of light as in bright field microscopy, a dark field patch stop is positioned before the condenser to form a hollow cone of light. The outer ring of illumination is then focused by an objective

lens onto the biological specimen. As the illumination light enters at an off-angle to the sample, most of it is directly transmitted and blocked by the illumination block in front of the collection objective. Only scattered light from the biological samples will enter the objective and produce the image. Dark field images appear to be bright against the dark background. The collection FZP-aperture can be operated in dark field mode by correctly tilting the illumination angle. As illustrated in Figure 3.2.4.1 (b), under the tilted plane wave illumination, the illumination light will form a focus in the spacing SU-8 layer and the collection aperture in the FZP-aperture unit will block a significant large amount of the illumination light (marked with a solid line). The FZP collects side-scattered light from the biological sample at the conjugate focus and the scatter from the sample enters the aperture, forming the dark field image (marked with a dotted line).

(a) (b)
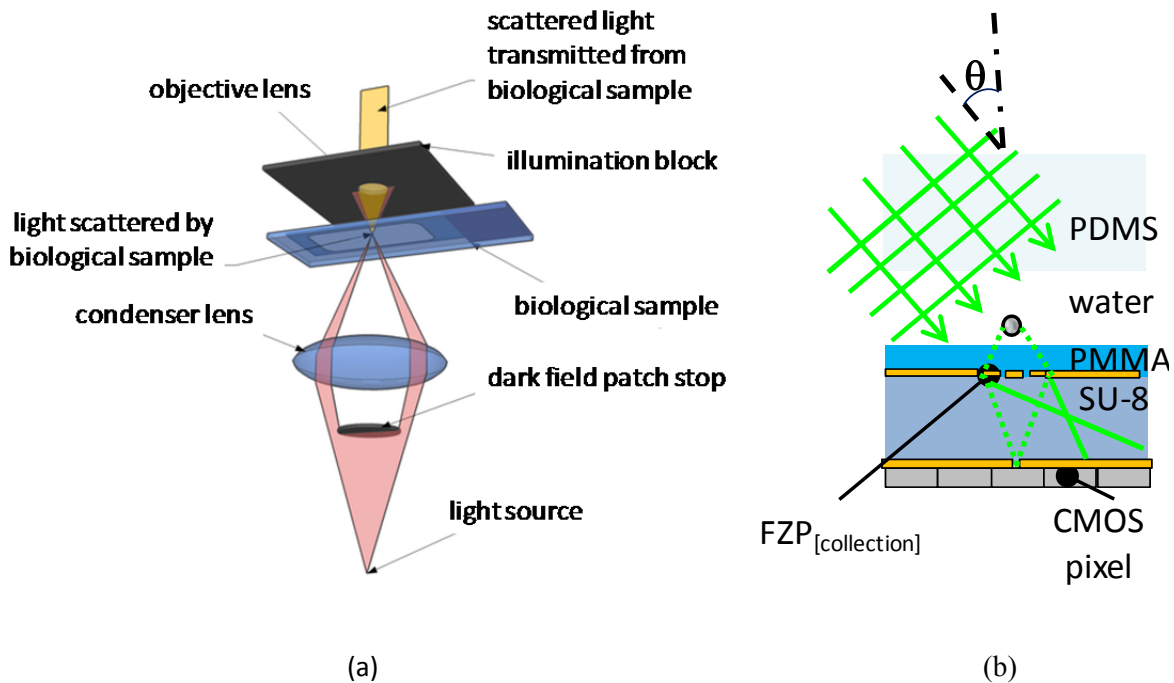
Figure 3.2.4.1 An illustration of dark field imaging scheme. (a) The planar geometry and the aperture array arrangement of the on-chip OFM. (b) A cross-sectional scheme of the OFM device. (c) A photo of the fabricated on-chip OFM device

To evaluate the optical performance of collection-FZP-aperture devices for dark field imaging, a rotation stage with a reflection mirror has been incorporated into the experimental setup, as shown in Figure 3.2.4.2. The illumination angle, θ, calculated at the air/PDMS interface, was tilted from normal to 30° and the intensity response of the CMOS sensor pixel is plotted in Figure 3.2.4.3 in comparison with numerical simulation results. The intensity reading is collected by averaging 4000 data points with an exposure time of 0.5 ms on a single pixel. A tilted illumination angle of 24° was selected since the pixel reading of the CMOS imaging sensor has been significantly suppressed to 1% compared with normal illumination, which is the lowest of all the data points. This value is about 4 times of that of the pixel dark current reading.
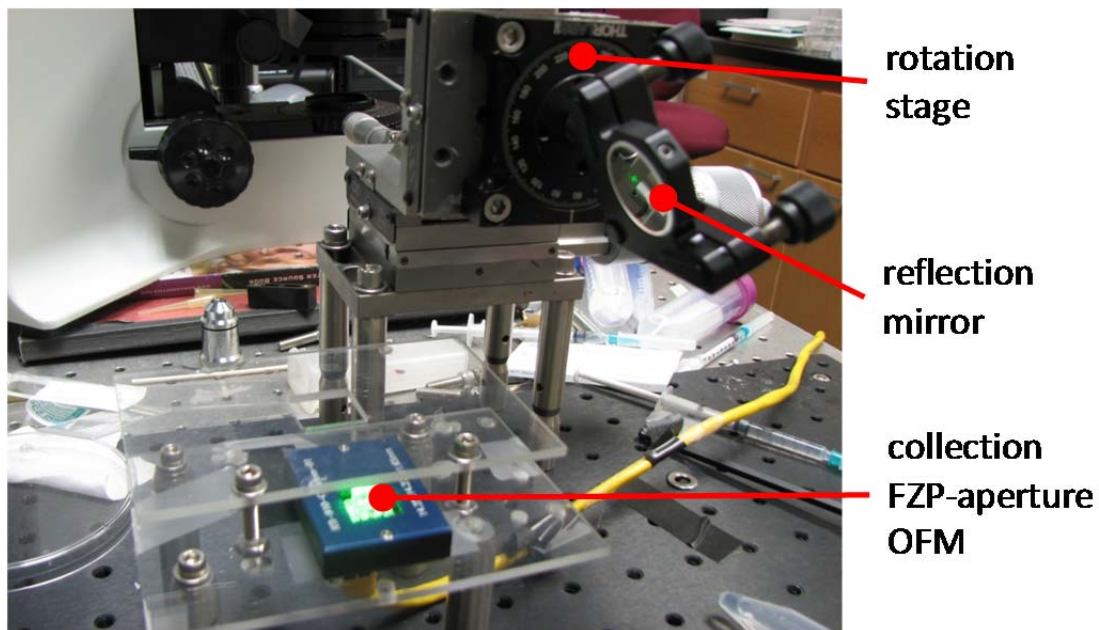
Figure 3.2.4.2 An illustration of experimental setup for tilted illumination in dark field collection-mode FZP-aperture OFM imaging
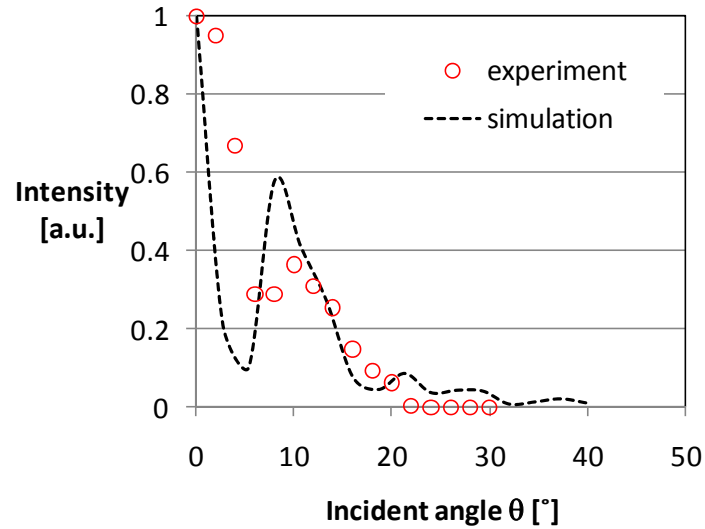
Figure 3.2.4.3 A plotting of light intensity detected versus the incident angle in illumination light suppression for dark field collection-mode OFM imaging

Under tilted illumination with inclination angle of 24°, a set of dark field images of pollen spores, 10 μm microspheres, and *Cyanophora paradoxa* were acquired from the collection-FZP-aperture OFM device and compared with a conventional light-transmission optical microscope. In tilted coherent illumination comparison, the condenser of the optical microscope is removed and the plane wave laser light is illuminated at an inclined angle to the biological specimen. For incoherent illumination, a high-intensity fiber light is used as the light source. Figure 3.2.4.4(a), (b) shows dark field images of the pollen spores acquired with a microscope (Olympus BX41) through a 20× objective with focal plane resolution of 650 nm under coherent and incoherent illumination, respectively. Figure 3.2.4.4(c) is the FZP-aperture OFM image of pollen spores. We also showed the images in a similar manner for a 10 μm microsphere and *Cyanophora paradoxa*, in Figure 3.2.4.4(d)–(f) and Figure 3.2.4.4 (g)–(i) respectively. All the OFM images were acquired based on the second FZP line array, with $q_{water} = 5$ μm.
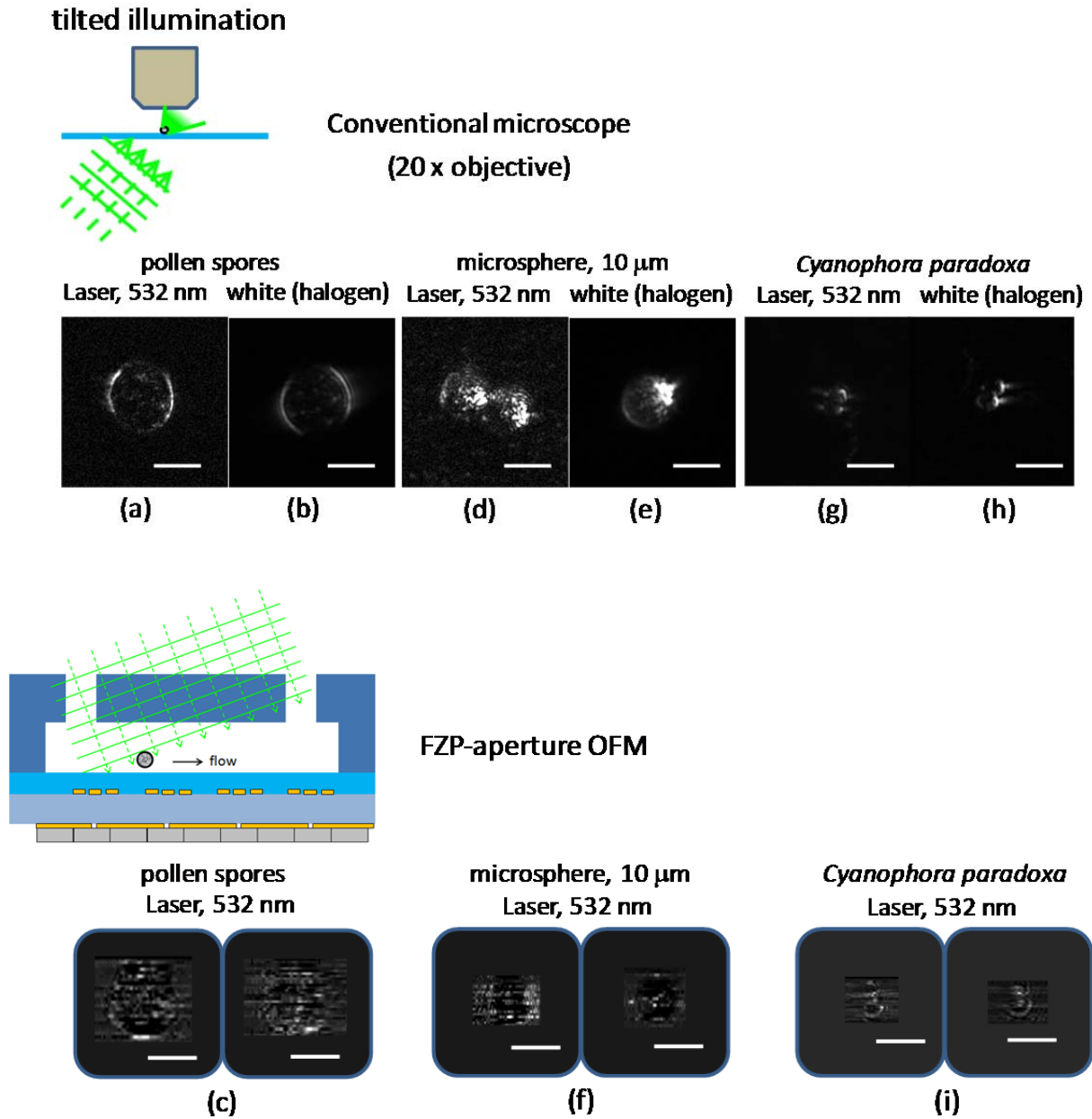
Figure 3.2.4.4 An experimental demonstration of several dark field images. Images acquired from a conventional light transmission microscope under a 20× objective with tilted laser and halogen illumination respectively of mulberry pollen spores (a),(b), 10 µm polystyrene microsphere (d),(e), and *Cyanophora paradoxa* (g),(h). Images acquired from the FZP-aperture OFM by tilted laser illumination of mulberry pollen spores (c), a 10 µm polystyrene microsphere (f), and *Cyanophora paradoxa* (i)

(Scale bars: 10 µm)

In the dark field FZP-aperture OFM images shown in Figure 3.2.4.4(c) and (i), the cell walls of the biological samples are clearly distinguishable from those from a conventional microscope (Figure 3.2.4.4(a), (b) and (g), (h)). The boundary of microspheres is less distinctive since the optical material within the sphere is homogeneous and the refractive index is uniformly distributed. Our implementation of dark field microscopy is by tilted illumination, rather by placing a patch stop in front of the condenser to create a hollow cone of illumination. Thus, a lensing effect is observed in the microsphere images in Figure 3.2.4.4(d), (e) in one light spot at one side of the microsphere. For the same reason, the bright ring structures on the cell walls of the biological samples in Figure 3.2.4.4(a), (b) and (g), (h) are not circularly symmetrical. We observed a similar effect for the FZP-aperture dark field images.

We also observed that the FZP-aperture images appear to have horizontal line patterns in the background along the microfluidic flow direction. This problem is attributed to the variation in the imaging sensor response on an individual pixel in low-intensity detection. I believe this issue can be solved by a more careful intensity normalization process between each pixel line. In dark field imaging, the background of the image should be zero and the features within the biological samples should always appear to be brighter than the background. However, we find that in the dark field FZP-aperture images some parts of the internal features are darker than the background. This means the illumination light is not fully suppressed in the tilted FZP-aperture dark field OFM implementation. We should be able to suppress the illumination light even more by increasing the tilted angle for illumination. An ideal situation would be a side-illumination mode. This implementation will require a better optical design in building the OFM device.

Finally, we find that there are some limitations on dark field imaging in OFM implementations. Since optical scattering light from biological samples is usually very weak, the illumination light intensity

has to be raised at least 100 times compared to the intensity used in normal illumination. This can cause overheating or even bubble generation in the microfluidic channel. Furthermore, since dark field imaging relies on a tilted or side illumination, the actual size of biological specimens can be impacted or the width of target objects can be exaggerated. This problem is more apparent if we want to image thick specimens. Last, since dark field imaging boosts the image contrast, the sample solution may have to be filtered contaminants in the cell suspension do not overlap with the OFM images and cause confusion.

References

[1] X. Cui, M. Lew and C. Yang, "Quantitative differential interference contrast microscopy based on structured-aperture interference," *Applied Physics Letters* **93**, 091113 (2008)

[2] G. Zheng, X. Cui and C. Yang, "Surface-Wave-Enabled Darkfield Aperture: A method for suppressing background during weak signal detection," *Proceedings of the National Academy of Science of the United States of America* **107**, 9043–9048 (2010)

[3] E. A. Ash and G. Nicholls, "Super-resolution aperture scanning microscope," *Nature* **237**, 510–512 (1972)

[4] U. Dürig, D. Pohl and F. Rohner, "Near field optical scanning microscopy," *Journal of Applied Physics* **59**, 3318–3327 (1986)

[5] X. Heng, X. Cui, D. W. Knapp, J. Wu, Z. Yaqoob, E. J. McDowell, D. Psaltis and C. Yang, "Theoretical modeling and experimental characterization of the collection of light through a nanoaperture from a point source," *Optics Express* **14**, 10410–10425 (2006)

[6] X. Cui, L. M. Lee, X. Heng, W. Zhong, P. W. Sternberg, D. Psaltis and C. Yang, "Lensless high-resolution on-chip optofluidic microscopes for *Caenorhabditis elegans* and cell imaging," *Proceedings of the National Academy of Science of the United States of America* **105**, 10670–10675 (2008)

[7] Y. M. Wang, G. Zheng and C. Yang, "Characterization of acceptance angles of small circular apertures," *Optics Express* **17**, 23903–23913 (2009)

[8] L. M. Lee, X. Cui and C. Yang, "The application of on-chip optofluidic microscopy for imaging *Giardia lamblia* trophozoites and cysts," *Biomedical Microdevices* **11**, 951–958 (2009)

[9] X. Heng, E. Hsiao, D. Psaltis and C. Yang, "An optical tweezer actuated, nanoaperture-grid based optofluidic microscope implementation," *Optics Express* **15**, 16367–16375 (2007)

[10] J.-A. Conchello and J. W. Lichtman, "Optical sectioning microscopy," *Nature Methods* **2**, 920–931 (2005)

[11] D. Daly, R. F. Stevens, M. C. Hutley and N. Davies, "The manufacture of microlenses by melting photoresist," *Measurement Science and Technology* **1**, 759–766 (1990)

[12] A. Tripathi, T. V. Chokshi, and N. Chronis, "A high numerical aperture, polymer-based, planar microlens array," **17**, *Optics Express* 19908–19918 (2009)

[13] A. E. Siegman, *Lasers*, University Science Books (1986)

[14] D. T. Attwood, *Soft X-Rays and Extreme Ultraviolet Radiation: Principles and Applications*, Cambridge University Press, 1st edition (2007)

[15] J. Wu, X. Cui, L. M. Lee and C. Yang, "The application of Fresnel zone plate based projection in optofluidic microscopy," *Optics Express* **16**, 15595–15602 (2008)

[16] E. Schonbrun, A. R. Abate, P. E. Steinvurzel, D. A. Weitz and K. B. Crozier, "High-throughput fluorescence detection using an integrated zone plate array," *Lab on a Chip* **10**, 852–856 (2010)

[17] E. Schonbrun, P. E. Steinvurzel and K. B. Crozier, "A microfluidic fluorescence measurement system using an astigmatic diffractive microlens array," *Optics Express* **19**, 1385–1394 (2011)

[18] R. M. Henkelman and J. J. Bronskill, "Imaging extended objects with a Fresnel-zoneplate aperture," *Journal of the Optical Society of America A* **64**, 134–137 (1974)

[19] M. Young, "Zone plates and their aberrations," *Journal of the Optical Society of America A* **62**, 972–976 (1972)

[20] A. R. Jones, "The focal properties of phase zone plates," *Journal of Physics D* **2**, 1789–1791 (1969)

[21] H. Lan, Y. Ding and H. Liu, *Nanoimprint lithography: principles, processes and materials*, Nova Science Pub, Inc. (2011)

Chapter 4: Illumination-mode Optofluidic Microscope

In the previous chapter, I reported the successful development of one-layer and two-layer collection-mode OFM prototypes. Here I would like to extend my study to the illumination mode of OFM prototypes. The first implementation of illumination-mode OFM was demonstrated in 2008 in an off-chip scheme [1]. An optical tweezers was used to translate targeted samples in close proximity with a 2D grid of nano-aperture illumination structure. Light transmitted through the sub-wavelength-sized (100 nm) apertures are collected by a conventional microscope objective onto a high-speed CCD camera, generating sub-wavelength high-resolution images. In my implementation of chip-level illumination-mode on OFM imaging, the diffractive optical elements are completely integrated with the microfluidic channel and the CMOS imaging sensor. The illumination light field can be modulated through several different means, such as a holographic plate or FZP array from the top of a microfluidic channel to create line arrays of tightly focused spots, with submicron size, in the microfluidic channel. When a biological sample is flowing across and intersects with the line array of focused spots, the light intensity change of the light spot will be detected by the undressed CMOS imaging sensor pixel at the bottom of the microfluidic channel. In illumination-mode OFM systems, the image resolution is fundamentally determined by the size of the focused light spots. In this chapter, I will start by presenting my effort to incorporate a holographic recording and playback approach to permanently generate a focused light-spot array in the compact OFM device. Although we can occasionally demonstrate relatively good quality of OFM images, we cannot generate repeatable results mainly due to the incompatibility in microfabrication technique and alignment difficulty in the bonding process. Another method to generate a focused light-spot array in a microfluidic channel is the FZP approach. By proper design of the focusing property of the FZP, I have shown improvements in both the generated focused-spot size and fabrication repeatability. I believe my effort in developing the illumination mode of a chip-level OFM prototype has paved the way for the

successful implementations of fluorescence-enabled OFM and complete confocal OFM systems at the chip-level. In fluorescence-enabled OFM, an optical filter is spin coated on the CMOS sensor pixel to block excitation light and allow emission light from the fluorescent biological sample to pass through for OFM image formation. Since there are no collection optics associated with the chip-level illumination-mode OFM systems, if the focused light spots are positioned significantly above the bottom of the microfluidic channel, we will not be able to collect all the light, due to the limited sensor-pixel size. We will present these findings at the end of this chapter. The defocusing problem actually motivates us to develop a complete confocal OFM system.

4.1   Holographic Approach to Create Focused Light Spots

The most common approach to generating an array of focused spots is by micro lenslet. Microlenses focus light by refraction with an optical resolution limit of about 1aµm, for a relatively large focal length of about 100 µm. However, the fabrication of a microlens array usually requires a very well controlled photoresist hard-bake reflow process [2]. Commercially available lenslets are made in high quality with high spot-to-background ratio. Some companies can even customize the focusing property. However, the manufacture cost is expensive and the process usually takes a long time. Furthermore, it is impossible to pack individual microlens units to create closely separated light spots. Most commercial lenslets have a pitch size of 150 µm [3]. It also takes a substantial amount of effort to develop a reliable and repeatable bonding and alignment scheme to integrate the microlens platform with compact OFM systems, due to the compatibility problem with standard microfabrication technique. All these restrictions motivate us to explore alternatives to generate a line array of tightly focused spots. One approach is by in-line holography [4]. The recording of inline holography involves interference of two coherent laser beams. The adaptation of such holographic recording scheme in on-chip OFM application is shown in Figure 4.1(a). The reference beam is the direct transmission of the incoming collimated laser beam through a mask coated with a thin metal film, and the sample beam is the transmission of the laser through the lines array of small apertures fabricated on the mask. The interference of the two laser beams is then recorded by a holographic plate positioned behind the mask. The thickness of the gold metal mask is set at 200 nm. The attenuated light intensity from the mask matches that diffracted from the aperture to achieve the best recording result. The holographic plate and the metal masks are clumped together with a hard contact. Two lines of aperture arrays are fabricated on the metal mask. A layer of SU-8, 15 µm thick is spin coated on the metal mask and a window is opened on one line of the aperture array. In the playback scheme shown in Figure 4.1(b), this configuration allows the generation of two lines of different depths inside the microfluidic channel. By design, the first line of holographic focused light-spot array, in which the

apertures are covered with SU-8 in the holographic recording, will focus at a depth of 12 μm (measuring from top wall of the microfluidic channel in the playback). The second line in the holographic recording is not covered with SU-8 and exposed to air. This line of holographic generated light spots is designed to have a focal plane at depth of 18 μm in the playback. These 2 lines have a lateral shift of 5.2 μm, which is equivalent to the pitch of one pixel.

(a)

(b)
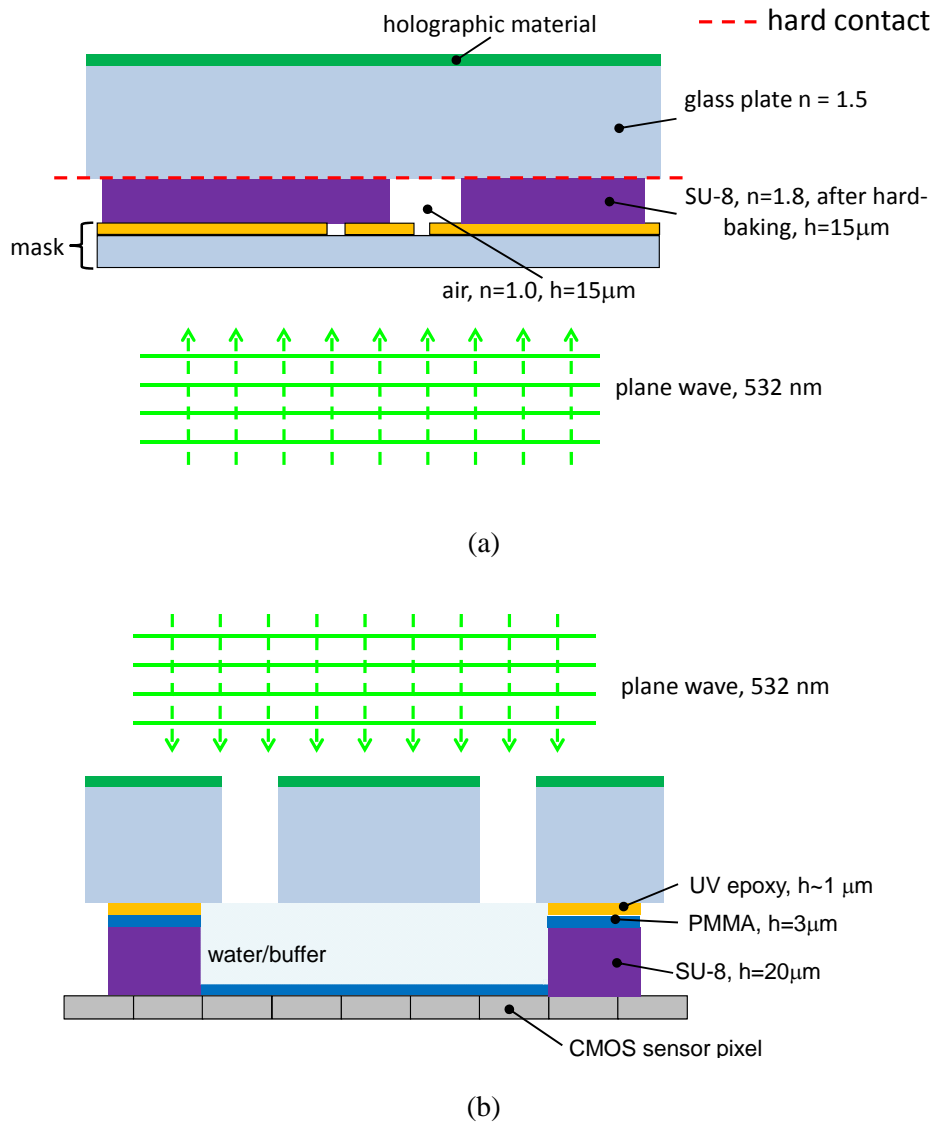
Figure 4.1 A schematic of the fabrication process for the illumination-mode holographic OFM device in holographic plate (a) recording and (b) playback

For the fabrication of the holographic illumination-mode OFM, the holographic plate (Integraf, Inc., JD-2 kit) is developed, bleached, and diced. The holographic illumination unit is then aligned and bonded with the OFM substrate under a contract aligner. The microfluidic channel is designed to be about 20 µm tall and 40 µm wide. Before the bonding of the OFM device, the diced holographic plate is placed under a conventional microscope to determine the size of the light spot. A collimated laser beam at 532 nm is adjusted in a normal incident angle. Under a 40× water immersion objective, the first line of holographic plate, the focused light spot measured an average size of 630 nm FWHM at its focal plane. The light spots decayed to 1.4 µm FWHM when we moved the detection planes 6 µm apart. The second line of holographic plate measured an average light-spot size of 740 nm FWHM at the focal plane and decayed to about 3 µm FWHM when we moved them 6 µm apart. For each line, there are 120 focused light spots with a separation of 10.4 µm, equivalent to two CMOS sensor pixels. The slanted angle between the lines of focused spots and the microfluidic channel is 2°.

4.1.1 Demonstration in Bright Field Holographic OFM Imaging

A collimated laser beam, with wavelength of 532 nm, diameter 12 mm, and power approximately 1 mW, is used as the illumination source. The laser beam is adjusted to a normal incident angle by observing the reflection from the top surface of the holographic plate. The OFM device is operated with a frame rate of 2000 per second and an exposure time of 0.5 ms. The biological samples are driven in a similar way as the collection mode OFM device, as discussed in Chapter 3. The average microfluidic flow speed is 600 $\mu m \cdot s^{-1}$. Two illumination-mode bright field holographic OFM images on mulberry pollen spores are shown in Figure 4.1.1(a),(b). Both OFM images are acquired from the first line of the holographic illumination spot array, in which the focal depth is 12 μm, measuring from the top channel wall. For comparison, three images of a pollen spore at different focal planes acquired with a conventional microscope (BX-45) under a 20× objective, with focal plane resolution of 650 nm and NA = 0.5, are shown in Figure 4.1.1(c)–(e). The samples are incoherently illuminated under a halogen lamp source. The focal plane of the microscope is positioned at three different points, with a step size of 4 μm. While we can still discern the internal features of the illumination-mode holographic OFM images quite well, the cell walls of the pollen spores appear to be blurry compared with those acquired by conventional optical microscopy. The problem may be that the pollen spores are not flowing exactly on the focal plane of the illumination holographic spots. This may be due to the fact that the height of the microfluidic channel is actually taller than designed, since there is no guarantee of quality control in the curvature of the holographic glass plates. I also expect there is some variation on the thickness of UV epoxy (SK-9, Summers Optical) in the bonding process. In addition, I also experienced a lot of difficulties in the alignment of the holographic plate with the microfluidic channel since I could only rely on the diffraction patterns on the holographic plate for alignment. I spent a lot of effort calibrating the separation of illumination light spots to match the CMOS pixels in the metal aperture mask fabrication and holographic plate recording.

holographic illumination-mode OFM image

(a)   (b)

**conventional light transmission microscope
20x objective**

z_{ref} = -4µm z_{ref} = 0µm z_{ref} = +4µm
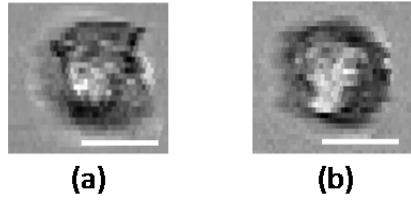
(c)   (d)   (e)
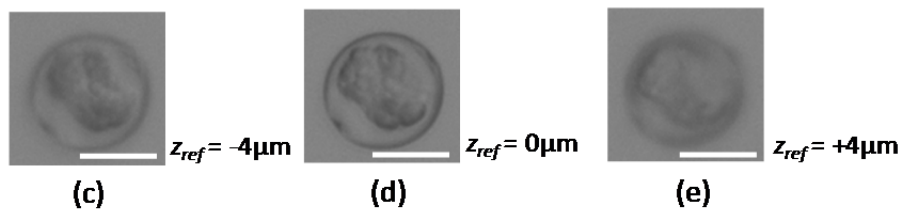
Figure 4.1.1 An experimental demonstration of mulberry pollen spore images from (a),(b) the bright field holographic OFM device (c)–(e) a conventional optical microscope under a 20× objective with focal plane resolution 650 nm and NA = 0.5 (z_{ref}= 0) at different detection planes (scale bar: 10 µm)

4.2   FZP Approach to create Focused Light Spots

Since the holographic approach cannot produce consistent results, I switched to using FZP to generate tightly focused illumination spot arrays. The design of illumination FZP is actually simpler than that of collection FZP in Chapter 3. In plane wave illumination, the formulation of the FZP zonal radius was discussed in Section 3.2.1. The only modification here is to adapt the formulation to the medium of water along the light propagation direction, as shown in Figure 4.2.1.
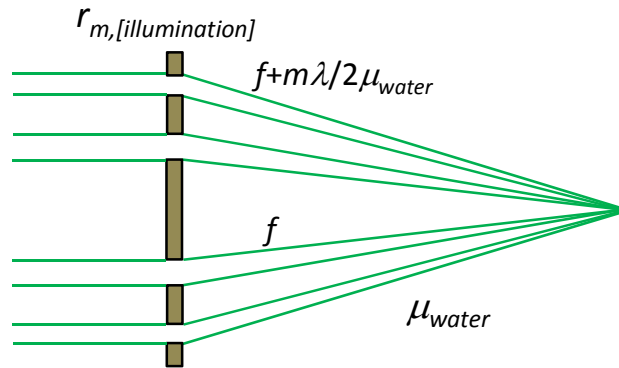
Figure 4.2.1 An illustration of the working principle of the illumination FZP unit under a collimated laser beam

The zonal radius of illumination-FZP can be found as follows:

$$r_{m,[illu\,min\,ation]} = \sqrt{\frac{m\lambda}{\mu_{water}} + \left(\frac{m\lambda}{2\mu_{water}}\right)^2} \qquad (4\text{-}1)$$

where λ is the illumination wavelength and μ_{water} is the refractive index of water. Several zonal radii of FZP design for different focal lengths under an illumination wavelength of 532 nm are listed in Table 4.2.

1	n	l=532			
2		f=5	f=10	f=15	f=20
3					
4	1	1.43	2.01	2.46	2.84
5	2	2.04	2.86	3.49	4.02
6	3	2.52	3.52	4.28	4.94
7	4	2.94	4.08	4.96	5.71
8	5	3.32	4.58	5.57	6.4
9	6	3.67	5.04	6.12	7.03
10	7	3.99	5.47	6.63	7.61
11	8	4.31	5.88	7.11	8.16
12	9	4.61	6.26	7.57	8.67
13	10	4.9	6.63	8	9.17
14	11	5.18	6.99	8.42	9.64
15	12	5.46	7.33	8.82	10.1
16	13	5.72	7.67	9.21	10.5
17	14	5.99	7.99	9.58	10.9
18	15	6.24	8.31	9.95	11.4
19	16	6.5	8.62	10.3	11.8
20	17	6.75	8.92	10.7	12.1
21	18	7	9.22	11	12.5
22	19	7.24	9.51	11.3	12.9
23	20	7.48	9.8	11.7	13.3
24	21	7.72	10.1	12	13.6

Table 4.2 The zonal radius of an illumination FZP design under a collimated laser source at 532nm

The FZP illumination focused-spot arrays are fabricated on a high-resolution chrome mask by Photronics, Inc. Line arrays of FZPs with different focal lengths are patterned on the chrome mask, with a line resolution limit of 400 nm. The chromium layer of the glass mask is 100 nm, which is thick enough to block almost all light transmission. In the illumination FZP design, the diameter of FZP is chosen to be less than 15.6 µm to prevent the overlapping of individual FZP units. The chrome mask is diced, drilled with holes for inlet and outlet ports, and used directly to form the top of the microfluidic channel, with the chromium side facing down. The FZP array illumination glass pieces are bonded with the CMOS imaging sensor in a similar manner to the holographic approach, forming the OFM device using UV epoxy. Figure4.2.2 (a) shows a pair of illumination FZPs with focal length of 10 µm under a 40× water immersion object with incoherent illumination in a conventional microscope. With a laser beam illumination of wavelength 532 nm, no light-focusing effect is observed at the FZP plane, as shown in

Figure 4.2.2(b); a pair of tightly focused spots is also formed at the focal length, which is 10 µm apart from the plane of FZPs as designed. An average FWHM of 360 nm is measured as shown in Figure 4.2.2(c). Note that the value is close to the line resolution limit of the chrome mask, which is 400nm since; FZP, the optical resolution is fundamentally determined by its size of the outermost zonal ring.
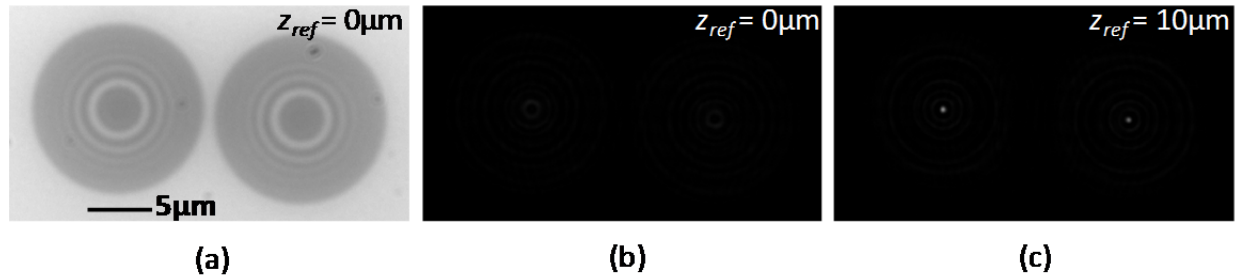
Figure 4.2.2 An experimental demonstration of a pair of illumination FZP units with focal length of 10 µm: (a) under a incoherent illumination (z_{ref}= 0µm) denotes the plane of the illumination FZP), (b),(c) under a coherent collimated laser illumination at 532 nm (scale bar: 10 µm)

The FZP approach is a more reliable method to generate tightly focused spot arrays in chip-level OFM systems. FZP-enabled, illumination-mode OFM schemes have directly led to the implementation of fluorescence microscopy imaging of biological samples in fluid media. This fluorescence-enabled OFM system uses a slanted line array of illumination FZP units to generate an array of focused light spots within a microfluidic channel, under a collimated laser illumination with wavelength matching the excitation spectrum of the fluorophore. As a fluorescence-tagged biological sample flows along the microfluidic channel, intersecting the line array of focused light spots, the fluorescence emissions from the sample are collected by a fluorescence-filter-coated CMOS sensor at the channel floor. The collected data can then be processed to render fluorescence microscopy images with optical resolution comparable to a bench-top microscope. This implementation has very recently been reported [5].

4.3   Talbot Approach to create Focused Light Spots

Other than holographic and FZP methods, there exist other methods to generate uniform, focused light-spot arrays based on diffractive optics. One of these approaches is by Talbot effect [6]. In the Talbot approach, a periodic 2-D array of apertures is fabricated on a metal mask and the mask is illuminated with a collimated laser beam. Light transmission through the aperture mask grid reproduces the same grid pattern at a regular distance from the mask. The distance interval, named the Talbot distance (Z_T), can be calculated as:

$$Z_T = \frac{2d^2}{\lambda}$$
(4-2)

where d is the period of the aperture pattern and λ is the illumination wavelength. The periodic light grid pattern reproduces itself at an integral increment of one unit of Talbot distance. The Talbot approach has several advantages. First, the focus grid on the metal mask can be manufactured more reliably. Similar to FZP implementation, the aperture mask can be readily fabricated by standard semiconductor microfabrication technique, and the mask can be used directly for illumination in contrast to the holographic approach. Second, the focused light spots are more uniformly illuminated. Since each focused light spot is a contribution from each aperture on the metal mask, the variation of light transmission through an individual aperture does not ultimately affect the formation of the focused light spots too much, due to this averaging effect. It is a major advantage over the holographic and FZP approach. Third, the Talbot effect allows tunable capability when we change the illumination wavelength. As shown in Equation (4-2), when we change the illumination wavelength, the Talbot distance, or plane of tightly focused grid, will change accordingly. However, the Talbot approach also suffers from several limitations making its integration with chip-scale OFM technology difficult. One limitation is that the Talbot effect usually has a long 'focal length'. For example, if we have a focused spot period of 15 µm and an illumination wavelength of 532 nm, the Talbot distance is about 1 mm. In chip-scale OFM

systems, the height of the microfluidic channel is usually made on the order of tens of microns. It requires a well-controlled alignment process to ensure that the replicate focus of the grid falls accurately at the desired depth in the microfluidic channel. In addition, the size of the focused light spot is usually larger than the aperture size on the mask, the smallest light spot size created by Talbot effect demonstrated in our group is about 1 µm with an aperture size of 800 nm. The Talbot approach is not as attractive as the FZP approach, in which we have already shown that we can achieve an illumination light-spot size of less than half a micron.
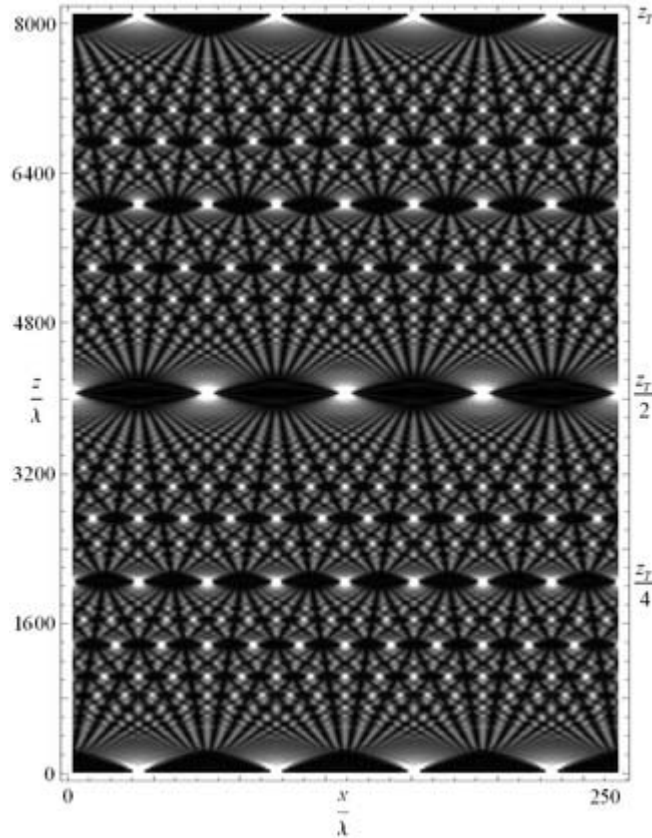
Figure 4.3 An illustration of Talbot effect

4.4　Limitations on Illumination-mode OFM Imaging

In this chapter, I presented my effort to integrate illumination optical elements in OFM devices on a chip-scale. In the holographic method, I successfully developed a novel recording and playback method to create two lines of focused light-spot array with an average spot size of 650 nm FWHM at different depths inside the microfluidic channel. However, due to incompatibility with standard microfluidic fabrication technique, I failed to produce repeatable results in the OFM device fabrication. The major difficulty arises from the variation in the flatness of holographic glass plates. This not only alters the bonding process, but also hinders precise height control of the microfluidic channel. Then, I switched to using FZP arrays to create illumination-focused light spots for OFM imaging. Since the FZP arrays are fabricated on a chrome glass mask used in standard semiconductor microfabrication, the roughness of the glass plate has better quality control; leading to a higher success rate in device fabrication. Furthermore, an improved optical resolution of the focused light spots was recorded: with 360 nm FWHM on average.

In addition to these technical challenges and constraints in the microfabrication process described above, illumination-mode OFM has a serious deficiency in optical configuration. Since there is no collection optics associated with illumination-mode OFM systems, we are essentially detecting defocused light at the detection plane. Thus, when designing illumination optical elements, the focused light spots have to be positioned either close enough to the undressed CMOS sensor pixel to prevent excessive spreading of light, or be sparsely separated to prevent crosstalk between successive light spots. Both cases are undesirable in OFM imaging and defeat our original intention to optically move the focal plane sufficiently far above the CMOS imaging sensor pixels to increase the separation of successive illumination spots and the length required for OFM imaging. The diffraction pattern from two lines of illumination spot arrays from a two-line array of FZP units with focal length 10 μm and 15 μm is shown

in Figure 4.4(a). Under a collimated laser illumination at 532 nm, the focus is positioned at the detection plane, 20 μm from the plane of the FZP array, with a 40× water immersion objective under a conventional microscope (BX45, Olympus). In Figure 4.4(b), the CMOS sensor pixel readout from a bonded illumination-mode holographic OFM device is illustrated. The microfluidic channel was filled with water. From the readout of the CMOS sensor, it is difficult to identify the center of the defocused diffraction pattern in bright field imaging formation.

under 40 x water immersion objective, focused on the detection plane

f = 10um

f = 15um

(a)

CMOS sensor pixel readout of the illumination mode holographic OFM device

(b)
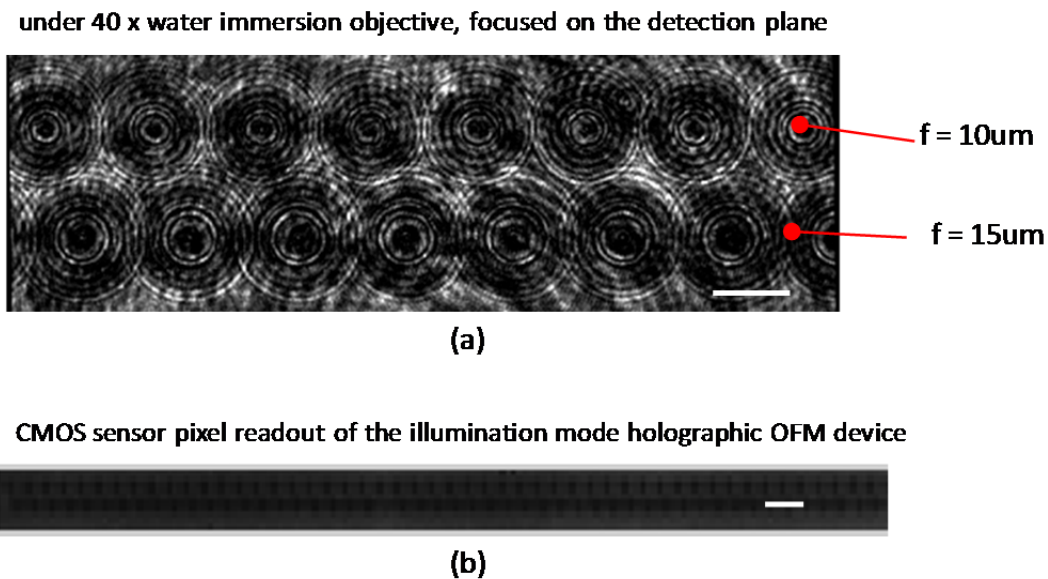
Figure 4.4 An experimental demonstration of (a) diffraction of two lines of illumination spots array from a two line arrays of FZP units with focal length 10 μm and 15μm where the detection plane is positioned 20 μm from the plane of the FZP array under a collimated laser illumination of 532 nm, and (b) the corresponding CMOS sensor pixel readout from an illumination mode holographic OFM device

(scale bar = 10 μm)

Nonetheless, the effort to incorporate illumination optics is an important milestone for the development of chip-level OFM systems. The defocusing problem actually motivates us to integrate

illumination and collection optical elements in OFM imaging, leading to a complete confocal OFM implementation.

References

[1] X. Heng, E. Hsiao, D. Psaltis and C. Yang, "An optical tweezer actuated, nanoaperture-grid based optofluidic microscope implementation," *Optics Express* **15**, 16367–16375 (2007)

[2] D. Daly, R. F. Stevens, M. C. Hutley and N. Davies, "The manufacture of microlenses by melting photoresist," *Measurement Science and Technology* **1**, 759–766 (1990)

[3] http://www.thorlabs.com/newgrouppage9.cfm?objectgroup_id=2861

[4] J. Wu, L. M. Lee and C. Yang, "Focus grid generation by in-line holography," *Optics Express* **18**, 14366–14374 (2010)

[5] S. Pang, H. Chao, L.M. Lee and C. Yang, "Fluorescence microscopy imaging with a Fresnel zone plate array based optofluidic microscope," submitted to *Lab on a Chip* (2011)

[6] J. Wu, G. Zheng, Z. Li and C. Yang, "Focal plane tuning in wide-field-of-view microscope with Talbot pattern illumination," *Optics Letters* **36**, 2179–2181 (2011)

Chapter 5: Illumination and Collection-Mode OFM

The effort to integrate collection and illumination optics in a chip-level OFM system has been discussed. We find that a Fresnel zone plate is an ideal optical element as a focusing unit for both light illumination and collection since the fabrication process is highly compatible with standard IC microfabrication processes. Thus, it is a natural progression to combine both illumination and collection optics to build a complete confocal OFM system, in which the image resolution, contrast, and SNR will be improved. FZP is an optical diffraction element, in which, by proper design of zonal radius, the light illumination or collection property can be manipulated, allowing another degree of freedom in OFM imaging. In this chapter, I will first demonstrate that with a set of both bright field illumination and collection zone plates, a confocal bright field imaging scheme can be implemented. With a set of bright field illumination and dark field collection zone plates, a confocal dark field OFM imaging scheme can potentially be realized. By incorporation of an illumination zone plate and a longer focal length bright field collection zone plate, a high resolution confocal fluorescence OFM imaging scheme can potentially be achieved by addition of an optical fluorescence filter. Although the motivation and advantages to integrate both illumination and collection optics in OFM systems is obvious, the implementation is not straightforward. The major difficulty arises from alignment issues. In confocal OFM systems, the target optical resolution of the confocal OFM image is about 0.5 µm. However, the tolerance of semiconductor fabrication by standard photolithography is about 2 µm. Furthermore, the height control of the microfluidic channel also plays an important role in axial alignment between the illumination and collection units. Despite those technology barriers, I believe successful integration of illumination and collection optics with advanced microfluidics technology will enable miniaturized flow cytometry for very large-scale imaging-based biological study and analysis.

5.1 Confocal Bright Field OFM Imaging

The schematic of confocal bright field configuration is shown in Figure 5.1. In Chapter 4, we demonstrated that the illumination FZP can create focused light spot size down to 360 nm FWHM under a plane wave laser illumination. In Chapter 3, the collection-FZP-aperture unit is able to collect light at the focal point with a FWHM of 650 nm. In a confocal OFM aperture configuration, the ultimate image resolution will be determined by superimposing the optical resolution of both illumination- and collection- FZP-aperture unit. This confocal configuration will not only increase the image resolution, both in the lateral and axial direction, but also enhance the contrast and SNR of the image. Since the illumination light is focused down into a tiny spot, contrary to the case of the collection-mode OFM systems, in which a plane wave is used as the illumination and the biological samples are flooded with illumination light, the image artifacts due to internal reflections within the biological samples and laser speckles are expected to be reduced.
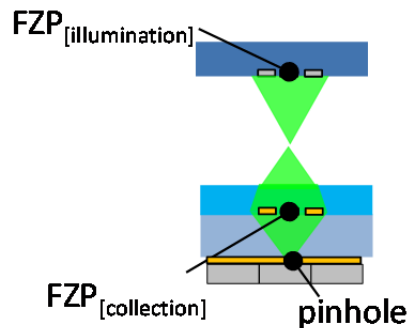
Figure 5.1 An illustration of bright field confocal OFM aperture configuration

5.1.1 Demonstration in Bright Field OFM Imaging

I have built a confocal OFM device to incorporate a set of illumination and collection FZPs to demonstrate bright field imaging. The fabrication process is similar to the collection-FZP-aperture OFM device presented in Chapter 3. The illumination-FZP array on a chrome glass piece is then bonded with the collection-FZP-aperture substrate using UV epoxy, which substitutes for the PDMS microfluidic channel in the implementation of a collection-FZP-aperture device. The alignment between the illumination- and collection-FZP arrays is performed under a contact aligner in a cleanroom. The height of the microfluidic channel is estimated to be about 20 µm. To ensure a normal incident angle, the collimated laser beam is tilted until maximum intensity readout is recorded in the CMOS sensor pixel of the confocal OFM device. Since there is no microfluidic control on the compact confocal OFM device, we cannot guarantee the biological samples are flowing at the focal plane of the FZP array. Nonetheless, a confocal OFM image on mulberry pollen spore is shown in Figure 5.1.1(a). The confocal OFM image seems to be distorted. I believe the high-resolution region is acquired from the part where the illumination- and collection-FZP array aligns well with each other, while the low-resolution region is from the part where the illumination- and collection-FZP arrays do not match. A set of conventional light-transmission microscopes under a 60× objective, with an optical resolution limit of 340 nm and NA = 0.95, when the focal plane is locked at different reference heights, is shown in Figure 5.1.1(b)–(d). We find that the high resolution region of the confocal OFM image is similar to the conventional optical microscope image when it is in focus, while the low-resolution region of the confocal OFM image is likely to be defocused.
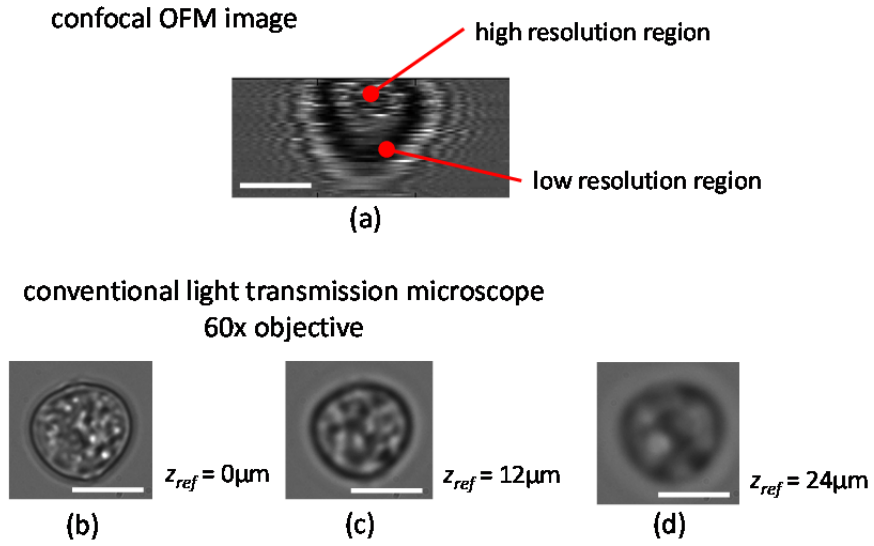
Figure 5.1.1 An experimental demonstration of mulberry pollen spore images from (a) the bright field confocal OFM device (b–d) a conventional optical microscope under a 60× objective with focal plane resolution 330 nm and NA = 0.95 (z_{ref}) at different detection planes (scale bar: 10 µm)

5.1.2 Alignment Issues

I believe the distortion of the bright field OFM image is due to the misalignment between the illumination and collection-FZP arrays, as illustrated in Figure 5.1.2. In Figure 5.1.2(a), under a 20× objective, the microscope is focused at the collection-FZP array located at the bottom of the microfluidic channel. In Figure 5.1.2(b), the microscope is focused at the illumination-FZP array located at the top of the microfluidic channel in the confocal OFM device. The misalignment at this portion of the array is estimated to be about 6–8 µm between these two FZP arrays. We notice that there is a certain portion of the array with good alignment and the bright field OFM image is acquired from that portion. At this moment, we do not have a good solution to ensure a reliable and repeatable the planar alignment between the illumination- and collection- FZP arrays. I performed the alignment and bonding under a contact aligner for standard photolithography, in which the tolerance and resolution limit is on the order of about 2 µm. However, our target optical resolution is about half of a micron. Thus, the alignment and bonding by standard photolithography is not enough to meet the precision alignment requirement of the confocal OFM system. On top of that, the control of the microfluidic height is also critical, in addition to the planar alignment between these two arrays. A microfluidic molding method by hot embossing may be a better approach compared with UV epoxy bonding, since the channel height is more controllable by this approach [1]. The alignment issue is critical for good imaging formation in confocal microscopy. Misalignment leads to loss of optical resolution and distortion of the OFM image. The alignment precision in diffractive optical elements in dark field confocal OFM imaging implementation is particularly important.
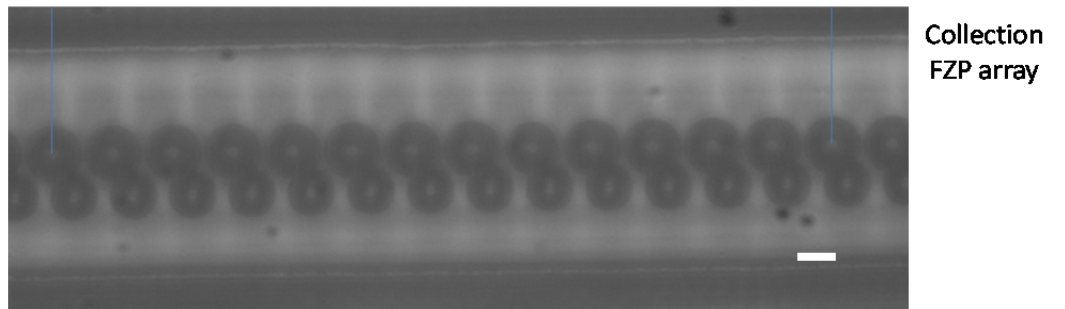
(a)
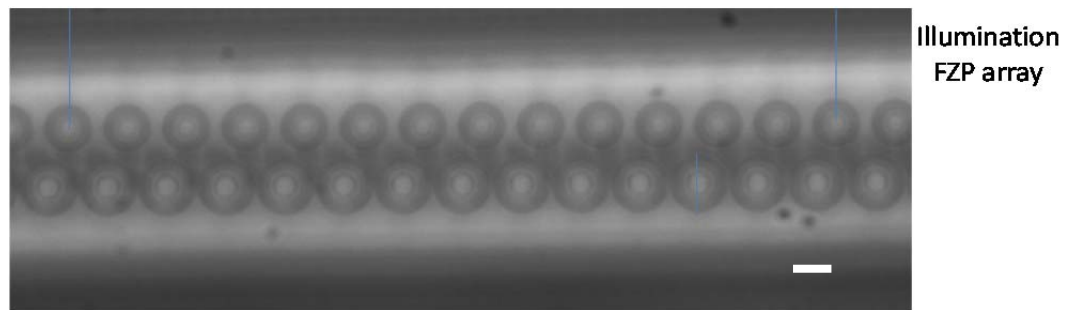
(b)

Figure 5.1.2 An experimental demonstration of misalignment problem between with the collection and illumination FZP arrays in bright field confocal OFM device with plane of observation located at (a) the collection FZP array, and (b) the illumination FZP array (scale bar: 10 μm)

5.2   Confocal Dark Field OFM Imaging

Here I would like to propose an approach to achieve confocal dark field imaging under the context of a compact OFM system. The operation principle of the confocal dark field unit is quite intuitive. It is composed of a set of bright field illumination FZP and a dark field collection FZP. As shown in Figure 5.2, when there is no scatterer, the dark field collection-FZP-aperture unit rejects all light at the focal point and gives zero intensity on the CMOS imaging sensor pixel. Thus, the background of the OFM image is dark. In contrast, when there is a scatterer, the illumination zone plate focuses light at the focal point and impinges on the scatterer. This disrupts the electric or intensity field distribution at the plane of the dark field collection zone plate. The dark field collection zone plate collects the scattered light to the aperture and rejects illumination light. This gives intensity response to the CMOS imaging sensor pixel in the presence of a scatterer. There are basically two ways to determine the zonal radius in design in the dark field collection-FZP unit. The first approach is to calculate the electric field distribution on the dark field collection-FZP plane based on Fresnel-Kirchhoff diffraction from the plane of illumination-FZP, based on the simulation scheme described in Appendix A3. The design parameter of the dark field collection-FZP can be found by a binarization process of the electric field distribution [2].
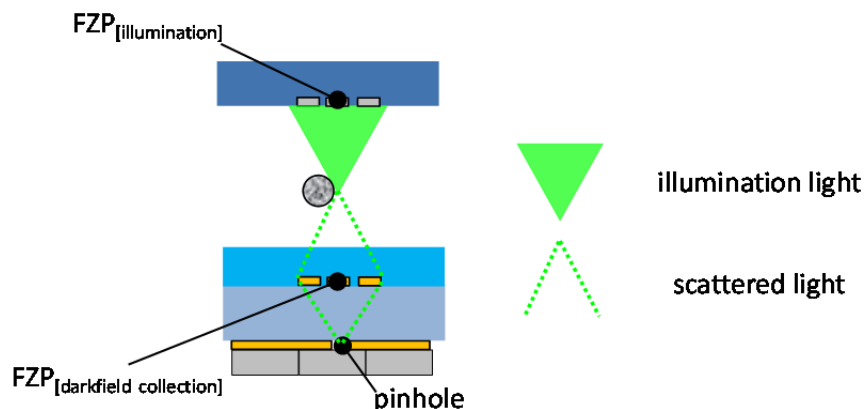
Figure 5.2 An illustration of dark field confocal OFM aperture configuration

5.3   Confocal Fluorescence OFM Imaging

The implementation of confocal fluorescence OFM imaging can simply be achieved by replacing the spacing SU-8 layer with a fluorescence filter. This SU-8 layer is 25 µm thick and this thickness is enough for most interference and absorption optical filters. The illumination-FZP array is designed based on the illumination wavelength, and the collection-FZP array is designed based on the emission wavelength of the fluorophore. As shown in Figure 5.3, when there is a fluorophore flowing along the microfluidic channel intersecting the illumination focused light spots, the fluorophore will be excited and emit light matching the wavelength of the collection-FZP array. The fluorescence filter effectively blocks the illumination wavelength and allows the emission light from the fluorophore to pass through and be collected by the confocal aperture. I believe this OFM imaging scheme has advantages over the illumination-mode fluorescence OFM systems. The incorporation of collection optics increases the collection efficiency of emission light, which is critical in fluorescence imaging. The pinhole also allows confocal or sectioning capability in fluorescence imaging of the biological samples.
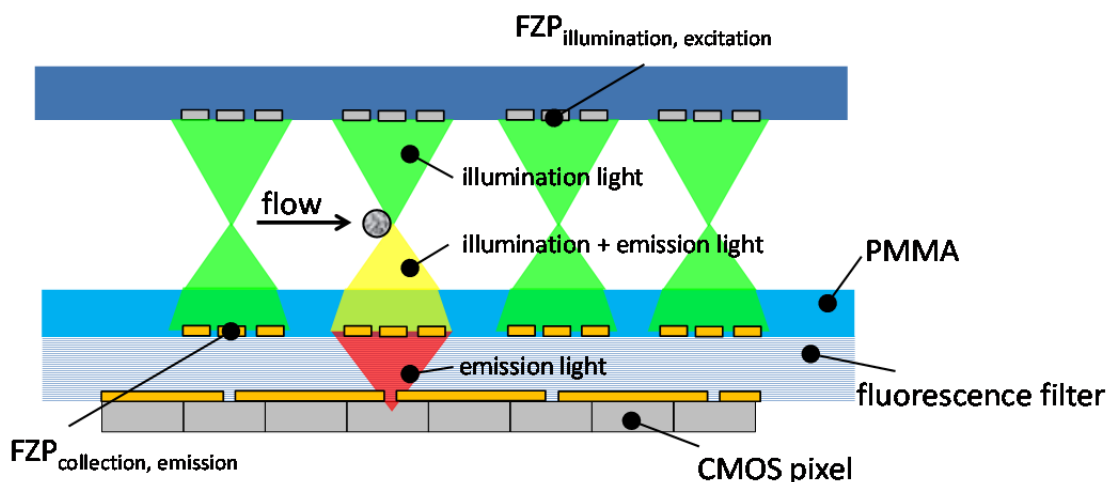
Figure 5.3 An illustration of fluorescence confocal OFM imaging device

References

[1] M. Worgull, Hot Embossing: Theory and Technology of Microreplication, William Andrew (2009)

[2] E. Schonbrun, W. N. Ye and K. B. Crozier "Scanning microscopy using a short-focal-length Fresnel zone plate," *Optics Letters* **34**, 2228–2230 (2009)

Chapter 6: Biological Applications of Optofluidic Microscopy

Microscopes and other optical microscopy devices are used extensively in all aspects of medicine and biological research. In a medical setting, clinicians typically prepare smears of fluid samples (e.g., blood samples). The slides are used to view and analyze the fluid samples under a microscope. Preparing slides takes time, potentially contaminates the samples, and adds cost to the analysis and diagnosis of illnesses. Further, conventional microscopes, upon which the slides are viewed, can be costly and relatively bulky. Optofluidic microscopy provides an attractive alternative in conventional optical imaging, due to its compactness and high throughput rate. In this chapter, I will pinpoint a few potential biological or biomedical fields that optofluidic microscopy technology is suitable for, namely quantitatively phenotype characterization in model organisms, water/environmental quality monitoring, blood-cells diagnostics, and virus detection.

6.1   Bioscience Studies – Quantitative Phenotype Characterization

A flow chart of a method of performing quantitative phenotype characterization of *C. elegans*, a widely adopted model organism in developmental biology, is shown in Figure 6.1.1. This method can be used to automatically image and analyze different phenotypes of *C. elegans*. For example, phenotypes at different stages of development or mutated strains of object phenotypes can be analyzed. This method provides an inexpensive means for conducting automated and quantitative phenotype characterization in biological studies. Although the biological sample being characterized in this illustrated example is *C. elegans*, any suitable entity can be characterized using this method. Notice that by placing multiple OFM devices, we can achieve a much higher throughput rate by taking advantage of parallel processing. The quantitative phenotype characterization process starts by immobilization or fixation of the *C. elegans*. The *C. elegans* can be immobilized by placing the worms in a heat bath or introducing an immobilizing drug into the suspension fluid medium. This immobilization process may be performed in an on-chip manner with an immobilization unit being integrated with the OFM microfluidic device, or by off-chip preparations. The fluid suspension containing *C. elegans* is introduced into the microfluidic channel of the OFM device by gravity-driven flow, as described in Section 2.3.3. After the *C. elegans* are introduced into the microfluidic channel, the OFM device will generate a series of images in microscope-level resolution, as described in Chapter 2. The OFM images generated can be used to analyze the morphology of *C. elegans* worms in order to determine value of the morphological characteristics or structures.   Suitable morphological characteristics include length, width, general shape, or internal features. Figure 6.1.2 includes images of three phenotypes of *C. elegans*, which were generated using an OFM device. The *C. elegans* in the top image is Wild-type, the middle image *Sma*-3 phenotype, and the bottom image, *Dpy*-7 phenotype. Using the values of the morphological characteristics, we can perform a quantitative phenotype characterization to determine the number of *C. elegans* in the sample suspension belonging to the different phenotypes. The characterization and sorting of different strains is through a comparison

with a library of stored morphological characteristic values for particular phenotypes or images of phenotypes. After the phenotypes are recognized, we can determine the statistical averages and the variations of each phenotype characteristic in the sample. The average values and the statistical variations for the phenotype characteristics of three strains of *C. elegans*—namely, wild-type, *Sma*-3 and *Dpy*-7, based on their length and width, are shown in Figure 6.1.2.

```
┌─────────────────────────┐
│   Immobilization of C.  │
│   elegans in heat bath  │
└─────────────────────────┘
             │
             ▼
┌─────────────────────────┐
│   Flow C. elegans into the │
│   compact OFM devices   │
└─────────────────────────┘
             │
             ▼
┌─────────────────────────┐
│   Analyze the morphology │
│   of the C. elegans OFM  │
│         images          │
└─────────────────────────┘
             │
             ▼
┌─────────────────────────┐
│  Quantitative phenotype │
│  characterization of C. │
│  elegans into different │
│         strains         │
└─────────────────────────┘
```
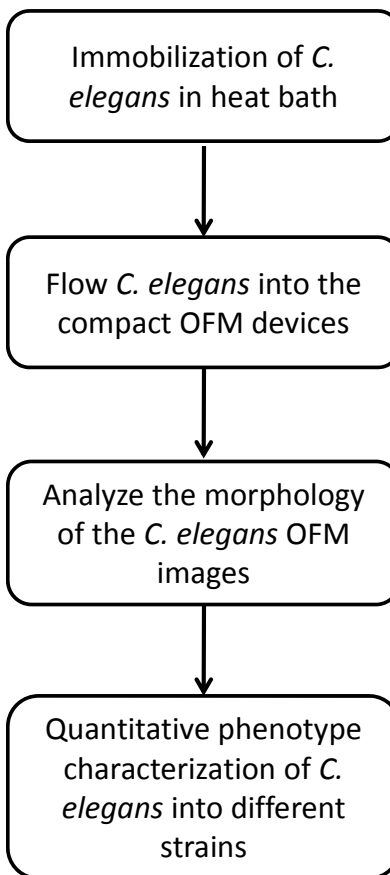
Figure 6.1.1 A flow chart of a method of performing quantitative phenotype characterization of *C. elegans* in OFM system
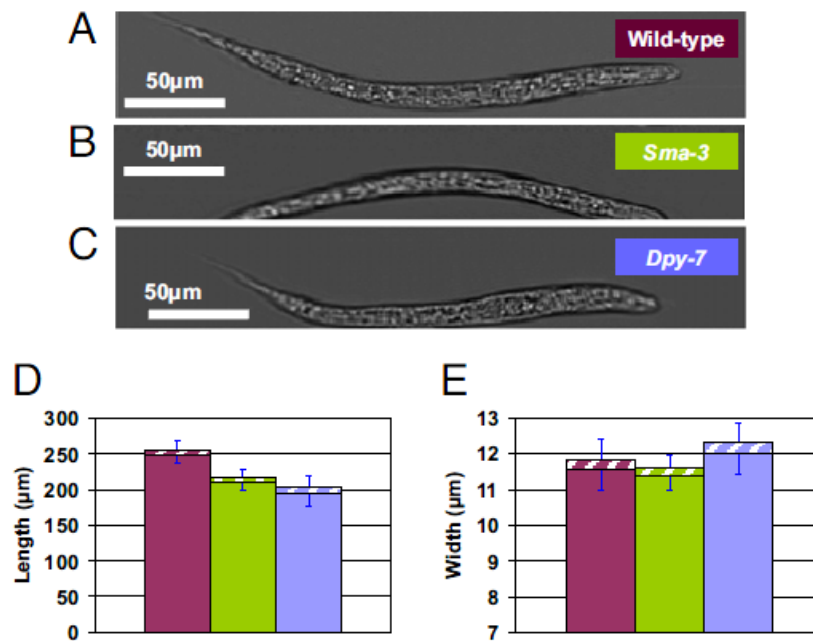
Figure 6.1.2 The quantitative phenotype characterization of three strains of *C. elegans* based on length

and width

Since OFM systems can render microscope-level resolution images, we can use the images to recognize internal features and cellular or subcellular compartments of micro-organisms or single cells (for example, the digestive tract or the pharynx of *C. elegans*, or the nucleus of single cells). We can use these traits for quantitative phenotype characterization of bio-species as well.

(This section is largely adapted from part of a published paper in reference [1].)

6.2   Water/Environmental Quality Monitoring — Towards Telemedicine

OFM systems can also be used for water or environmental monitoring. A flow chart which describes a method of detecting microbial cells in a water sample is shown in Figure 6.2.1. The method is used to detect microbial cells of a size < 10 µm (e.g., oocysts and *Giardia lamblia* cysts) in water sample and determine whether the level of these microbial cells in the water sample is safe for human consumption. Microorganisms of other suitable sizes or other objects can be detected for other purposes.

```
┌──────────┐      ┌──────────┐      ┌──────────┐
│          │      │          │      │ color or │
│ filtering│ ───► │ immuno-  │ ───► │fluorescent│
│          │      │ labeling │      │   OFM    │
└──────────┘      └──────────┘      └──────────┘
```

Figure 6.2.1 A flow chart of a method to detect microbial cells in a water sample

The method starts by filtering larger objects or contaminants from the water sample. In the illustrated example, the suspended particles being filtered from the fluid sample are objects with a predefined size greater than 20 µm such that the fluid sample is left with objects less than 20 µm in size. This can prevent clogging of the OFM device. Filtering may be performed by a microfluidic filter integrated with the OFM device. Some examples of the filtering scheme can be found in [2]. In Figure 6.2.2, a schematic drawing of a filter for a water testing sample is shown. In this example, the filter prevents the larger objects from passing and allows microbial cells Type I and II to pass through the microfluidic filter. As the fluid sample flows through the channel, the filter removes the larger objects.
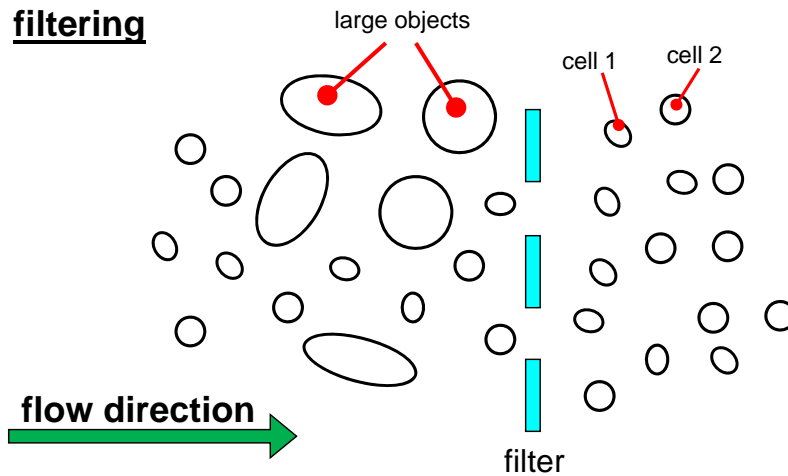
Figure 6.2.2 An illustration of a filtering scheme of a water sample

Next, the filtered microbial cells in the fluid media are labeled as shown in Figure 6.2.3, for example, by immunolabeling, which refers to the process of tagging conjugate antibodies and introducing them to the fluid sample to bind themselves to the membrane of microbial cells having the primary antigens corresponding to the tagged conjugate antibodies. Certain suitable tagging methods can be used such as fluorescent staining, gold beads, or epitope tags. By tagging the conjugate antibodies, the objects having the primary antigens corresponding to the conjugate antibodies are also tagged. For example, a fluorescent stain may be applied to conjugate antibodies and the stained conjugate antibodies added to the fluid sample. The stained conjugate antibodies bind to the membrane of the objects having the primary antigen corresponding to the conjugate antibodies. Labeling may be performed by a device entirely separate from the OFM system, or incorporated into the OFM system. After the tagged conjugate antibodies bind to the objects, the fluid sample is flushed with a buffer solution. Flushing the fluid sample removes a substantial portion of the unbound conjugate antibodies.

immuno-labeling
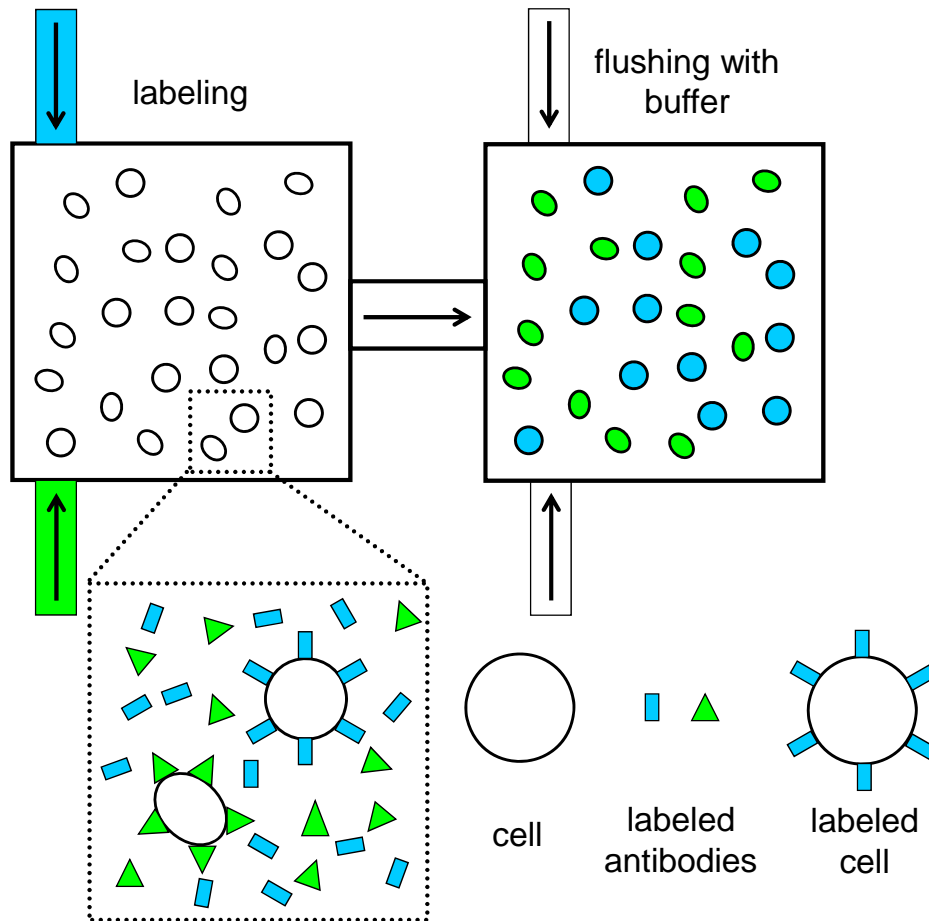
Figure 6.2.3 An illustration of an immune-labeling scheme for microbial cells in a water sample

In this example, a first-tagged conjugate antibody and a second-tagged conjugate antibody are introduced into a microfluidic chamber with the fluid sample having microbial cells Type I and II. The first-tagged conjugate antibodies are represented by triangles and the second-tagged conjugate antibodies are represented by rectangles. Once the tagged conjugate antibodies are introduced into the fluid sample, they bind specifically to the membranes of target microbial cells. The sample suspension is then flowed to a second chamber and flushed with a buffer to remove the unbound tagged conjugate antibodies. (An example of a microfluidic device used to perform immunolabeling for microbial cells from a water

sample can be found in [3].) After labeling, the cell suspension solution is introduced into the OFM device to generate images of the cells. An excitation light of a certain wavelength (e.g., blue light) illuminates the objects in the microfluidic channel. In the implementation of a fluorescence OFM system, the excitation light excites the fluorophores in tagged conjugate antibodies which re-emit light with longer wavelength. An optical filter blocks the excitation and allows emission light from the fluorescent-labeled immune microbial cells to pass through. The fluorescence OFM system is able to render fluorescence image with microscope level resolution. We can also incorporate two different optical fluorescence filters into the OFM device and use illumination of two different wavelengths. By doing this, it is possible to conduct fluorescent imaging for two different types of microbial cells with different immune expressions. Alternatively, a non-fluorescent stain can be used to tag the cells. One example is the H&E stain widely used in histology. In this case, a white light is used as the illumination, and the color or RGB filters can be used to render color images of the cells. Then, the images can be used for cell identification and counting purposes as shown in Figure 6.2.4. We can also measure the intensity of the images to quantify the immuno expression level of the cells. This information tells us the number of microbial cells appearing in the water sample and how toxic the water is. We can then compare these results with a threshold value to determine whether the water source in test is good for human consumption. Since OFM systems can be made very compact in size, the can be readily integrated onto a cell phone and information can be sent through the cell phone network for further analysis or reporting. I believe the OFM imaging method can enhance the advancement of global health [4].

(This section is partially adapted from a published paper in reference [5].)

Color or fluorescent OFM
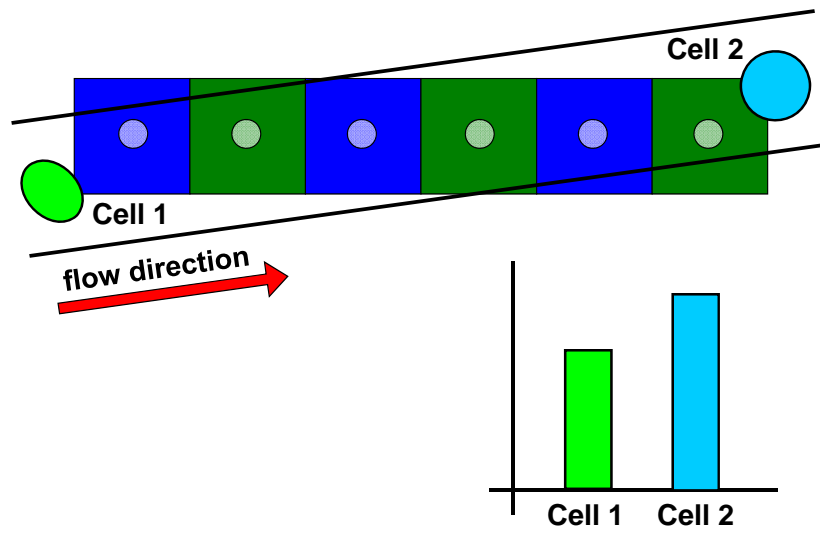
Figure 6.2.4 An illustration of the color or fluorescence OFM scheme for cell identification and counting

6.3   Blood Diagnostics — Imaging Based Blood Analysis on a Chip

A flow chart of a method of analyzing a blood sample in fluid form is shown in Figure 6.3.1. This method can be used to analyze a blood sample and diagnose an illness or to determine whether certain cells or cell structures are present in the blood sample. OFM devices provide an inexpensive means to automate blood analysis and/or illness diagnosis without the need for slide preparation or skilled technicians.

```
        ┌──────────────────────────────┐
        │   Separation of blood cells   │
        └──────────────────────────────┘
                      │
                      ▼
        ┌──────────────────────────────┐
        │   Fixation of the blood cells and │
        │   immuno-labeling if applicable   │
        └──────────────────────────────┘
                      │
                      ▼
        ┌──────────────────────────────┐
        │   Flow different fractions of  │
        │   blood cells into OFM device  │
        └──────────────────────────────┘
                      │
                      ▼
        ┌──────────────────────────────┐
        │   Blood cell analysis and disease │
        │   diagnostics based on the OFM    │
        │   images                          │
        └──────────────────────────────┘
```

| Red blood cell analysis Malaria & anaemia diagnostics | White blood cell analysis: HIV/AIDS, Leukemia monitoring & diagnostics | Early cancer detection: circulating tumor cells (CTCs) in blood | Stem cells detection and isolation |

Figure 6.3.1 A flow chart of a method for a blood sample analysis

The method begins by separating a blood sample into fractions associated with specific types of blood cells, such as red blood cells, white blood cells, plasma and platelets; one common separation method is by centrifuge. One or more fractions may be selected for further analysis. Next, the cells in the blood sample with the selected fractions are fixed through injection of formalin. Next, the blood cells are labeled (such as by immunolabeling). The staining dyes or the tagged conjugate antibodies to the cells, and then are flushed with buffer to substantially remove unbound dyes or antibodies. Labeling may not be necessary when the cells are not transparent or have color; for example, red blood cells contain hemoglobin which has a color dependent on the oxygen content of the cells and may not require immunolabeling in order to image the cells. After labeling, the blood sample is introduced into the OFM device. The OFM device then generates blood cell images for analysis or diagnosis. OFM imaging can be an essential component in blood-on-a-chip systems [6].

An OFM device can be used to analyze the red blood cell fraction in a blood sample to diagnosis certain illnesses such as anaemia and malaria. Malaria is a disease caused by protozoan parasites that infect red blood cells. The infected red blood cells have a different morphology than normal healthy red blood cells and contain parasites Plasmodium falciparum and/or gametocytes within which are opaque and can be imaged. We can use the OFM images to determine whether the red blood cells have a healthy biconcave shape and whether they are smaller than healthy red blood cells or in low quantity as with anemia.

An OFM device can also be used to analyze the white blood cell fraction in a blood sample to diagnose certain illnesses such as HIV/AIDS or Leukemia. Typically, immuno- or other labeling is used to differentiate types of white blood cells (leukocytes) such as neutrophils, lymphocytes such as T-cells (T lymphocytes), B-cells, or monocytes and certain proteins (e.g., glycoproteins) within the cells, such as

CD4 and CD8. The OFM images of the white blood cells can be used to determine the number of certain types of white blood cells. Using the OFM device, we can also analyze the morphology of the white blood cells to determine the number of immature and abnormal cells in the suspension. Thus, an OFM device can monitor or diagnose HIV/AIDS or Leukemia.

OFM devices can be used to analyze a blood sample for early cancer detection. Tumor cells generally have a larger nucleus and a higher light absorption coefficient than healthy cells. Circulating tumor cells in blood can indicate an early stage of malignant cancer. Based on detection by OFM device, physicians may determine that more aggressive therapy or treatment is needed, which may improve patient care and survivorship.

Finally, OFM devices can be used to detect and isolate stem cells in a blood sample. Stem cells can be differentiated by immuno-labeling. The OFM device detects the stem cells in the sample solution by recognizing the tagged conjugate antibodies on the stem cells. Fluorescent dyes can be used to tag different compartments or organelles in cells, such as the nucleus, cytoskeleton, and membrane proteins, and to tag certain cytoskeleton structures in cells such as actin filaments and microtubules. The OFM device generates high resolution images. We can use the OFM images of the tagged cytoskeleton structures to differentiate between different species in order to provide information for cytoskeleton-related studies and diagnose cytoskeleton-related diseases such as muscular dystrophy. Fluorescent dyes can be used to tag certain membrane proteins. Several membrane proteins are important in the regulation of physiology of the cells such as sodium/potassium ion pumps and the G-proteins. Using the generated images of the tagged membrane proteins, OFM device can detect membrane proteins and diagnosis diseases caused by certain membrane proteins such as cystic fibrosis. In addition, membrane receptors

like nicotine receptors can be tagged. OFM images of the nicotine receptors can be used to study the relationship between smoking and cancer based on these images.

6.4   Virus Detection — Subwavelength Resolution Optofluidic Microscopy

The resolution of an OFM system is fundamentally limited by the aperture size. In principle, by making smaller (subwavelength) apertures, OFM systems have been demonstrated to resolve images down to ~ 110 nm [7]. Such resolution can useful for virus detection and diagnostics. Usually, identification of viruses is conducted with PCR (polymerase chain reaction) and ELISA (enzyme-linked immunosorbent assay) test; however, this technique can be quite tedious due to frequent virus mutation rates, spurred by the hundreds of millions of new infections occurring every year. But viruses can be identified by their morphology within minutes, irrespective of the virus in question. Virologists and clinicians can use subwavelength OFM devices to detect and identify these viruses based on high-resolution OFM images, providing a low cost alternative to scanning electron microscopes (SEM) and transmission electron microscopes (TEM).

References

This chapter is largely adapted from a US patent application - Methods of Using Optofluidic Microscope Devices Lap Man Lee et al, Application number: 12/398,098, Publication number: US 2009/0225319 A1 Filing date: Mar 4, 2009

[1] X. Cui, L. M. Lee, X. Heng, W. Zhong, P. W. Sternberg, D. Psaltis and C. Yang, "Lensless high-resolution on-chip optofluidic microscopes for *Caenorhabditis elegans* and cell imaging," *Proceedings of the National Academy of Science of the United States of America* **105**, 10670–10675 (2008)

[2] C. Lay, C. Y. Teo, L. Zhu, X. L. Peh, H. M. Ji, B.-R. Chew, R. Murthy, H. F. Han and W.-T. Liu, "Enhanced microfiltration devices configured with hydrodynamic trapping and a rain drop bypass filtering architecture for microbial cells detection," *Lab on a Chip* **8**, 830–833 (2008)

[3] L. Zhu, Q. Zhang, H. Feng, S. Ang, F. S. Chau and W. T. Liu, "Filter-based microfluidic device as a platform for immunofluorescent assay of microbial cells," *Lab on a Chip* **4**, 337–341 (2004)

[4] C. D. Chin, V. Linder and S. K. Sia, "Lab-on-a-chip devices for global health," *Lab on a Chip* **7**, 41–57 (2007)

[5] L. M. Lee, X. Cui and C. Yang, "The application of on-chip optofluidic microscopy for imaging *Giardia lamblia* trophozoites and cysts," *Biomedical Microdevices* **11**, 951–958 (2009)

[6] M. Toner and D. Irimi, "Blood-on-a-Chip," *Annual Review of Biomedical Engineering* **7**, 77–103 (2005)

[7] X. Heng, E. Hsiao, D. Psaltis and C. Yang, "An optical tweezer actuated, nanoaperture-grid based optofluidic microscope implementation," *Optics Express* **15**, 16367–16375 (2007)

Chapter 7: Conclusions and Future Works

In my PhD thesis, I have presented the technology development and implementation of optofluidic microscopy on a chip level. Optofluidic microscopy can be defined as a miniaturized optical scanning imaging method using microfluidics for sample transport. Miniaturization of the conventional microscope has advantages in reduction of manufacturing cost and integration with lab-on-a-chip functionalities. Several microfluidic flow mechanisms have been studied extensively to ensure a constant-rotation and tumble-free biological sample translation. We find that simple application of a constant DC electrical field can lock spherical or ellipsoidal biological entities at constant orientation during their translation. A complete on-chip OFM device has been built by fabrication of a slanted line array of 500 nm diameter apertures on a CMOS imaging sensor. An optimal optical resolution of 800 nm is achieved when the biological samples are flowing in close proximity to the apertures in the microfluidic channel under incoherent plane wave illumination. Several single-cell entities and micro-organisms have been imaged at subcellular-level resolution using this dime-sized microscope. I further expand OFM technology development in an attempt to enable focusing capability. A line array of diffractive optical element, FZP, is fabricated with good alignment on top of the aperture line array, with a spacing layer between to relay light collection from the plane of the CMOS sensor pixel aperture to the focal plane in the microfluidic channel. An optical resolution of 650 nm is recorded at the focal point under a coherent laser source. By tilting the illumination angle, a dark field imaging scheme is implemented in experiment. In this thesis, I also outline that with the combination of illumination FZP, we are able to focus a coherent plane wave light source to a tightly focused spot of 360 nm. I believe that the combination of illumination and collection optics will lead to a complete confocal OFM system if we can overcome the alignment difficulties in the fabrication process. In this ending chapter, I am going to analyze the challenge and investigate the role of optofluidics technology in the miniaturization of optical imaging to chip-level.

7.1 Optical Imaging on a Chip

Several novel scanning-based microscopic imaging techniques have been developed and commercialized in the 20th century. Two ground-breaking advancements include scanning electron microscopy (SEM) and atomic force microscopy (AFM). SEM uses a high-energy electron beam to raster scan the sample surface for imaging. The electrons interact with the atoms of the sample, producing signals that contain information about different properties of the sample, for example, the surface topography. In SEM, the resolution is limited by the wavelength of the electron beam and the aberration associated with the focused electron beam by a set of electromagnetic lenses. SEM is able to produce very high resolution images of a sample surface less than 1 nm. AFM consists of a silicon or silicon nitride cantilever beam with a sharp tip beneath its end. The tip is brought in close proximity to the sample surface, which is the set-point position, using a piezoelectric actuating scanner. The interactions between the tip and the sample surface cause the cantilever to deflect as the scanner moves across the sample. A laser spot is emitted onto the top of the cantilever and reflected to a set of split-array photodiodes. The deflection of the cantilever beam is monitored by the change in the intensity signal received by the split photodiodes. A feedback loop controlled by an electronic system directs the piezoelectric scanner to move the tip back to the set-point position, and the relative movement of the tip is recorded in this way. AFM can reach a lateral resolution of 1 nm and a vertical resolution of 0.1 nm. These two microscopic imaging techniques can achieve a resolution at least 1000 times better than diffraction-limited conventional optical microscopy.

However, we still find that optical microscopy is a dominant approach in bioscience and biomedical imaging. There are several reasons for this: First, both SEM and AFM either require sample preparation or cause damage to the biological samples. The SEM imaging method requires that the sample be electrically conductive to prevent charge accumulation on the surface which scatters the

electron beam and makes the resulting image blurry. If the specimen is not electrically conductive, as most biological specimens are not, the sample has to be coated with a thin film of conductive layer (for example, gold or chromium) prior to the SEM examination. Recent development of environmental SEM allows for the system to operate at a higher vapor pressure and for the introduction of gas (for example, water molecules) into the chamber to lower the charging effect. Nevertheless, the high-energy electron beam can still cause damage to the biological specimen. AFM reveals the topology of a specimen by scanning the sample surface by mechanical probe, thus biological molecules, such as RNA or collagen must first be absorbed or deposited to a substrate [1, 2]. To prevent excessive damage to the biological entities, AFM application for biological imaging is usually operated in non-contact or tapping mode. AFM can also be used to study the interaction force between conjugate biological molecule pairs, for example, the specific binding by antibody and antigen in immunoassay [3]. Conventional optical microscopy, limited by the diffraction of visible light wavelength usually cannot render resolution as high as SEM or AFM. However, optical microscopy is less invasive and does not require complicated sample preparation, thus the throughput rate of optical imaging can be much higher.

OFM imaging shares some similarities with AFM and SEM as a scanning imaging technique. In theory, aperture-based OFM can potentially break the diffraction limit by using a collection aperture smaller than the wavelength of visible light, such as 100 nm, which is approaching the resolution limit of NSOM. However, in practice, the microfluidic motion of translating biological samples is subjected to Brownian fluctuation, causing image blur and distortion. OFM systems smartly combine microfluidic technology in the sample translation and a slanted-line aperture array for imaging, which highly simplifies the scanning scheme. OFM imaging can achieve a very high throughput rate when combined with advanced microfluidic control systems, enabling very large scale imaging-based analysis. It also enables integration of other lab-on-a-chip functions, for example, sorting and harvesting for stem cells or circulating tumor cells (CTCs). However, OFM imaging has a major limitation: since the biological

samples have to be suspended in a liquid medium, OFM imaging is not applicable for attached samples on a microscopic slide. In addition, the biological samples have to maintain a constant orientation and shape during the microfluidic translation for good imaging formulation. This greatly hinders the possibility for cell-dynamic studies in OFM systems. Recently, a few interesting miniaturized lensless on-chip imaging prototypes have been demonstrated in cell-division and micro-organism-movement tracking, water quality monitoring, sperm mortality study, blood cell analysis, detection of cardiotoxicity, and point-of-case diagnostics and tissue engineering [4-13]. I believe these miniaturized microscopes form a major component in BioMEMS and lab-on-a-chip systems and can promote the advancement of global health.

7.2 Optofluidic Imaging Platform on a Chip

We have studied extensively the use of microfluidics flow to control biological sample motion in order to ensure good OFM image quality. Can we incorporate the usage of microfluidics to advance on-chip optical imaging? Liquid is incompressible but deformable, this property is very favorable for building a reconfigurable microsystem, since liquid can change its shape but maintain a constant volume upon the application of external force. In the last section of my thesis, I would like to revisit an article we first published in 2006 [14] to search for some inspirations for the development of a reconfigurable optofluidic imaging platform as shown in Figure 7.2.
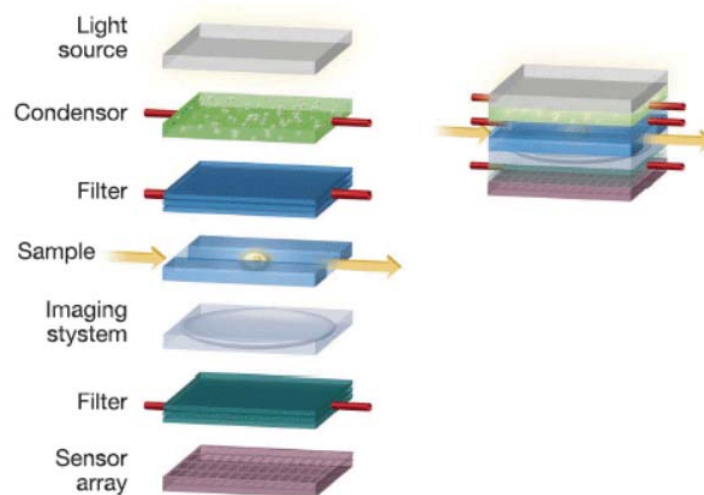
Figure 7.2 A schematic of an adjustable-focal-depth optofluidic transmission microscope, the light source, the condenser, the spectral filters, and the imaging system

There are two components in the reconfigurable optofluidic transmission microscope platform to which I think it is appropriate to apply microfluidics technology. The first one is the integration of a microfluidic switching light source. In the recent development of a multi-color fast-switching microfluidic droplet dye laser, a train of alternating droplets containing solutions of different fluorescent dyes is generated in a microfluidic channel. These fluorescent droplets act as the lasing medium and are stimulated by a pulsed laser operating in whispering gallery mode. This dye laser is able to switch the wavelength of its emission between 580 nm and 680 nm at frequencies of up to 3.6 kHz [15]. This approach is particularly attractive for fluorescence applications in on-chip imaging if we need to switch the excitation wavelength to excite different fluorophores on the same chip. The second component is the imaging system. In on-chip optical imaging microscopy, we have to make sure the biological samples are in close proximity to the imaging sensor pixel to ensure good optical resolution. We can potentially overcome this problem by incorporation of a liquid lens, in which we can move the focal plane by changing the radius of curvature of the liquid interface. Optofluidic lenses have been developed quite extensively in the past ten years, relying on different operation mechanisms [16, 17]. I find that an electrical-based optofluidic lens is particularly suitable for on-chip imaging applications due to its fast response time [18-20].

References

[1] R. Lal and S. A. John, "Biological applications of atomic force microscopy," *American Journal of Physiology: Cell Physiology* **266**, C1–C21 (1994)

[2] S. Kasas, N. H. Thomson, B. L. Smith, P. K. Hansma, J. Miklossy and H. G. Hansma, "Biological applications of the AFM: from single molecules to organs," *International Journal of Imaging Systems and Technology* **8**, 151–161 (1997)

[3] Caltech APh 109 course materials, AFM module

[4] T. Su, A. Erlinger, D. Tseng and A. Ozcan, "Compact and light-weight automated semen analysis platform using lensfree on-chip microscopy," *Analytical Chemistry* **82**, 8307–8312 (2010)

[5] O. Mudanyali, C. Oztoprak, D. Tseng, A. Erlinger and A. Ozcan, "Detection of waterborne parasites using field-portable and cost-effective lensfree microscopy," *Lab on a Chip* **10**, 2419–2423 (2010)

[6] S. Seo, S. O. Isikman, I. Sencan, O. Mudanyali, T. Su, W. Bishara, A. Erlinger and A. Ozcan, "High-throughput lensfree blood analysis on a chip," *Analytical Chemistry* **82**, 4621–4627 (2010)

[7] G. Stybayeva, O. Mudanyali, S. Seo, J. Silangcruz, M. Macal, E. Ramanculov, S. Dandekar, A. Erlinger, A. Ozcan and A. Revzin, "Lensfree holographic imaging of antibody microarrays for high-throughput detection of leukocyte numbers and function," *Analytical Chemistry* **82**, 3736–3744 (2010)

[8] S. B. Kim, H. Bae, J. M. Cha, S. J. Moon, M. R. Dokmeci, D. M. Cropek and A. Khademhosseini, "A cell-based biosensor for real-time detection of cardiotoxicity using lensfree imaging," *Lab on a Chip* **11**, 1801–1807 (2011)

[9] S. Moon, H. O. Keles, A. Ozcan, A. Khademhosseini, E. Hæggstrom, D. Kuritzkes and U. Demirci, "Integrating microfluidics and lensless imaging for point-of-care testing," *Biosensors and Bioelectronics* **24**, 3208–3214 (2009)

[10] C. D. Chin, V. Linder, S. K. Sia, "Lab-on-a-chip devices for global health: past studies and future opportunities," *Lab on a Chip* **7**, 41–57 (2007)

[11] H. Varmus, R. Klausner, E. Zerhouni, T. Acharya, A. S. Daar and P. A. Singer, "Grand challenges in global health," *Science* **302**, 398–399 (2003)

[12] P. Yager, G. J. Doming and John Gerdes, "Point-of-care diagnostics for global health," *Annual Review of Biomedical Engineering* **10**, 107–144 (2008)

[13] U. A. Gurkan, S. Moon, H. Geckil, F. Xu, S. Wang, T. J. Lu and U. Demirci, "Miniaturized lensless imaging systems for cell and microorganism visualization in point-of-care testing," *Biotechnology Journal* **6**, 138–149 (2011)

[14] C. Yang and D. Psaltis, "Optofluidics can create small, cheap biophotonic devices," *Laser Focus World* **42**, 85–88 (2006)

[15] S. K. Y. Tang, Z. Li, A. R. Abate, J. J. Agresti, D. A. Weitz, D. Psaltis and George M. Whitesides, "A multi-color fast-switching microfluidic droplet dye laser," *Lab on a Chip* **9**, 2767–2771 (2009)

[16] N.-T. Nguyen, "Micro-optofluidic lenses: a review," *Biomicrofluidics* **4**, 031501 (2010)

[17] L. Dong, A. K. Agarwal, D. J. Beebe and H. Jiang, "Adaptive liquid microlenses activated by stimuli-responsive hydrogels," *Nature* **442**, 551–554 (2006)

[18] S. Kuiper and B. H. W. Hendriks, "Variable-focus liquid lens for miniature cameras," *Applied Physics Letters* **85**, 1128–1130 (2004)

[19] C. B. Gorman, H. A. Biebuyck and G. M. Whitesides, "Control of the shape of liquid lenses on a modified gold surface using an applied electrical potential across a self-assembled monolayer," *Langmuir* **11**, 2242–2246 (1995)

[20] H. J. J. Verheijen and M. W. J. Prins, "Reversible electrowetting and trapping of charge: model and experiments," *Langmuir* **15**, 6616–6620 (1999)

Appendix A.1: Microfluidic Channel Surface Modification and Biological Sample Preparations

PEG Grafting Process to Promote the Flow of Samples in OFM Microfluidic Channels

To facilitate smooth flow of our biological samples in the device and to prevent debris adhesion to the microfluidic channel walls, we conditioned the channel walls through the following process. First, the microfluidic channel is filled up and flushed with a 10% poly(ethylene glycol) (PEG) solution, 0.5 mM NaIO4, and 0.5% (by weight) benzyl alcohol. The OFM device is then placed under a UV light source for 1 hour to promote PEG deposition onto the channel walls. This process is similar to the one developed in [1]. The PEG-grafted surface prevents nonspecific adsorption with biological entities and lubricates the object flow. The device is then rinsed with deionized water, dried, and stored under ambient condition (the PEG-grafted surface has long-term stability).

Biological Sample Preparations for OFM Experiments

Chlamydomonas cells (8–16 µm) were purchased from Carolina Scientific. Before use, the cells are immobilized by heat bath at 50ºC for 10 minutes. The cell is suspended in the culture buffer provided by the company and then used directly without dilution. Mulberry pollen spores (11 µm to 16 µm) were purchased from Duke Scientific, and polystyrene microspheres (10 µm) from PolyScience respectively. These are suspended in 1.0 mM phosphate buffer saline (PBS). The cell suspensions are sonicated before use. The suspensions of *G. lamblia* cysts and trophozoites (H3 isolate) were purchased from WaterBorne, Inc., USA. They are fixed and preserved in 5% Formalin/PBS at pH 7.4/0.01% Tween 20. The *G. lamblia* cyst has an oval shape, about 7–10 µm in width and 8–13 µm in length, while its trophozoite form has a particular pear shape and is approximately 10–20 µm in dimension. Before use, the suspensions were sonicated and filtered with a 40 µm cell strainer (BD Falcon, USA). The number concentration of targets in the suspensions is approximately 10^6 per ml.

Appendix A.2: Advanced Microfluidic Control for High Throughput Applications

The incorporation of a hydrodynamic focusing system to OFM can not only control the motion of the biological samples in the OFM image-acquisition region, but also increase the throughput of the OFM systems dramatically. The hydrodynamic focusing unit is composed of an injection unit where the sample cell suspension is introduced to the system, and two focusing units which create sheath streams to focus the cells to the core (the mid axis of the microfluidic channel). In Chapter 2, we discussed that when the biological samples are translating in the channel mid-axis, their vorticity is exactly zero. In theory, the flowing sample will not experience any rotational motion regardless of its shape or orientation. After passing the focusing region, the cells will reach a steady state in the OFM region for good image acquisition, as shown in Figure A.2. Notice that this illustration is for 2-D hydrodynamic focusing. We have already demonstrated in experiment that with a simple 3-D hydrodynamic focusing unit, the microfluidic flow of 10 µm microspheres focused to the channel mid-axis less than 1 mm under optimized conditions. The building of 3-D hydrodynamic focusing is similar to [2] in including additional sheath flow channels from the top and bottom of the sample flow channel. The rate of the cell flow is determined by the flow rate of the focusing units, the differential pressure before the focusing units and the injection units and the concentration of the sample cell suspension. Although we do not expect the throughput rate of our OFM system, assisted with the hydrodynamic focusing unit, to be as high as most commercially available flow cytometers (which can have a throughput rate up to a few thousands cells per second), we think it is very possible to have a throughput rate of about one thousand cells per minute. It is worth mentioning that there are recent developments of an exciting microfluidic self-focusing technique using inertia microfluidics [3]. Biological samples with different shapes can be aligned hydrodynamically in a certain orientation by inertial effect. It has been demonstrated that inertial microfluidics requires a

simple planar configuration in the design of the microfluidic channel, which can be readily adapted to OFM applications [4, 5]. We also notice that there exist other approaches for focusing biological samples in a microfluidic channel, for example, by electrokinetics or acoustics [6, 7]. Although these implementations require a more complicated design, they deserve a close look to evaluate the suitability of adapting these techniques to OFM applications.
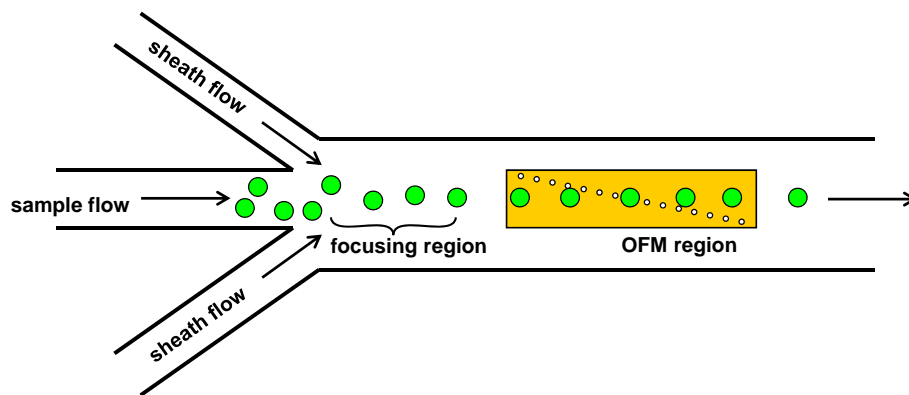
Figure A.2 A hydrodynamic focusing unit for high throughput OFM applications

Appendix A.3: Numerical Simulation Scheme

A numerical simulation scheme has been implemented to determine the PSF of the collection-FZP-aperture unit as shown in Figure A.3.1. The purpose of this numerical simulation study is to validate with the experimental result in Section 3.2.3.1. The electric field distribution from a point source at the object plane is calculated in the zone plate plane. A Fresnel zone plate with zonal radii based on the formulation in Section 3.2.2 is imposed in the zone plate plane. The transparent zone transmits the electric field while the opaque zone blocks the electric field from the point source. This electric field distribution truncated by the zone plate is propagated in free space. With the paraxial approximation, the diffraction pattern in the detection plane can be calculated using the Fresnel-Kirchhoff diffraction integral formulation [8]. The intensity distribution in the detection plane of the diffraction pattern is calculated by simply taking the square of the absolute value of the electric field. The light intensity collected by the aperture is determined by integration of the intensity distribution enclosed by the collection area in the detection plane. The detailed formulation of this numerical simulation scheme is illustrated in Figure A.3.2. Note that the simulation scheme is based on scalar diffraction theory, which neglects the fundamental vectorial nature of light as an electromagnetic wave described by Maxwell's equation. The scalar theory is able to yield highly accurate results under the following conditions: (1) the size of the diffraction aperture or grating must be large compared with the wavelength and (2) the detection plane of the diffraction pattern has to be placed sufficiently far enough from the plane of the aperture or the zone plate [9]. It is possible to use commercial numerical simulation tools such as, COMSOL or CST Studio, which is based on FEM or FDTD numerical methods to solve the complete Maxwell's equation. However, given the large size of propagative free space in our problem, the numerical computation is expected to be very demanding.
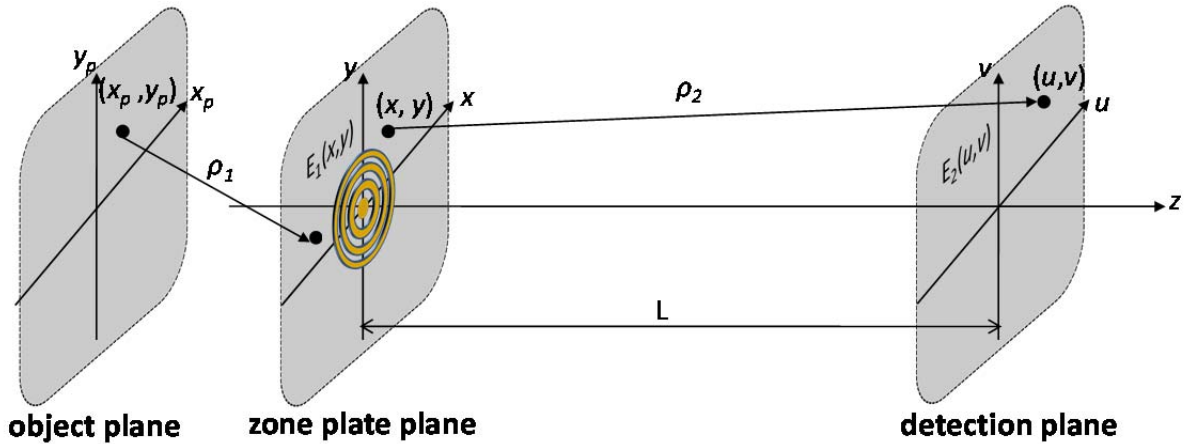
Figure A.3.1 A numerical simulation scheme based on Fresnel-Kirchhoff diffraction integral

formulation to determine the focusing property of the FZP-aperture unit

- **Determine the E-field of the zone plate plane $E_1(x,y)$**
  - Plane wave: $E_1(x,y) = Ae^{jky\sin\theta}$
  - Point source: $E_1(x,y) = Ae^{jk\rho_1}/\rho_1$ $\rho_1 = \sqrt{z^2 + (x_p - x)^2 + (y_p - y)^2}$
  - Assumption made: lumped refractive index

    $$\mu_1 = \frac{\mu_{water}\, z_{water} + \mu_{PMMA}\, z_{PMMA}}{z_{water} + z_{PMMA}}$$

- **Determine the E-field of the image plane $E_2(x,y)$**
  - Huygens principle

    $$E_2(x,y) = A\iint \frac{E_1(x,y)e^{ik\rho_2(x,y,u,v)}}{\rho_2} dxdy$$

  - *Fresnel-Kirchhoff diffraction integral formula* $x, y, u, v < L$
    - Paraxial approximation

      $$E_2(x,y) = \frac{-jA}{kL} e^{jkL} \cdot e^{jk\frac{u^2+v^2}{2L}} \iint E_1(x,y) \cdot e^{jk\frac{x^2+y^2}{2L}} \cdot e^{-jk\frac{xu+yu}{L}} dxdy$$

- **Determine the intensity of the image plane $I_2(x,y) \propto E_2(x,y) \cdot E_2^*(x,y)$**
  - Integrate the intensity flowed into the collection aperture or pixel area to calculate the collection power

Figure A.3.2 The formulation process based on Fresnel-Kirchhoff diffraction integral to determine

the focusing property of the FZP-aperture unit

Appendix A.4: Characterization of Different Factors affecting the Optical Performance of Collection FZP-aperture Unit

<u>Characterization of individual Collection FZP-aperture unit - experiment</u>

A set of experiments has been conducted to characterize the focusing property of individual zone plates in the collection-mode FZP-aperture OFM device. Note that the characterization is conducted using a 40 × water immersion with NA=0.8 and focal point resolution of 330nm. The mean FWHM values of 12 FZP-aperture units is 1.1μm and the standard derivation/mean = 7%. We find that there is a noticeable disagreement between these values and those in Section 3.2.3.1. The reasons can be attributed to the following. The FZP-aperture units tested in this study are actually come from a dissembled collection-mode FZP-aperture OFM device. This set FZP-aperture array coated with a PMMA layer of 5μm and the PSF characterization was conducted in a water immersion objective. In addition, I also experienced some difficulties to search the focal plane for every FZP-aperture units in a single scan using the motion controller with a scanning distance about 200 μm. We may be able to achieve a higher optical resolution with a better optical setup. Nonetheless, this set of study illustrates that the variation of the focusing property of individual FZP-aperture unit is not significant successive 12 FZP-aperture units in the OFM device.
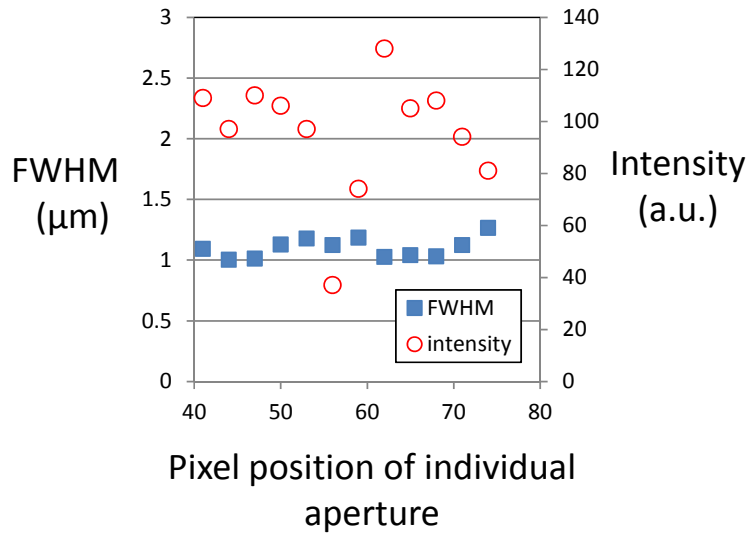
Figure A.4.1 A plotting showing the FWHM and intensity variation for individual FZP-aperture

in the collection-mode OFM device

Variation in the refractive index of photoresist – numerical simulations
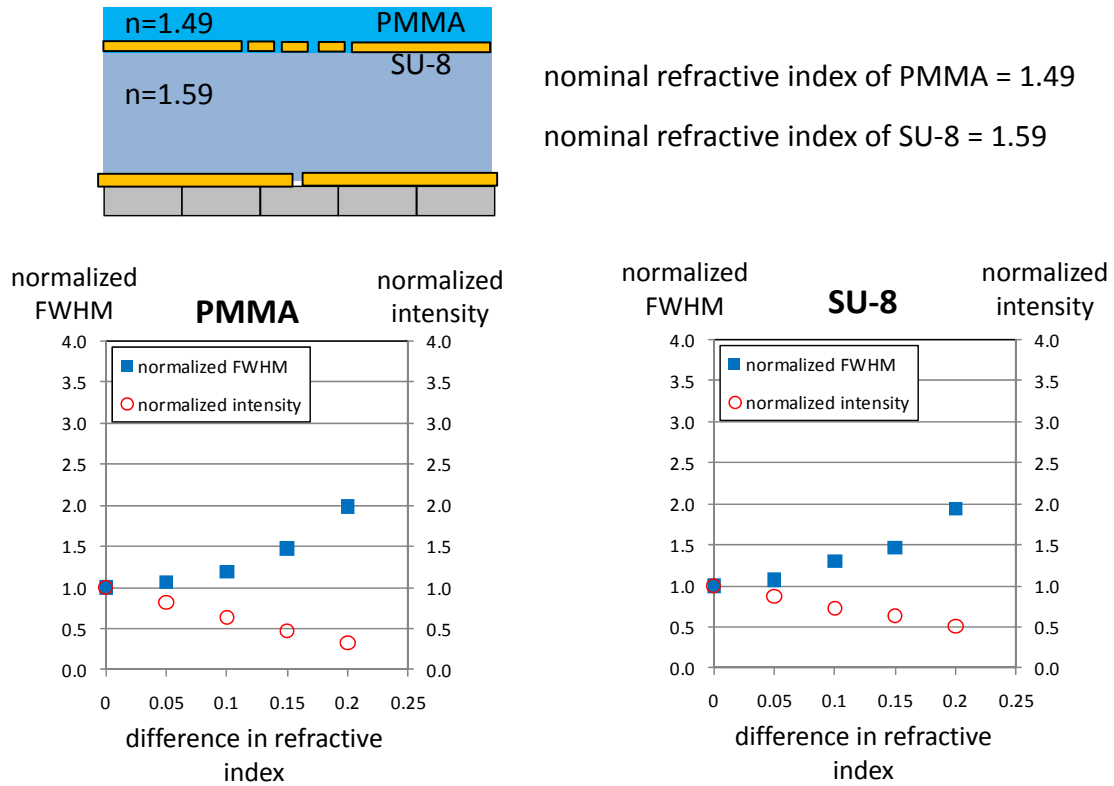
Figure A.4.2 A plotting showing the effect on the normalized FWHM and intensity of the collection FZP-aperture when there is a deviation in the refractive index of the photoresists

Variation in the thickness of photoresist – numerical simulations
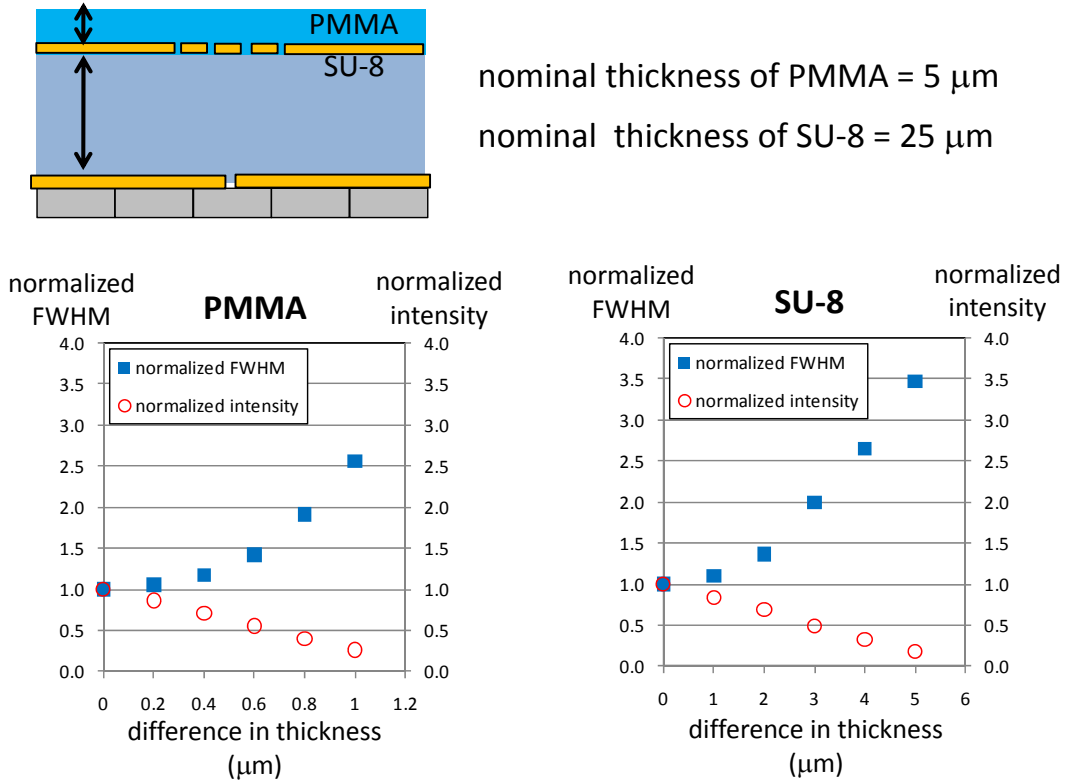
Figure A.4.3 A plotting showing the effect on the normalized FWHM and intensity of the

collection FZP-aperture when there is a deviation in the thickness of the photoresists

Variation in refractive index of photoresist – numerical simulations
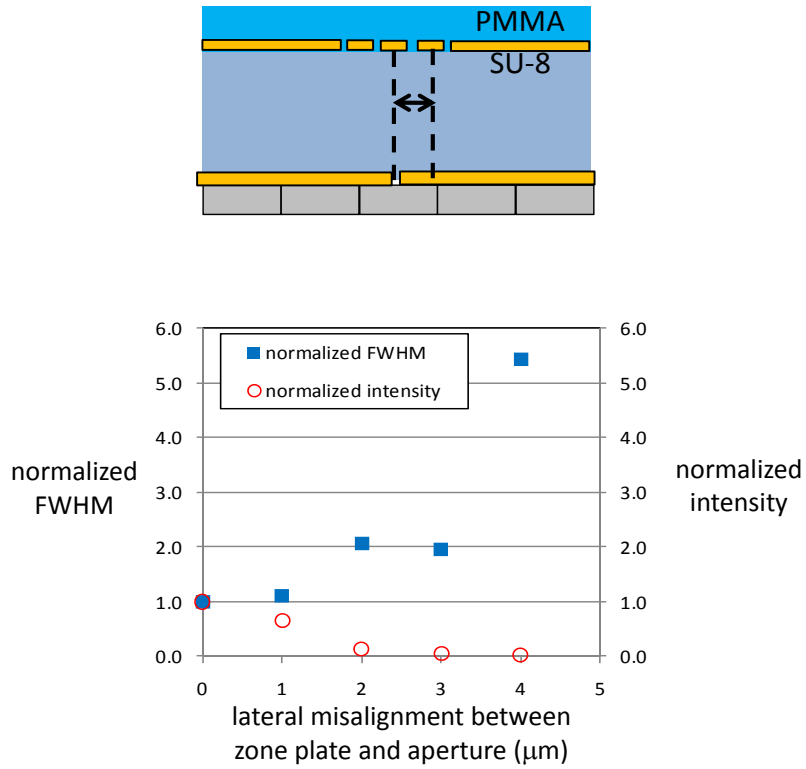
Figure A.4.4 A plotting showing the effect on the normalized FWHM and intensity of the

collection FZP-aperture when there is lateral misalignment between the FZP and aperture

References

[1] S. Hu, X. Ren, M. Bachman, C. E. Sims, C. P. Li, and N. Allbritton, "Cross-linked coatings for electrophoretic separations in poly(dimetylsiloxane) microchannels," *Electrophoresis* **24**, 3679–3688 (2003)

[2] N. Sundararajan, M. S. Pio, L. P. Lee, and A. A. Berlin, "Three-dimensional hydrodynamic focusing in polydimethylsiloxane micro-channels for molecular detection," *Journal of Microelectromechanical Systems* **13** 559–567 (2004)

[3] D. Di Carlo, "Inertial microfluidics," *Lab on a Chip* **9**, 3038–3046 (2009)

[4] D. Di Carlo, D. Irimia, R. G. Tompkins and M. Toner, "Continuous inertial focusing, ordering, and separation of particles in microchannels," *Proceedings of the National Academy of Sciences of the United States of America* **104**, 18892–18897 (2007)

[5] D. Di Carlo, J. F. Edd, K. J. Humphry, H. A. Stone, and M. Toner, "Particle segregation and dynamics in confined flows," *Physical. Review Letters* **102**, 094503–4 (2009)

[6] S. C. Jacobson, and J. M. Ramsey, "Electrokinetic focusing in microfabricated channel structures," *Analytical Chemistry* **69**, 3212–3217 (1997)

[7] J. Shi, S. Yazdi, S. Lin, X. Ding, I-K, Chiang, K. Sharp, and T. J. Huang, "Three-dimensional continuous particle focusing in a microfluidic channel via standing surface acoustic waves (SSAW)," *Lab on a Chip* **11**, 2319-2324 (2011)

[8] U. Schnars, and W. Jüptner, "Direct recording of holograms by a CCD target and numerical reconstruction," *Applied Optics* **33**, 179-181 (1994)

[9] J. W. Goodman, Introduction to Fourier Optics, Roberts & Co, 3rd edition (2004)